공학박사 학위논문

Molecular-level Understanding of the Synthesis of Iron-oxo and Cadmium-doped Silver Nanoclusters

철-산소 나노클러스터와 카드뮴-도핑된 은 나노클러스터의 합성에 대한 분자 수준의 이해

2020 년 2 월

서울대학교 대학원

화학생물공학부

장호근

Molecular-level Understanding of the Synthesis of Iron-oxo and Cadmium-doped Silver Nanoclusters

지도 교수 현 택 환

이 논문을 공학박사 학위논문으로 제출함
2020년 1월

서울대학교 대학원
화학생물공학부
장 호 근

장호근의 공학박사 학위논문을 인준함
2020년 1월

위 원 장 성 영 은 (인)
부위원장 현 택환 (인)
위 원 박 정 원 (인)
위 원 박 원 철 (인)
위 원 문 정 희 (인)

Abstract

Molecular-level Understanding of the Synthesis of Iron-oxo and Cadmium-doped Silver Nanoclusters

Hogeun Chang

School of Chemical & Biological Engineering

Seoul National University

The synthesis of nanoparticles with unique atomic composition and structure can guide their promising physicochemical properties, which foster their use in various applications. As the targeted products of the nanomaterial synthesis are becoming more complicated, a clear understanding of the overall synthetic process is prerequisite for boosting the efficient synthesis and thereby performance of the products. The mechanistic approaches on the nanoparticle synthesis elucidate that distinct nonclassical nucleation and growth models are required to explain the formation of nanoparticles. In addition, nanoclusters observed while studying in detail the nanoparticles' synthesis can connect the missing-link between metal ligand complexes and nanoparticles. The current thesis focuses on the characterization and molecular-level understandings of the synthesis of nanoparticles and nanoclusters.

First, the synthesis of iron oxide nanoparticles is delicately controlled by limiting thermal decomposition and studied in detail by introducing a combinatorial analysis technique. Molecular-level understandings on the synthesis are successfully achieved from the starting materials to nanoparticles. The widely used precursor, iron-oleate complex, is shown to have a trinuclear-oxo cluster structure, and it can be continuously grown into sub-nanometer iron-oxo clusters followed by iron oxide nanoparticles without having a distinct nucleation stage. Such an atom-level growth is observed because of the following two effects. First, the ligand stabilization on the metal-oxo core is amplified under the limited thermal decomposition condition. Second, nonhydrolytic sol-gel like condensation is controlled at low temperature. Considering the analogy of various metal oxide nanoparticles synthesis, the continuous growth process shown in this work can provide new insights into the formation mechanism of other metal oxide nanoparticles.

Second, non-noble metal doped metal nanoclusters, which has been challenging to obtain non-gold noble metal nanoclusters, are successfully synthesized by introducing assisting ligands. Particularly, cadmium-doped silver nanoclusters ($Cd_{12}Ag_{32}(SePh)_{36}$) are synthesized with the aid of phosphines in the reaction. This cluster is characterized to have unique absorption and near-infrared photoluminescence features. Its X-ray single crystal structure reveals an asymmetric $Ag_4@Ag_{24}$ metal core structure covered by four $Cd_3Ag(SePh)_9$ surface motifs. The electronic structure of nanoclusters is also studied by "super-atom" theory and time-dependent density functional theory calculations. The $Cd_{12}Ag_{32}(SePh)_{36}$ is a 20-electron superatom and its theoretical chiral optical response is comparable to that of the well-known $Au_{38}(SR)_{24}$ cluster. Ligand-assisted synthesis of nanoclusters may pave the way for introducing other active metals into noble metal clusters.

Keywords: nanoparticles, nanoclusters, formation mechanism, molecular-level understanding, mass spectrometry.

Student Number 2015-30218

Contents

List of Figures

List of Tables

Chapter 1. Introduction to Inorganic Nanoclusters: Between Molecule and Nanoparticle

1.1 Introduction

Nanoscience has gained a wide range of interests in the past several decades as nano-sized materials show distinct physical and chemical properties compare to bulk counterparts. The importance of size dependent properties has promoted the advance of the synthetic methods to control size and monodispersity. However, until now, nanomaterial synthesis is frequently achieved by empirical trial-and-error approaches without sufficient fundamental understandings. As the targeted products of the nanomaterial synthesis are becoming more complicated, the clear understanding on the overall synthesis process is a prerequisite for boosting the efficiency to optimize the synthesis and improve the performance of the products.

In the controlled nanoparticle synthesis, intermediate species which have tens to hundreds of atoms, so called nanoclusters, are successfully observed between the transition from molecular precursors to nanoparticles. Nanoclusters whose size are in between molecules and nanoparticles have succeeded subsequent interests of nanomaterial scientists, as nanoparticles whose size are in between molecules and bulk solids drew attentions according to their novel properties.

This chapter will introduce the research background on the inorganic nanoclusters. Firstly, fundamentals regarding the nanoparticle formation and growth control are presented. This is classical nucleation and growth model succeeded from 1940's colloidal chemistry. Mechanism studies on various nanoparticle synthesis are subsequently summarized with introduction of nanoclusters observed in the nonclassical nucleation and growth pathway. Nanoclusters, which can be observed during the mechanism studies on several nanoparticle syntheses or achieved in precise chemical formula by particular synthetic approaches, are briefly introduced including noble-metal, metal chalcogenide, and metal oxide. Overviews on this dissertation is summarized at the last section.

1.2 Fundamentals on the synthesis of inorganic nanoparticles

1.2.1 Classical nucleation and growth model

The formation mechanism of monodisperse nanoparticles has been explained by the classical theory based on burst nucleation and separated growth mechanism, in which nucleation occurs rapidly after the injection of precursors, and then growth occurs separately.[1]

Synthesis of monodisperse nanoparticles is achieved by various synthetic protocols, such as reduction, thermal decomposition, and nonhydrolytic sol-gel process. Although a chemical nature of synthesis is diversified, scientists endeavor to understand a variety of synthesis process by their analogous characteristics. The colloidal synthesis of nanoparticles can be generally described by three steps: monomer formation, nucleation, and growth. Notably, three-step mechanism is analogous to LaMer model explained the formation of monodisperse hydrosol with micrometer size (Fig. 1.1).

For the growth of nanoparticles in solution, seed substance is necessary so that the crystallization can be followed at the surface between the seeds and the solution. These seeds initializing particle formation are called nuclei and the formation of them is nucleation. Nuclei can be either generated in the reaction media or introduced externally. The former one, a homogeneous nucleation process, is widely accepted concept to understand colloidal synthesis of nanoparticles by two representative methods: hot-injection and heat-up process. The latter one is a heterogeneous nucleation process and occurs in the synthesis of nanomaterials which grow based on nano-sized seeds or surfaces.

Ideally, homogeneous nucleation can occur at once and nuclei can be grown into uniform-sized particles (Fig. 1.2b). However, in practical reaction condition, nuclei are generated within a distinct period, rather than at once. As a result, the size and number increase of produced nanoparticles unavoidably coincide with the broadened size distribution in that the size distribution shows maximum at the end of the nucleation period (Fig. 1.2a). Accordingly, to produce monodisperse nanoparticles, the nucleation step must be quickly terminated and separated from the growth step. High supersaturation, which can be achieved by the accumulation of monomers before nucleation, is required to advance a homogeneous and immediate nucleation process. The nucleation begins when supersaturation level overtakes a critical concentration (minimum concentration for homogeneous nucleation, C_{crit} in Fig. 1.1). The dramatic consumption of monomers, induced by the nucleation and following growth, abruptly decreases the concentration level and limits the additional nucleation events. Such a quick nucleation, so called “burst nucleation”, is no better than the ideal single-step nucleation.[2]

During the growth process after nucleation period, precipitation and dissolution of solute (precursor or monomer) occurs competitively on the particle surface and they determine the growth rate of each particle. If the increase rate of the particle volume is equal to the diffusion rate of the solute from the solution to the particle (diffusion-controlled growth model), the growth rate of the particles decreases when the size of particles increases.[3] As a result, the distribution of particles is decreased as the faster growth rate of smaller particles induce the them to be reached to the size of larger ones. This effect is called “size focusing” (Fig. 1.2c).[4]

As time advances, the solute concentration is diminished in the solution that the concentration is much lower that the solubility. In this condition, the particles can be redissolved into the solution. Based on Gibbs-Thompson relation, the chemical potential of particles decreases with the increase of size. In other words, larger particles are more stable than smaller particles. Whereas smaller particles with higher chemical potential are dissolved into the solution, larger particles with lower chemical potential grows with slow rate. This is called “Ostwald ripening”. As a result of Ostwald ripening, the particle concentration and solute concentration in the solution decreases, but the average and the standard deviation of the size of particles slowly increases (Fig. 1.3).[3, 5-9]

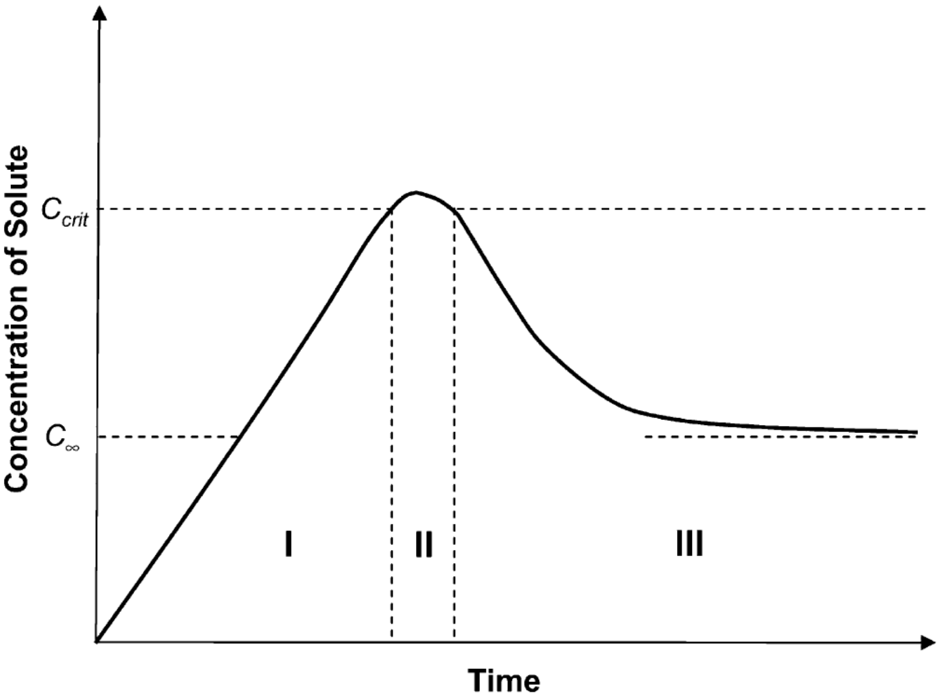

Figure 1.1 The LaMer diagram explaining the formation process of monodisperse particles. Here, C_∞ and C_{crit} denote the equilibrium concentration and critical concentration. The regions I, II, and III refers to the prenucleation, nucleation, and growth stage. (from Ref. [10], *J. Colloid Interface Sci.* **2007,** *309*, 106-118.)

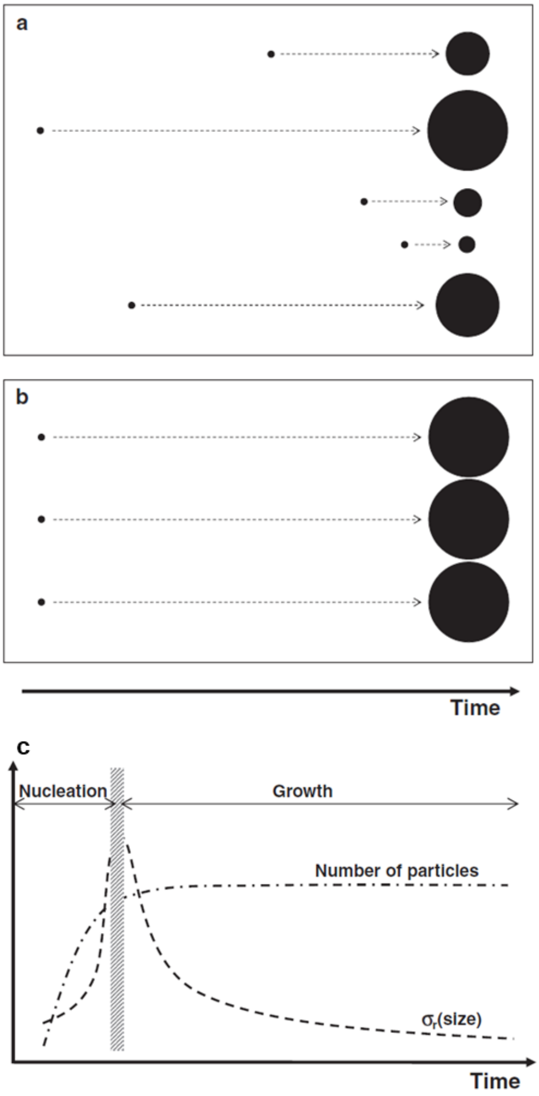

Figure 1.2 (a,b) Schematics of the crystallization reaction for two distinct cases in which homogeneous nucleation occurs (a) randomly or (b) simultaneously. (c) The change of the number of particles and size distribution during homogeneous nucleation and growth process. (from Ref. [2], *Small* **2011,** *7*, 2685-2702.)

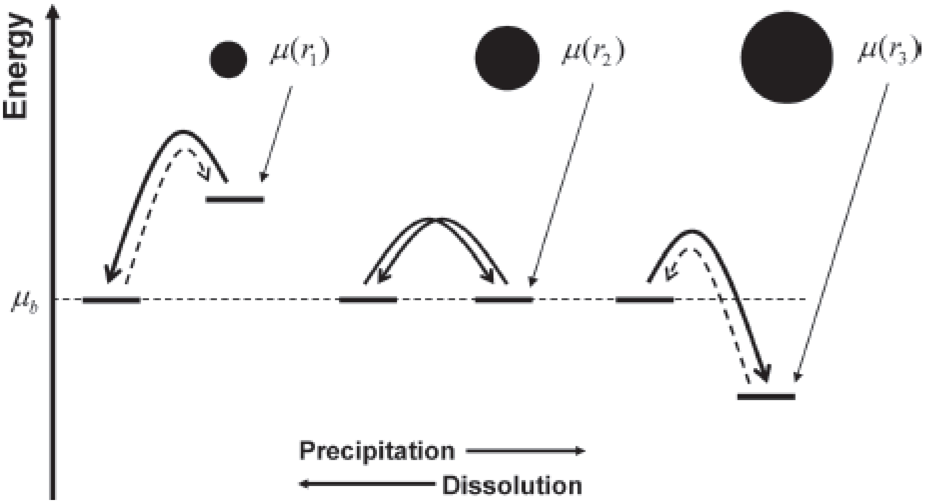

Figure 1.3 Schematics of chemical potential related to the size of particles. Three different sized particles are presented for examples as shown in black circles. Here, μ_b and $\mu(r)$ refer the chemical potentials of the monomers in the solution and the particle with the radius r. (from Ref. [2], *Small* **2011,** *7*, 2685-2702.)

1.2.2 Comparison among classical nucleation, spinodal decomposition, and nonclassical nucleation based on thermodynamics

There are three different scenario of the nucleation in the solution: classical nucleation, spinodal decomposition, and nonclassical nucleation.[11] (Fig. 1.4) In the classical nucleation theory, high thermodynamic energy barrier exists as a huddle for homogeneous nucleation because of high surface-to-volume ratio of the nucleus. Thermodynamics of the homogeneous nucleation can be expressed as a function of a radius of nucleus regarding the competition between the surface energy and the bulk free energy. The free energy change of homogeneous nucleation is written as

$$\Delta G_{\mathrm{homo}}(r) = 4\pi r^2\gamma + 4/3\pi r^3\Delta G_{\mathrm{v}}$$

where r is the radius of the spherical nucleus, γ is the surface energy per area, and ΔG_{v} is the bulk energy per volume. It should be noted that γ and ΔG_{v} are constant in the classical model. A critical radius, $\mathrm{r}^* = -2\gamma/\Delta G_{\mathrm{v}}$, can be derived if the condition $\mathrm{d}[\Delta G_{\mathrm{homo}}(r)]/\mathrm{d}r = 0$, is fulfilled. The nuclei with the size larger than the critical radius can grow into larger particles, whereas the smaller counterparts will redissolve into the solution. Notably, this energy barrier limits the random formation and growth of particles, rather induces the burst of nucleation in highly supersaturated solution. Alternately, the most distinct character of spinodal decomposition is an absence of free energy barrier. In this model, the destabilizing effect of the surface energy of the nuclei is negligible that a phase separation occurs spontaneously under spinodal decomposition.

Then, how about nonclassical nucleation? Energetics of nonclassical nucleation can be described in between them of classical nucleation with high energy barrier and spinodal decomposition without energy barrier. Moreover, γ and ΔG_v are not constant according to the size change of particles. Unique conditions of nonclassical nucleation lead the intermediates structures to be stabilized. These findings imply nonclassical pathway would be more energetically favorable than classical counterparts by lowering the energy barrier for nucleation.

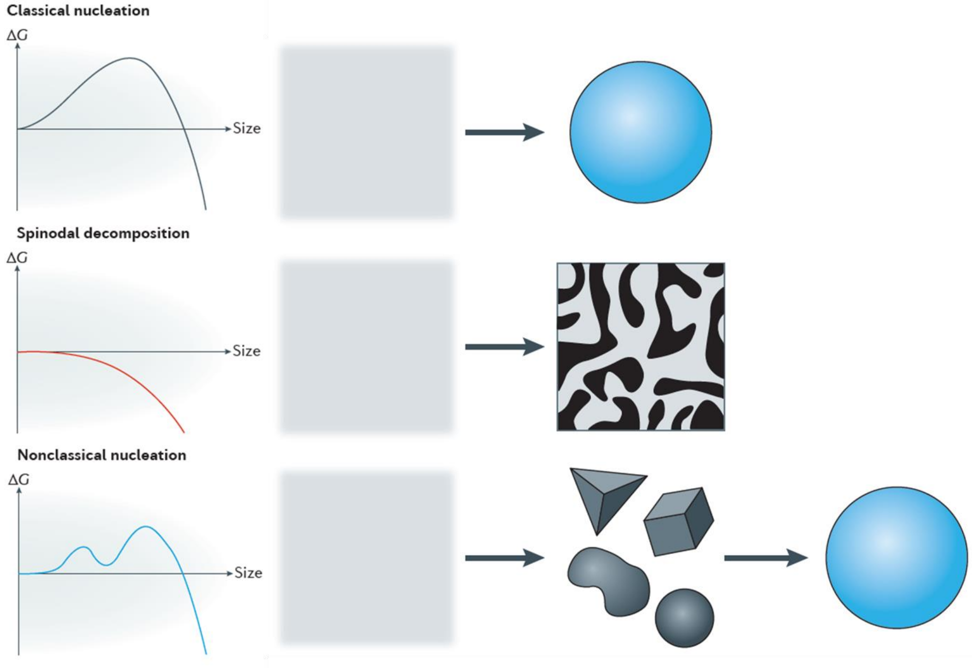

Figure 1.4 Comparison among classical nucleation, spinodal decomposition, and nonclassical nucleation based on thermodynamics. (from Ref. [11], *Nat. Rev. Mater.* **2016,** *1*, 16034.)

1.3 Synthesis and mechanism studies on the synthesis of nanoparticles and nanoclusters

Whereas the interests on the monodispersity of nanoparticles guide the fundamental understandings on the nanoparticle synthesis to be correlated with the classic theory of colloidal chemistry, subsequent interests on the nonclassical phenomena, which are unique in nanochemistry, are recently enhancing owing to advanced characterization technologies. Nonclassical nucleation and growth, which demonstrates new features of nucleation and growth within the nanometer scales, has been accepted as independent theories since last two decades.[11-16] Energetically metastable products, so called “nanoclusters”, are emerged during the synthesis of nanoparticles from molecular precursors to nanoparticles, and the intermediates can be aggregated into larger sized nanoparticles. Nowadays, these nanoclusters are attracting rising interests of material scientists and engineers, because the clusters are composed of more atoms than molecules, but less atoms than nano-sized materials.

1.3.1 Noble metals

The synthesis of gold nanoparticles, the most representative noble metal nanoparticles, is first developed in 1951 by Turkevich *et al.* using citrate as both reductant and stabilizing ligands in aqueous media (Figure 1.5a).[17] In 1994, a breakthrough on the synthesis of Au NPs is reported by Brust and Schriffin by introducing biphasic system.[18-19] Gold precursors are transferred to the organic solvent by tetraoctylammonium bromide and transferred precursors are reduced by sodium borohydride and stabilized with the aid of alkanethiolate (Fig. 1.5b). Whereas the product of Turkevich method has the size of 10 to 100 nm, the product of Brust method have distinctly smaller size of 1.5 to 3.5 nm. Interestingly, localized surface plasmonic resonance of nanosized Au NPs phased out for NPs smaller than two nanometers, rather they show characteristic absorption by their unique core-ligand structure.[20-22] Subsequently, NPs less than two nanometers are separated by polyacrylamide gel electrophoresis (PAGE) and characterized as nanoclusters which have distinct number of gold and ligand (i.e. $Au_x(SR)_y$).[23-24] After that, various kinds of gold nanoclusters with different size and ligands are synthesized and precisely characterized with single-crystal x-ray diffraction crystallography (Fig. 1.6).[25-30]

Recent mechanism studies showing discrete number of gold atoms during the synthesis refer the nonclassical nucleation and growth as a universal concept in gold nanoparticle synthesis.[31-36] Kinetic control on the growth by controlling precursor-to-ligand ratio shows that gold nanoclusters or gold complexes are metastable intermediates between the precursor and nanoparticles in the synthesis of gold nanoparticles (Fig. 1.7).[23, 34] Moreover, interesting structural evolution from molecules to crystalline nanoparticles are reported for better understanding the crystallization process.[33] The transition of gold nanoclusters from a non-fcc to a fcc structure is in the size range from Au_{144} to Au_{187} (Fig. 1.8).

For silver, monolayer protected clusters are successfully synthesized and characterized to have distinct absorption and photoluminescence (Fig 1.9).[37-53] Although silver and gold are in the same group, silver nanoclusters are shown to have more complicated surface structure than gold counterparts. Compare to the oligomeric $Au_n(SR)_{n+1}$ staple motifs frequently observed in gold nanoclusters, Ag and SR can compose three-dimensional surface motifs, as each silver atom can bind up to three –SR groups and each –SR also bind to three Ag atoms. For example, the surface of $[Ag_{44}(SR)_{30}]^{4-}$ nanocluster is protected by a $Ag_2(SR)_5$ "mount" motif with four anchoring S atoms (Fig. 1.9a).[45-46]

Moreover, R. G. Finke *et al.* reported the synthesis of iridium nanoclusters under hydrogen reduction condition with mechanistic studies showing Finke-Watzky 2-step mechanism, slow, continuous nucleation and fast autocatalytic growth (Fig. 1.10a).[12] The autocatalytic growth mechanism is extended to 4-step mechanism for the explanation of the synthesis of platinum nanoclusters (Fig. 1.10b).[54-55]

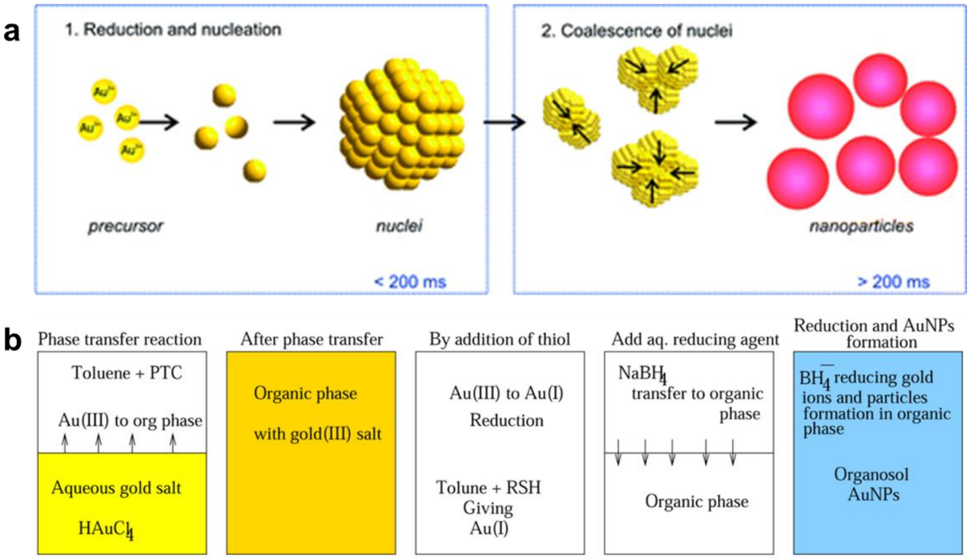

Figure 1.5 Overview of the gold nanoparticle synthesis by (a) Turkevich method and (b) Brust-Schiffrin method. ((a) from Ref. [56], *ACS Nano* **2010,** *4*, 1076-1082., and (b) from Ref. [57], *Langmuir* **2013,** *29*, 9863-9873.)

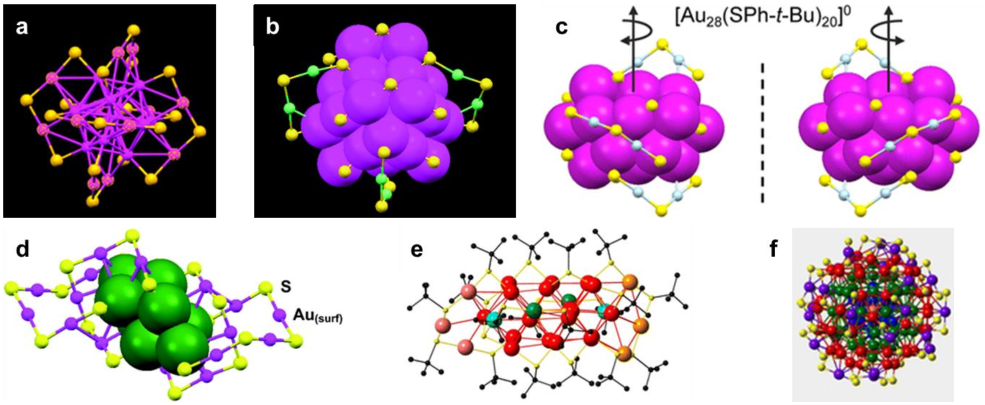

Figure 1.6 Crystal structure of the representative gold nanoclusters. (a) $Au_{25}(SR)_{18}$, (b) $Au_{36}(SR)_{24}$, (c) $Au_{28}(SR)_{20}$, (d) $Au_{24}(SR)_{20}$, (e) $Au_{30}S(SR)_{18}$ and (f) $Au_{133}(SR)_{52}$. ((a) from Ref. [25], *J. Am. Chem. Soc.* **2008,** *130*, 5883-5885., (b) from Ref. [26], *Angew. Chem. Int. Ed. Engl.* **2012,** *51*, 13114-13118., (c) from Ref. [27], *J. Am. Chem. Soc.* **2013,** *135*, 10011-10013., (d) from Ref. [28], *Nanoscale* **2014,** *6*, 6458-6462., (e) from Ref. [29], *J. Am. Chem. Soc.* **2014,** *136*, 5000-5005., and (f) from Ref. [30], *J. Am. Chem. Soc.* **2015,** *137*, 4610-4613.)

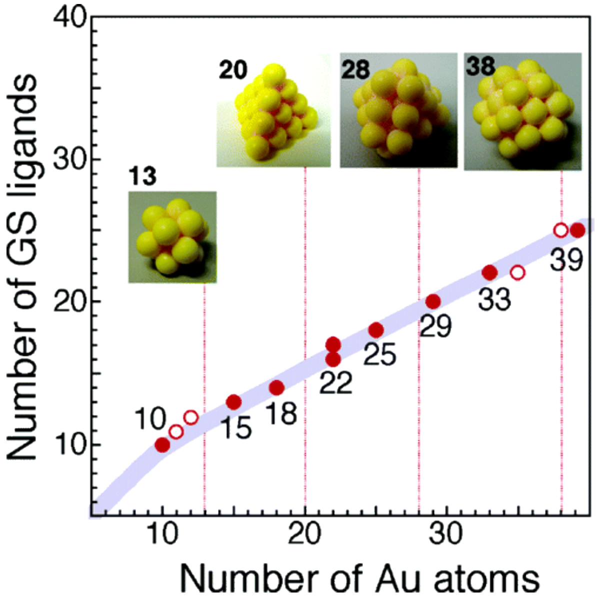

Figure 1.7 A plot of the chemical composition between gold atoms and glutathione ligands. The closed and open dots represent the most dominant and minor species observed in the mass spectrum. It should be noted that the size of these clusters are between the gold molecules such as sodium aurothiomalate and the plasmonic gold nanoparticles. (from Ref. [23], *J. Am. Chem. Soc.* **2005**, 127, 5261-5270.)

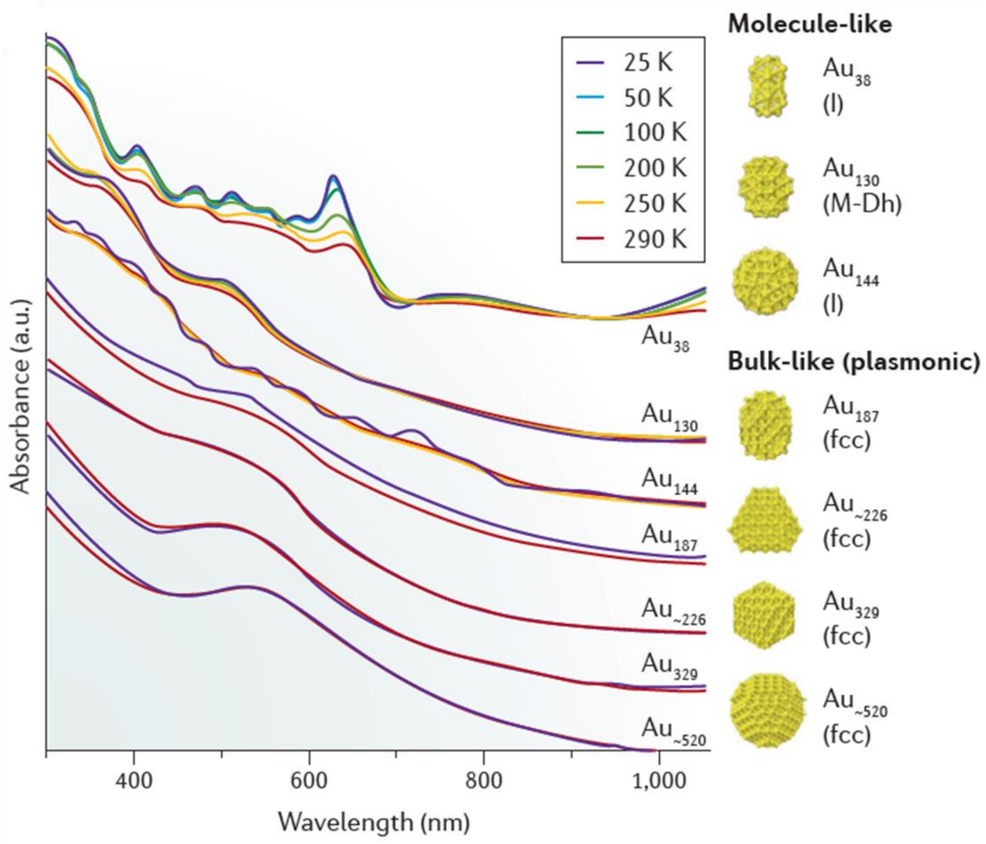

Figure 1.8 Size-dependent absorption of gold nanoclusters. Whereas the clusters with hundreds of gold atoms show bulk-like plasmonic absorption, smaller clusters show molecule-like characteristic absorption. (from Ref. [11], *Nat. Rev. Mater.* **2016,** *1*, 16034.)

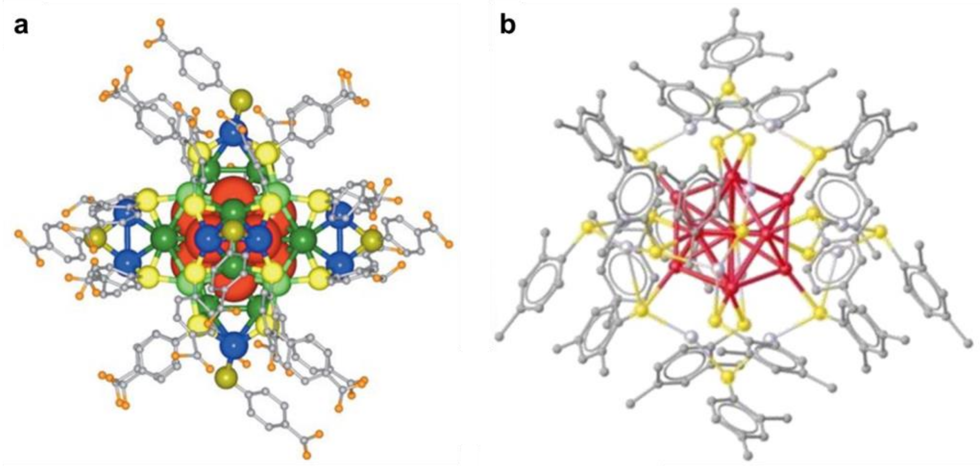

Figure 1.9 Crystal structure of the representative silver nanoclusters. (a) $[Ag_{44}(SR)_{30}]^{4-}$ and (b) $[Ag_{25}(SR)_{18}]^{-}$. ((a) from Ref. [45], *Nature* **2013,** *501*, 399-402., and (b) from Ref. [51], *J. Am. Chem. Soc.* **2015,** *137*, 11578-11581.)

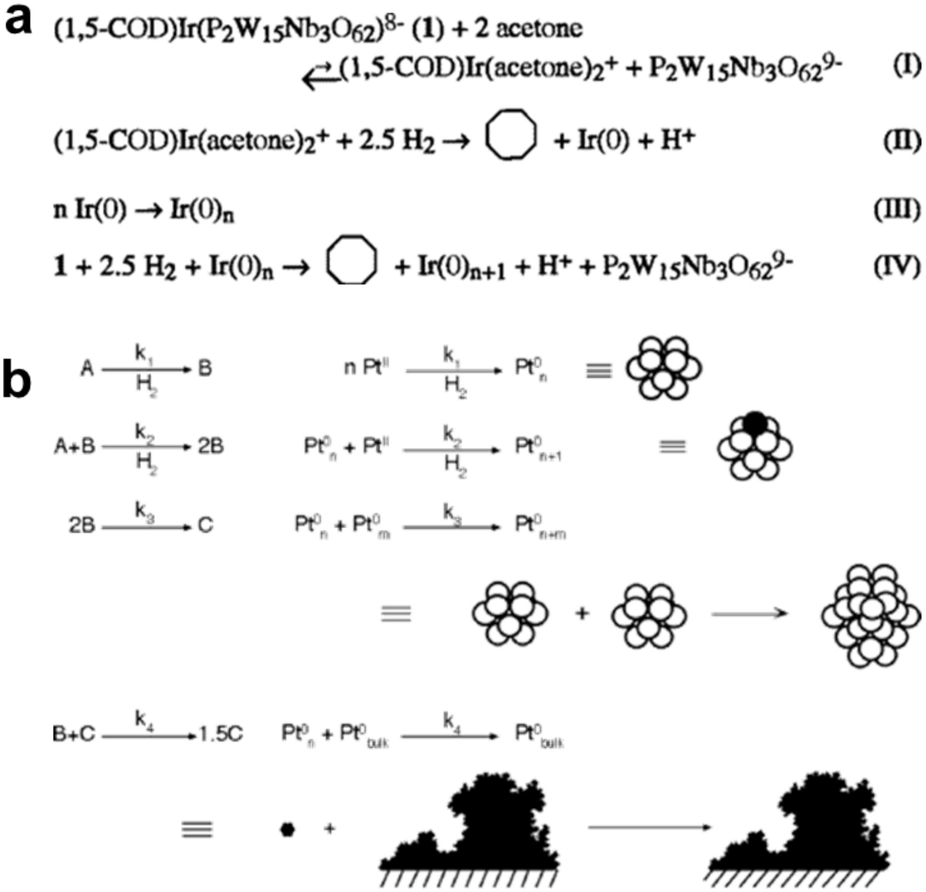

Figure 1.10 Suggested synthesis mechanism of metal nanoclusters by R. G. Finke *et al.* (a) 2-step Finke-Watzky mechanism and (b) 4-step Finke-Watzky mechanism. ((a) from Ref. [12], *J. Am. Chem. Soc.* **1997,** *119*, 10382-10400., and (b) from Ref. [55], *J. Am. Chem. Soc.* **2005,** *127*, 8179-8184.)

1.3.2 Metal chalcogenides

Since the synthesis of highly monodisperse II-VI metal chalcogenide QD was reported,[58] the mechanistic understandings on the synthesis are subsequently studied by optical characterization such as UV-Vis and PL.[8, 59-65] Several factors including ligands stabilizing the metal precursor and impurities in the chalcogenide source are pointed out as critical causes at the nucleation stage.[59, 64] Notably, the synthesis of CdSe QD is shown to follow nonclassical nucleation and growth pathway by several detailed studies (Fig. 1.11).[60-62, 66-69] CdSe nanoclusters of discrete sizes with a motif of a bulk structure have been successfully observed and synthesized by several groups.[70-73] For example, certain numbered clusters, $(CdSe)_n$ (n = 13, 19, 33, 34) can be distinctly captured in the mild temperature condition (Fig. 1.12) [73] and single crystallized nanoclusters with mixed motif of zinc blende and wurtzite or single zinc blende motif are also synthesized.[72] These clusters are all shown to act as bulk semiconductor in that they follows Varshni's law,[74] which correlates size-dependent band gap energy and the temperature (Fig. 1.13).[72, 75] Interestingly, these CdSe nanoclusters do not always grow into smaller ones to larger ones. At the early stage of the synthesis of CdSe nanoribbon, $(CdSe)_{34}$ nanoclusters are observed before the formation of smaller $(CdSe)_{13}$ nanoclusters (Fig. 1.11b).[75-77] This result implies that the thermodynamics of the nanoparticle formation is much more complicated than those of the classical model.

Recently, the synthesis of magic-sized metal chalcogenide nanoclusters is extended to other semiconductor nanoclusters.[67, 78-80] Especially, overall growth process from indium and phosphine source to InP nanoclusters and nanoparticles is successfully examined by consistent results of mass spectrometry and absorption spectroscopy (Fig. 1.14).

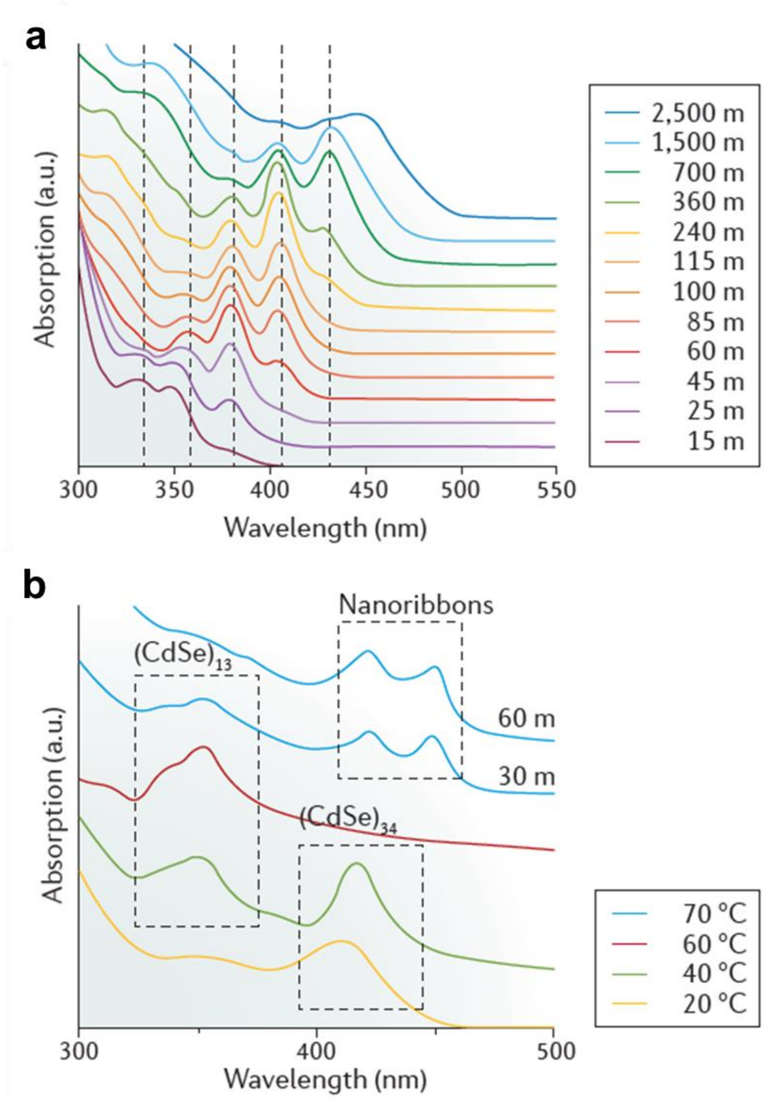

Figure 1.11 (a) Time-dependent UV-Vis absorption spectra observed during the synthesis of CdSe nanoparticles. Vertical lines show the absorbance of the discrete magic-sized CdSe clusters, (b) UV-Vis absorption spectra observed during the synthesis of CdSe nanoribbons. (from Ref. [11], *Nat. Rev. Mater.* **2016,** *1*, 16034.)

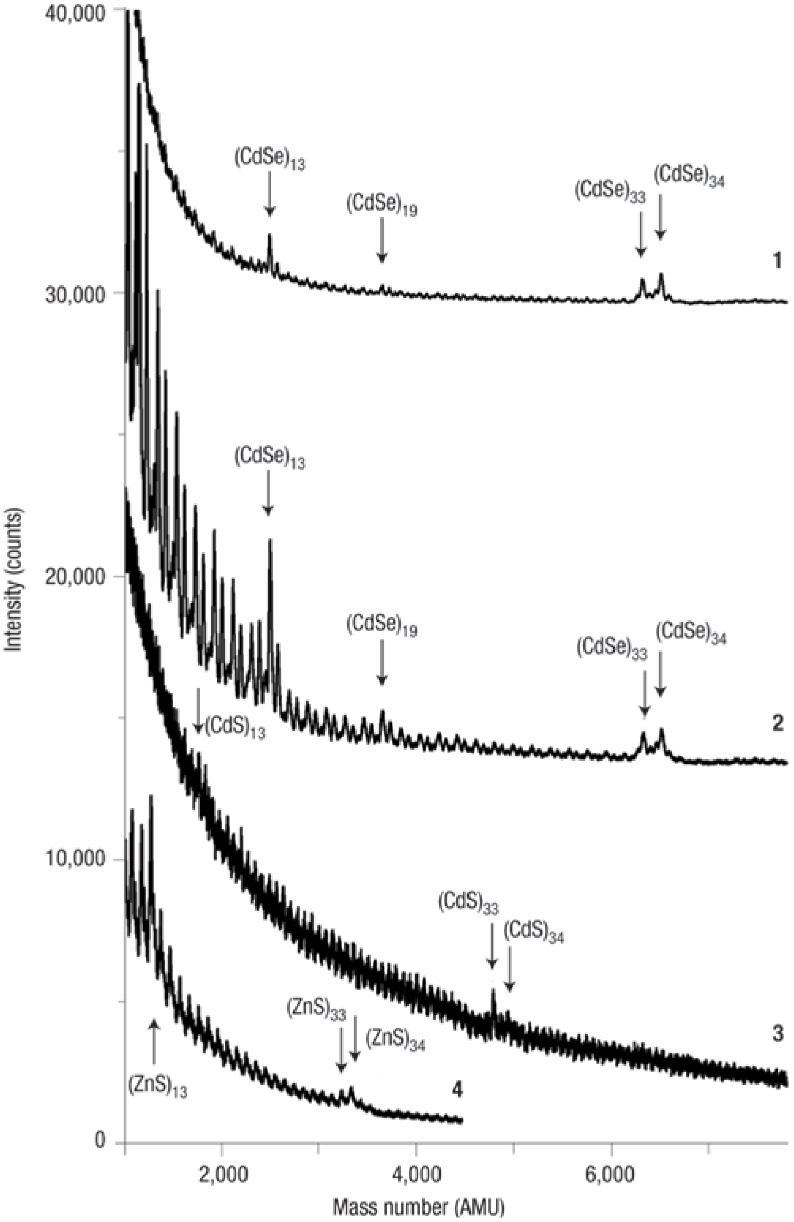

Figure 1.12 Mass spectra of ultrastable magic-sized CdSe, CdS, and ZnS nanoclusters observed without purification. (from Ref. [73], *Nat. Mater.* **2004,** *3*, 99-102.)

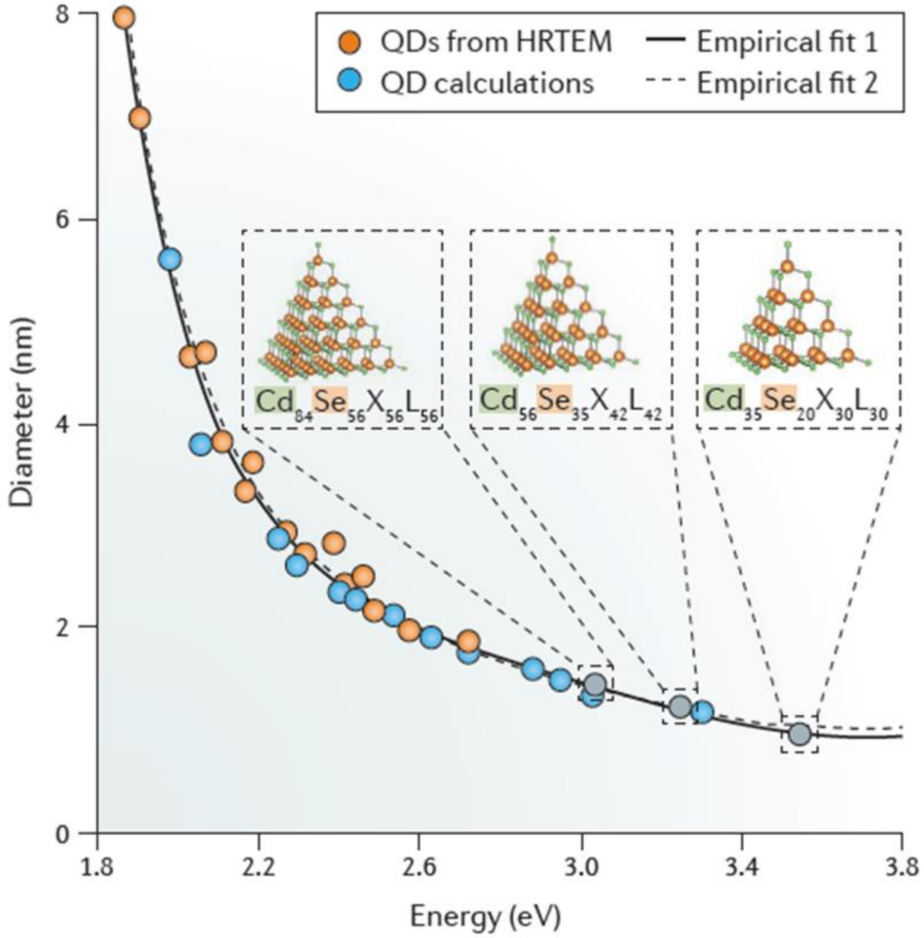

Figure 1.13 Size dependence of the bandgap energy of CdSe nanoparticles and nanoclusters. The structures of the clusters are presented in the inset and their bandgap energies are shown as grey dots. Here, empirical fit 1 is calculated for data points of both nanoparticles and nanoclusters, but empirical fit 2 is only for nanoparticles. (from Ref. [11], *Nat. Rev. Mater.* **2016,** *1*, 16034.)

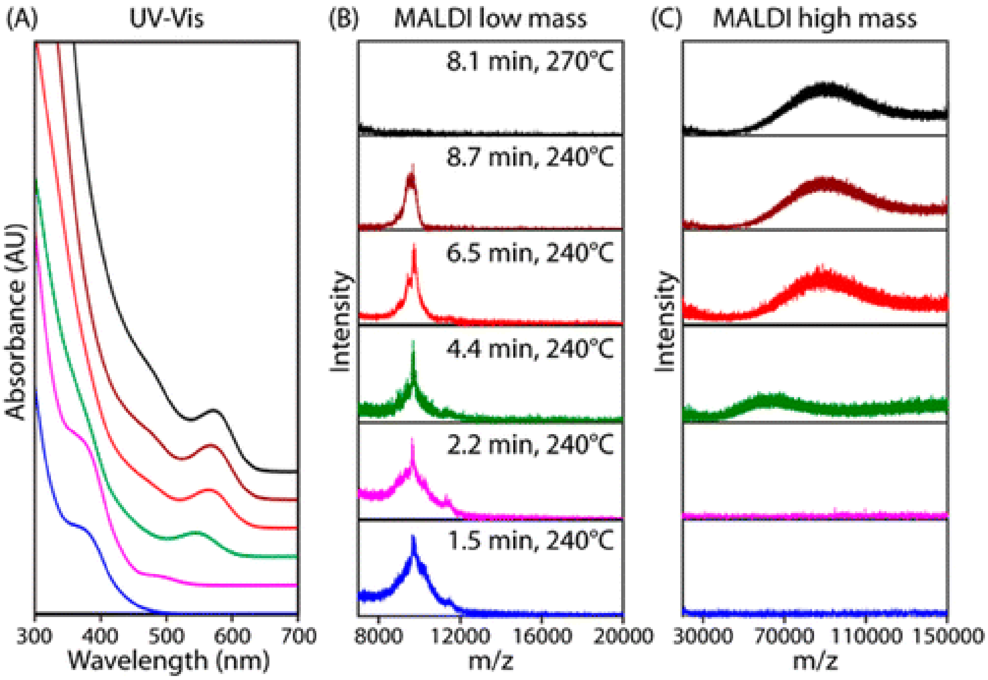

Figure 1.14 (A) UV-Vis absorption spectra observed during the synthesis of InP nanoparticles. (B,C) (B) Low mass and (C) High mass spectra observed during the synthesis of InP nanoparticles. Discrete size distribution, which refers to the nonclassical phenomena, is observed by mass spectra. (from Ref. [79], *J. Am. Chem. Soc.* **2016,** *138*, 13469-13472.)

1.3.3 Metal oxides

As many kinds of syntheses can guide the formation of metal oxide nanoparticles, here we are focused on the most representative pathways, heat-up method, which can lead high monodispersity in facile one-pot reaction.[81] Compare to the hot-injection method, which induce the nucleation by rapid supplement and cooling for supersaturation of monomers, the heat-up process can easily control the temperature condition which is critical for the decomposition of precursor. On account of consistent results of the experiment and theoretical simulation, the heat-up synthesis of the monodisperse nanoparticles is successfully explained as the gradual accumulation of the precursors can induce the burst nucleation and further separated growth without nucleation at aging period.[82]

However, the formation mechanisms of metal oxide nanoparticles have not been clearly demonstrated because of complicated and rapid reaction condition and lack of characterization tools for elucidating sub-nanometer sized intermediates. As introduced in previous parts, several detailed studies of the formation of the noble metal or metal chalcogenide nanomaterials have been performed using optical characterization methods,[31, 63-64] but the techniques are not easy to adopt to metal oxide nanoparticles which have no characteristic absorption spectrum. Some recent results show nonclassical nucleation and growth mechanism of the metal oxide nanoparticle synthesis by using MALDI-TOF MS and *in situ* total scattering (Fig. 1.15 and 1.16).[15, 83] Those results show intermediate structure of metal-oxo clusters in common.

Here, we should note the metal-oxo clusters shown in the metal oxide synthesis, because the synthesis of metal-oxo clusters are dated back to 1980s as an independent area of inorganic chemistry.[84-92] Many kinds of metal-oxo complexes or clusters have been synthesized and characterized for basic scientific purpose and potential applications such as molecular magnet.[93] (Fig. 1.17) These studies provide detailed crystallographic and spectroscopic information of the crystals. Nowadays, many metal-oxo clusters whose structure is similar to metal oxide solids were found in polyoxometalates.[94-96] These polyoxometalate clusters usually consist of transition metal cations (M), oxygen atoms and additional heteroatom (X), such as Lindqvist (M_6O_{19})[97], Anderson (XM_6O_{24})[98], Keggin ($XM_{12}O_{40}$),[99] Wells–Dawson ($X_2M_{18}O_{62}$)[100] and Preyssler ($P_5W_{30}O_{110}$)[101] clusters (Fig. 1.18). Whereas the metal-oxo clusters are similarly acquired from totally different origins, such as geology[102-103] or biology[104-105], the interdisciplinary of the metal-oxo species is enough to gain interests for industrial applications.

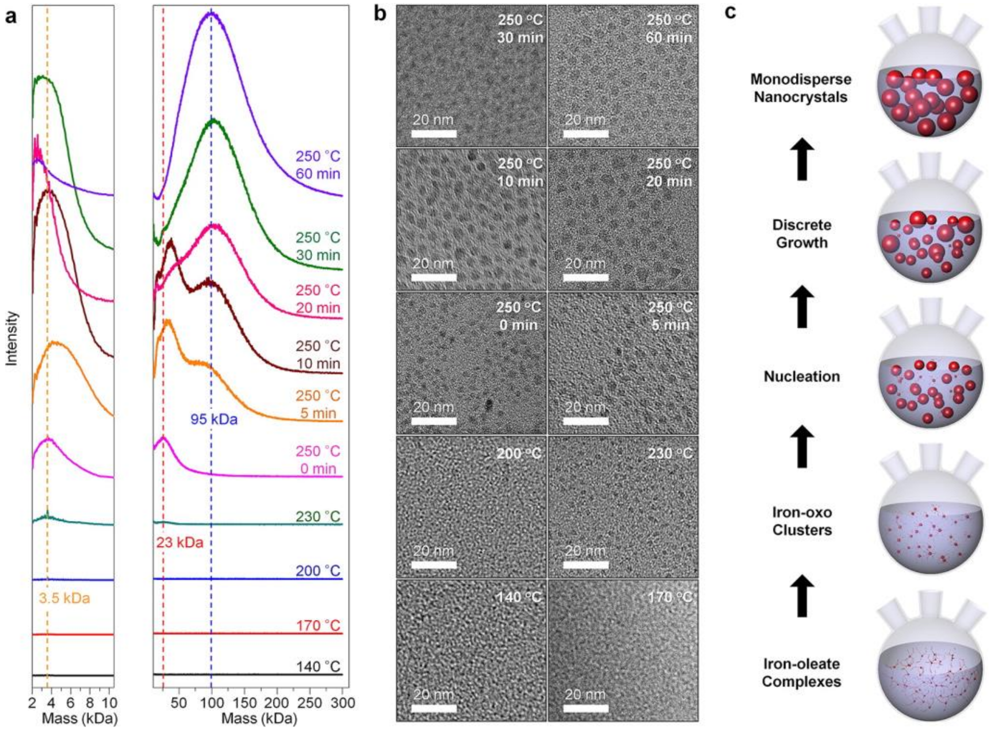

Figure 1.15 (a,b) Combinatorial growth mechanism studies on extremely small iron oxide nanoparticle synthesis showing nonclassical nucleation and growth process by using (a) mass spectrometry and (b) transmission electron microscopy. (c) Suggested reaction mechanism of extremely small iron oxide nanoparticle synthesis. (from Ref. [15], *J. Am. Chem. Soc.* **2013,** *135*, 2407-2410.)

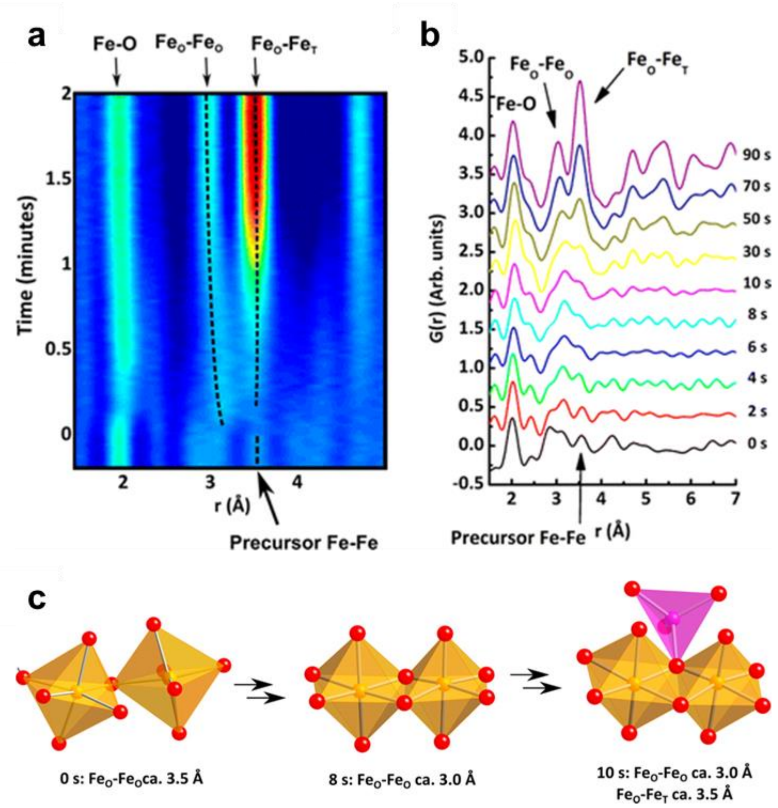

Figure 1.16 (a) Contour plot of the low *r*-range pair distribution functions (PDFs) during the maghemite nanoparticle formation from 4 M ammonium iron(III) citrate solutions in hydrothermal condition at 320 ºC and 250 bar. The dotted lines refer to the evolution of the new distinct Fe-Fe peaks. (b) Selected PDFs from the initial stages. (c) Structure observed in the low *r*-range at the early stage. Octahedrally coordinated iron (yellow polyhedron) and tetrahedrally coordinated iron (pink polyhedron) are coordinated by point-sharing after 10 seconds. (from Ref. [83], *ACS Nano* **2014,** *8*, 10704-10714.)

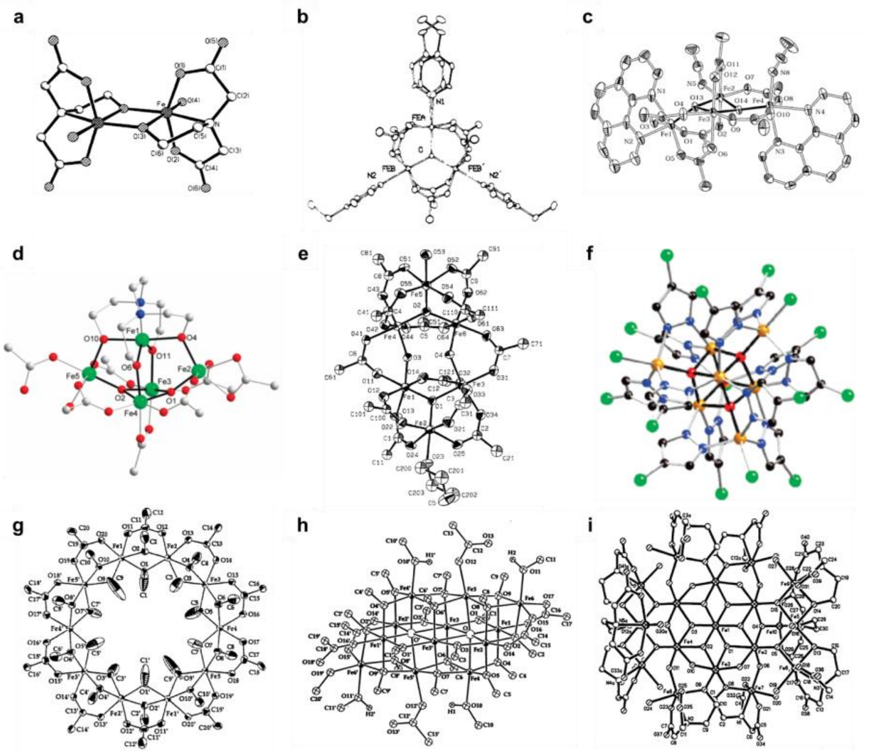

Figure 1.17 Crystal structure of the representative metal-oxo clusters having (a) Fe_2O_2 core, (b) Fe_3O core, (c) Fe_4O_2 core, (d) Fe_5O_2 core, (e) $Fe_6O_2(OH)_2$ core, (f) Fe_8O_4 core, (g) $Fe_{10}O_{10}$ core, (h) $Fe_{12}O_2$ core and (i) Fe_{19} core. ((a) and (i) from Ref. [85], *J. Am. Chem. Soc.* **1995,** *117*, 2491-2502., (b) from Ref. [84], *J. Am. Chem. Soc.* **1984,** *106*, 7984-7985., (c) from Ref. [91], *Inorganica Chim. Acta* **2004,** *357*, 1345-1354., (d) from [90], *Inorg. Chem.* **2008,** *47*, 3318-3327., (e) from Ref. [87], *Inorg. Chem.* **1988,** *27*, 3067-3069., (f) from Ref. [89], *Inorg. Chem.* **2008,** *47*, 11734-11737., (g) from Ref. [92] *J. Am. Chem. Soc.* **1990,** *112*, 9629-9630., and (h) from Ref. [88], *Science* **1993,** *259*, 1302-1305)

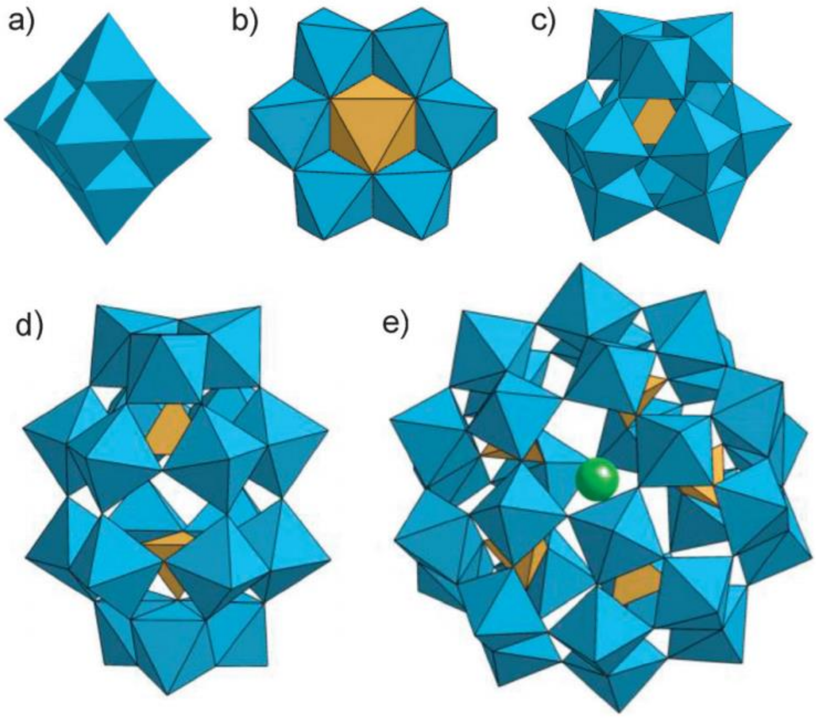

Figure 1.18 Polyhedral representation of some polyoxometalates. (a) Lindqvist, (b) Anderson, (c) Keggin, (d) Wells–Dawson and (e) Preyssler polyoxometallates. The blue octahedrons indicate the metal oxide core. (from Ref. [106], *Chem. Soc. Rev.* **2012,** *41*, 7537-7571.)

1.4 Dissertation overview

As referred in the introduction, understandings of the formation mechanism of nanoparticles are extremely essential not only for basic scientific research purpose, but also for controlled synthesis for further applications. Along with the advance of technologies, mechanistic approaches on the nanoparticle synthesis show that distinctive nonclassical models are needed to explain overall reaction pathway. Nanoclusters observed in the detailed studies can connect the missing-link between molecules and nanoparticles. The studies on the nanoclusters are gradually increasing as they can act as distinctive molecules. The current thesis focuses on the characterization and molecular-level understandings on the nanoparticle and nanocluster synthesis. Overall studies are correlated to the effect of ligands on the inorganic core. By controlling the reaction condition, the synthesis of iron oxide nanoparticles can be studied in detail and the phenomena at the early stage are successfully demonstrated. Moreover, the synthesis of doped noble metal nanoclusters is expanded to non-noble metal dopant by introducing assisting ligands.

This dissertation consists of two topics related to nanoclusters. In the first part (Chapter 2), the synthesis of iron oxide nanoparticles is delicately controlled by limiting thermal decomposition and studied in detail by introducing combinatorial analysis technique, such as MALDI-TOF MS, NMR, absorption spectroscopies, TEM, DFT calculation and *in situ* X-ray scattering. Molecular-level understandings on the synthesis are successfully done from the starting materials to nanoparticles. As a result, widely used precursor, iron-oleate complex, is shown to have trinuclear-oxo cluster structure, and it can be continuously grown into sub-nanometer iron-oxo clusters and iron oxide nanoparticles without showing distinct nucleation stage. Atom-level growth can be proceeded, because the ligand stabilizing effect on the metal-oxo core is amplified in the thermal decomposition limited condition and further nonhydrolytic sol-gel like condensation is also limited at low temperature condition. On account of the analogy of various metal oxide nanoparticle synthesis, the continuous growth process shown in this work suggests insightful information on the formation mechanism of various other metal oxide nanoparticles.

The second part (Chapter 3) describes non-noble metal doping to metal nanoclusters, which has been still challenging for non-gold noble metal nanoclusters. Cadmium-doped silver nanoclusters ($Cd_{12}Ag_{32}(SePh)_{36}$) are successfully synthesized with the aid of phosphines to the reaction and characterized to have unique absorbance and near-infrared (NIR) photoluminescence. X-ray single crystallography uncovers the structure of cadmium-doped silver nanoclusters to have asymmetric $Ag_4@Ag_{24}$ metal core structure and four $Cd_3Ag(SePh)_9$ surface motifs. The electronic structure of nanoclusters is revealed by “super-atom” theory and time-dependent density functional theory (TD-DFT) calculation. $Cd_{12}Ag_{32}(SePh)_{36}$ is a 20-

electron superatom and its theoretical chiral optical response is comparable to that of the well-known $Au_{38}(SR)_{24}$ cluster. Ligand-assisted synthesis of nanoclusters may pave the way for introducing other active metals into noble metal clusters.

1.5 References

[1] LaMer, V. K.; Dinegar, R. H., Theory, Production and Mechanism of Formation of Monodispersed Hydrosols, *J. Am. Chem. Soc.* **1950,** *72*, 4847–4854.

[2] Kwon, S. G.; Hyeon, T., Formation mechanisms of uniform nanocrystals *via* hot-injection and heat-up methods, *Small* **2011,** *7*, 2685–2702.

[3] Sugimoto, T., Preparation of monodispersed colloidal particles, *Adv. Colloid Interface Sci.* **1987,** *28*, 65–108.

[4] Peng, X.; Wickham, J.; Alivisatos, A. P., Kinetics of II-VI and III-V Colloidal Semiconductor Nanocrystal Growth: "Focusing" of Size Distributions, *J. Am. Chem. Soc.* **1998,** *120*, 5343–5344.

[5] Sugimoto, T., *Monodispersed Particles*. Elsevier: New York, **2001**.

[6] Talapin, D. V.; Rogach, A. L.; Haase, M.; Weller, H., Evolution of an Ensemble of Nanoparticles in a Colloidal Solution: Theoretical Study, *J. Phys. Chem. B* **2001,** *105*, 12278–12285.

[7] Rogach, A. L.; Talapin, D. V.; Shevchenko, E. V.; Kornowski, A.; Haase, M.; Weller, H., Organization of Matter on Different Size Scales: Monodisperse Nanocrystals and Their Superstructures, *Adv. Funct. Mater.* **2002,** *12*, 653–664.

[8] Talapin, D. V.; Rogach, A. L.; Shevchenko, E. V.; Kornowski, A.; Haase, M.; Weller, H., Dynamic distribution of growth rates within the ensembles of

colloidal II-VI and III-V semiconductor nanocrystals as a factor governing their photoluminescence efficiency, *J. Am. Chem. Soc.* **2002,** *124*, 5782–5790.

[9] Kabalnov, A. S.; Shchukin, E. D., Ostwald ripening theory: applications to fluorocarbon emulsion stability, *Adv. Colloid Interface Sci.* **1992,** *38*, 69–97.

[10] Sugimoto, T., Underlying mechanisms in size control of uniform nanoparticles, *J. Colloid Interface Sci.* **2007,** *309*, 106–118.

[11] Lee, J.; Yang, J.; Kwon, S. G.; Hyeon, T., Nonclassical nucleation and growth of inorganic nanoparticles, *Nat. Rev. Mater.* **2016,** *1*, 16034.

[12] Watzky, M. A.; Finke, R. G., Transition Metal Nanocluster Formation Kinetic and Mechanistic Studies. A New Mechanism When Hydrogen Is the Reductant: Slow, Continuous Nucleation and Fast Autocatalytic Surface Growth, *J. Am. Chem. Soc.* **1997,** *119*, 10382–10400.

[13] Raiteri, P.; Gale, J. D., Water is the key to nonclassical nucleation of amorphous calcium carbonate, *J. Am. Chem. Soc.* **2010,** *132*, 17623–17634.

[14] Zheng, H.; Smith, R. K.; Jun, Y. W.; Kisielowski, C.; Dahmen, U.; Alivisatos, A. P., Observation of single colloidal platinum nanocrystal growth trajectories, *Science* **2009,** *324*, 1309–1312.

[15] Kim, B. H.; Shin, K.; Kwon, S. G.; Jang, Y.; Lee, H. S.; Lee, H.; Jun, S. W.; Lee, J.; Han, S. Y.; Yim, Y. H.; Kim, D. H.; Hyeon, T., Sizing by weighing: characterizing sizes of ultrasmall-sized iron oxide nanocrystals using MALDI-TOF mass spectrometry, *J. Am. Chem. Soc.* **2013,** *135*, 2407–2410.

[16] Wang, F.; Richards, V. N.; Shields, S. P.; Buhro, W. E., Kinetics and Mechanisms of Aggregative Nanocrystal Growth, *Chem. Mater.* **2013,** *26*, 5–21.

[17] Turkevich, J.; Stevenson, P. C.; Hillier, J., A study of the nucleation and growth processes in the synthesis of colloidal gold, *Discuss. Faraday Soc.* **1951,** *11*, 55.

[18] Brust, M.; Fink, J.; Bethell, D.; Schiffrin, D. J.; Kiely, C., Synthesis and reactions of functionalised gold nanoparticles, *J. Chem. Soc., Chem. Commun.* **1995**, 1655.

[19] Brust, M.; Walker, M.; Bethell, D.; Schiffrin, D. J.; Whyman, R., Synthesis of thiol-derivatised gold nanoparticles in a two-phase Liquid–Liquid system, *J. Chem. Soc., Chem. Commun.* **1994,** *0*, 801–802.

[20] Alvarez, M. M.; Khoury, J. T.; Schaaff, T. G.; Shafigullin, M. N.; Vezmar, I.; Whetten, R. L., Optical Absorption Spectra of Nanocrystal Gold Molecules, *J. Phys. Chem. B* **1997,** *101*, 3706–3712.

[21] Schaaff, T. G.; Whetten, R. L., Controlled Etching of Au:SR Cluster Compounds, *J. Phys. Chem. B* **1999,** *103*, 9394–9396.

[22] Schaaff, T. G.; Whetten, R. L., Giant Gold−Glutathione Cluster Compounds: Intense Optical Activity in Metal-Based Transitions, *J. Phys. Chem. B* **2000,** *104*, 2630–2641.

[23] Negishi, Y.; Nobusada, K.; Tsukuda, T., Glutathione-protected gold clusters revisited: bridging the gap between gold(I)-thiolate complexes and

thiolate-protected gold nanocrystals, *J. Am. Chem. Soc.* **2005,** *127*, 5261–5270.

[24] Negishi, Y.; Takasugi, Y.; Sato, S.; Yao, H.; Kimura, K.; Tsukuda, T., Kinetic stabilization of growing gold clusters by passivation with thiolates, *J. Phys. Chem. B* **2006,** *110*, 12218–12221.

[25] Zhu, M.; Aikens, C. M.; Hollander, F. J.; Schatz, G. C.; Jin, R., Correlating the crystal structure of a thiol-protected Au_{25} cluster and optical properties, *J. Am. Chem. Soc.* **2008,** *130*, 5883–5885.

[26] Zeng, C.; Qian, H.; Li, T.; Li, G.; Rosi, N. L.; Yoon, B.; Barnett, R. N.; Whetten, R. L.; Landman, U.; Jin, R., Total structure and electronic properties of the gold nanocrystal $Au_{36}(SR)_{24}$, *Angew. Chem. Int. Ed. Engl.* **2012,** *51*, 13114–13118.

[27] Zeng, C.; Li, T.; Das, A.; Rosi, N. L.; Jin, R., Chiral structure of thiolate-protected 28-gold-atom nanocluster determined by X-ray crystallography, *J. Am. Chem. Soc.* **2013,** *135*, 10011–10013.

[28] Das, A.; Li, T.; Li, G.; Nobusada, K.; Zeng, C.; Rosi, N. L.; Jin, R., Crystal structure and electronic properties of a thiolate-protected Au_{24} nanocluster, *Nanoscale* **2014,** *6*, 6458–6462.

[29] Crasto, D.; Malola, S.; Brosofsky, G.; Dass, A.; Hakkinen, H., Single crystal XRD structure and theoretical analysis of the chiral $Au_{30}S(S\text{-}t\text{-}Bu)_{18}$ cluster, *J. Am. Chem. Soc.* **2014,** *136*, 5000–5005.

[30] Dass, A.; Theivendran, S.; Nimmala, P. R.; Kumara, C.; Jupally, V. R.;

Fortunelli, A.; Sementa, L.; Barcaro, G.; Zuo, X.; Noll, B. C., Au_{133}(SPh-*t*Bu)$_{52}$ nanomolecules: X-ray crystallography, optical, electrochemical, and theoretical analysis, *J. Am. Chem. Soc.* **2015,** *137*, 4610–4613.

[31] Goulet, P. J.; Lennox, R. B., New insights into Brust-Schiffrin metal nanoparticle synthesis, *J. Am. Chem. Soc.* **2010,** *132*, 9582–9584.

[32] Polte, J.; Ahner, T. T.; Delissen, F.; Sokolov, S.; Emmerling, F.; Thunemann, A. F.; Kraehnert, R., Mechanism of gold nanoparticle formation in the classical citrate synthesis method derived from coupled in situ XANES and SAXS evaluation, *J. Am. Chem. Soc.* **2010,** *132*, 1296–1301.

[33] Negishi, Y.; Nakazaki, T.; Malola, S.; Takano, S.; Niihori, Y.; Kurashige, W.; Yamazoe, S.; Tsukuda, T.; Hakkinen, H., A critical size for emergence of nonbulk electronic and geometric structures in dodecanethiolate-protected Au clusters, *J. Am. Chem. Soc.* **2015,** *137*, 1206–1212.

[34] Chen, T.; Luo, Z.; Yao, Q.; Yeo, A. X.; Xie, J., Synthesis of thiolate-protected Au nanoparticles revisited: U-shape trend between the size of nanoparticles and thiol-to-Au ratio, *Chem. Commun.* **2016,** *52*, 9522–9525.

[35] Yao, Q.; Yuan, X.; Fung, V.; Yu, Y.; Leong, D. T.; Jiang, D. E.; Xie, J., Understanding seed-mediated growth of gold nanoclusters at molecular level, *Nat. Commun.* **2017,** *8*, 927.

[36] Lu, Y.; Chen, W., Sub-nanometre sized metal clusters: from synthetic challenges to the unique property discoveries, *Chem. Soc. Rev.* **2012,** *41*, 3594–3623.

[37] Yu, J.; Patel, S. A.; Dickson, R. M., In vitro and intracellular production of peptide-encapsulated fluorescent silver nanoclusters, *Angew. Chem. Int. Ed. Engl.* **2007,** *46*, 2028–2030.

[38] Wu, Z.; Lanni, E.; Chen, W.; Bier, M. E.; Ly, D.; Jin, R., High yield, large scale synthesis of thiolate-protected Ag_7 clusters, *J. Am. Chem. Soc.* **2009,** *131*, 16672–16674.

[39] Rao, T. U.; Nataraju, B.; Pradeep, T., Ag_9 quantum cluster through a solid-state route, *J. Am. Chem. Soc.* **2010,** *132*, 16304–16307.

[40] Kumar, S.; Bolan, M. D.; Bigioni, T. P., Glutathione-stabilized magic-number silver cluster compounds, *J. Am. Chem. Soc.* **2010,** *132*, 13141–13143.

[41] Udaya Bhaskara Rao, T.; Pradeep, T., Luminescent Ag_7 and Ag_8 clusters by interfacial synthesis, *Angew. Chem. Int. Ed. Engl.* **2010,** *49*, 3925–3929.

[42] Guo, J.; Kumar, S.; Bolan, M.; Desireddy, A.; Bigioni, T. P.; Griffith, W. P., Mass spectrometric identification of silver nanoparticles: the case of $Ag_{32}(SG)_{19}$, *Anal. Chem.* **2012,** *84*, 5304–5308.

[43] Harkness, K. M.; Tang, Y.; Dass, A.; Pan, J.; Kothalawala, N.; Reddy, V. J.; Cliffel, D. E.; Demeler, B.; Stellacci, F.; Bakr, O. M.; McLean, J. A., $Ag_{44}(SR)_{30}^{4-}$: a silver-thiolate superatom complex, *Nanoscale* **2012,** *4*, 4269–4274.

[44] Bertorelle, F.; Hamouda, R.; Rayane, D.; Broyer, M.; Antoine, R.; Dugourd, P.; Gell, L.; Kulesza, A.; Mitric, R.; Bonacic-Koutecky, V.,

Synthesis, characterization and optical properties of low nuclearity liganded silver clusters: $Ag_{31}(SG)_{19}$ and $Ag_{15}(SG)_{11}$, *Nanoscale* **2013,** *5*, 5637–5643.

[45] Desireddy, A.; Conn, B. E.; Guo, J.; Yoon, B.; Barnett, R. N.; Monahan, B. M.; Kirschbaum, K.; Griffith, W. P.; Whetten, R. L.; Landman, U.; Bigioni, T. P., Ultrastable silver nanoparticles, *Nature* **2013,** *501*, 399–402.

[46] Yang, H.; Wang, Y.; Huang, H.; Gell, L.; Lehtovaara, L.; Malola, S.; Hakkinen, H.; Zheng, N., All-thiol-stabilized Ag_{44} and $Au_{12}Ag_{32}$ nanoparticles with single-crystal structures, *Nat. Commun.* **2013,** *4*, 2422.

[47] Yang, H.; Lei, J.; Wu, B.; Wang, Y.; Zhou, M.; Xia, A.; Zheng, L.; Zheng, N., Crystal structure of a luminescent thiolated Ag nanocluster with an octahedral Ag_6^{4+} core, *Chem. Commun.* **2013,** *49*, 300–302.

[48] Yang, H.; Wang, Y.; Zheng, N., Stabilizing subnanometer Ag(0) nanoclusters by thiolate and diphosphine ligands and their crystal structures, *Nanoscale* **2013,** *5*, 2674–2677.

[49] Baksi, A.; Bootharaju, M. S.; Chen, X.; Häkkinen, H.; Pradeep, T., $Ag_{11}(SG)_7$: A New Cluster Identified by Mass Spectrometry and Optical Spectroscopy, *J. Phys. Chem. C* **2014,** *118*, 21722–21729.

[50] Wickramasinghe, S.; Atnagulov, A.; Conn, B. E. C.; Yoon, B.; Barnett, R. N.; Griffith, W. P.; Landman, U.; Bigioni, T. P., $M_3Ag_{17}(SPh)_{12}$ Nanoparticles and Their Structure Prediction, *J. Am. Chem. Soc.* **2015,** *137*, 11550–11553.

[51] Joshi, C. P.; Bootharaju, M. S.; Alhilaly, M. J.; Bakr, O. M., $[Ag_{25}(SR)_{18}]^-$:

The "Golden" Silver Nanoparticle, *J. Am. Chem. Soc.* **2015,** *137*, 11578–11581.

[52] Xia, N.; Yang, J.; Wu, Z., Fast, high-yield synthesis of amphiphilic Ag nanoclusters and the sensing of Hg^{2+} in environmental samples, *Nanoscale* **2015,** *7*, 10013–10020.

[53] Bootharaju, M. S.; Burlakov, V. M.; Besong, T. M. D.; Joshi, C. P.; AbdulHalim, L. G.; Black, D. M.; Whetten, R. L.; Goriely, A.; Bakr, O. M., Reversible Size Control of Silver Nanoclusters via Ligand-Exchange, *Chem. Mater.* **2015,** *27*, 4289–4297.

[54] Besson, C.; Finney, E. E.; Finke, R. G., Nanocluster Nucleation, Growth, and Then Agglomeration Kinetic and Mechanistic Studies: A More General, Four-Step Mechanism Involving Double Autocatalysis, *Chem. Mater.* **2005,** *17*, 4925–4938.

[55] Besson, C.; Finney, E. E.; Finke, R. G., A mechanism for transition-metal nanoparticle self-assembly, *J. Am. Chem. Soc.* **2005,** *127*, 8179–8184.

[56] Polte, J.; Erler, R.; Thunemann, A. F.; Sokolov, S.; Ahner, T. T.; Rademann, K.; Emmerling, F.; Kraehnert, R., Nucleation and growth of gold nanoparticles studied via in situ small angle X-ray scattering at millisecond time resolution, *ACS Nano* **2010,** *4*, 1076–1082.

[57] Perala, S. R.; Kumar, S., On the mechanism of metal nanoparticle synthesis in the Brust-Schiffrin method, *Langmuir* **2013,** *29*, 9863–9873.

[58] Murray, C. B.; Norris, D. J.; Bawendi, M. G., Synthesis and

characterization of nearly monodisperse CdE (E = sulfur, selenium, tellurium) semiconductor nanocrystallites, *J. Am. Chem. Soc.* **1993,** *115*, 8706–8715.

[59] van Embden, J.; Mulvaney, P., Nucleation and growth of CdSe nanocrystals in a binary ligand system, *Langmuir* **2005,** *21*, 10226–10233.

[60] Kudera, S.; Zanella, M.; Giannini, C.; Rizzo, A.; Li, Y.; Gigli, G.; Cingolani, R.; Ciccarella, G.; Spahl, W.; Parak, W. J.; Manna, L., Sequential Growth of Magic-Size CdSe Nanocrystals, *Adv. Mater.* **2007,** *19*, 548–552.

[61] Chen, H. S.; Kumar, R. V., Discontinuous Growth of Colloidal CdSe Nanocrystals in the Magic Structure, *J. Phys. Chem. C* **2008,** *113*, 31–36.

[62] Yu, Q.; Liu, C.-Y., Study of Magic-Size-Cluster Mediated Formation of CdS Nanocrystals: Properties of the Magic-Size Clusters and Mechanism Implication, *J. Phys. Chem. C* **2009,** *113*, 12766–12771.

[63] Owen, J. S.; Chan, E. M.; Liu, H.; Alivisatos, A. P., Precursor conversion kinetics and the nucleation of cadmium selenide nanocrystals, *J. Am. Chem. Soc.* **2010,** *132*, 18206–18213.

[64] Evans, C. M.; Evans, M. E.; Krauss, T. D., Mysteries of TOPSe revealed: insights into quantum dot nucleation, *J. Am. Chem. Soc.* **2010,** *132*, 10973–10975.

[65] Wang, Y.; Zhang, Y.; Wang, F.; Giblin, D. E.; Hoy, J.; Rohrs, H. W.; Loomis, R. A.; Buhro, W. E., The Magic-Size Nanocluster $(CdSe)_{34}$ as a Low-Temperature Nucleant for Cadmium Selenide Nanocrystals; Room-Temperature Growth of Crystalline Quantum Platelets, *Chem. Mater.* **2014,**

26, 2233–2243.

[66] Dagtepe, P.; Chikan, V.; Jasinski, J.; Leppert, V. J., Quantized Growth of CdTe Quantum Dots; Observation of Magic-Sized CdTe Quantum Dots, *J. Phys. Chem. C* **2007,** *111*, 14977–14983.

[67] Evans, C. M.; Guo, L.; Peterson, J. J.; Maccagnano-Zacher, S.; Krauss, T. D., Ultrabright PbSe magic-sized clusters, *Nano Lett.* **2008,** *8*, 2896–2899.

[68] Zanella, M.; Abbasi, A. Z.; Schaper, A. K.; Parak, W. J., Discontinuous Growth of II−VI Semiconductor Nanocrystals from Different Materials, *J. Phys. Chem. C* **2010,** *114*, 6205–6215.

[69] Harrell, S. M.; McBride, J. R.; Rosenthal, S. J., Synthesis of Ultrasmall and Magic-Sized CdSe Nanocrystals, *Chem. Mater.* **2013,** *25*, 1199–1210.

[70] Soloviev, V. N.; Eichhofer, A.; Fenske, D.; Banin, U., Size-dependent optical spectroscopy of a homologous series of CdSe cluster molecules, *J. Am. Chem. Soc.* **2001,** *123*, 2354–2364.

[71] Soloviev, V. N.; Eichhöfer, A.; Fenske, D.; Banin, U., Molecular Limit of a Bulk Semiconductor: Size Dependence of the "Band Gap" in CdSe Cluster Molecules, *J. Am. Chem. Soc.* **2000,** *122*, 2673–2674.

[72] Beecher, A. N.; Yang, X.; Palmer, J. H.; LaGrassa, A. L.; Juhas, P.; Billinge, S. J.; Owen, J. S., Atomic structures and gram scale synthesis of three tetrahedral quantum dots, *J. Am. Chem. Soc.* **2014,** *136*, 10645–10653.

[73] Kasuya, A.; Sivamohan, R.; Barnakov, Y. A.; Dmitruk, I. M.; Nirasawa, T.; Romanyuk, V. R.; Kumar, V.; Mamykin, S. V.; Tohji, K.; Jeyadevan, B.;

Shinoda, K.; Kudo, T.; Terasaki, O.; Liu, Z.; Belosludov, R. V.; Sundararajan, V.; Kawazoe, Y., Ultra-stable nanoparticles of CdSe revealed from mass spectrometry, *Nat. Mater.* **2004,** *3*, 99–102.

[74] Varshni, Y. P., Temperature dependence of the energy gap in semiconductors, *Physica* **1967,** *34*, 149–154.

[75] Yang, J.; Fainblat, R.; Kwon, S. G.; Muckel, F.; Yu, J. H.; Terlinden, H.; Kim, B. H.; Iavarone, D.; Choi, M. K.; Kim, I. Y.; Park, I.; Hong, H. K.; Lee, J.; Son, J. S.; Lee, Z.; Kang, K.; Hwang, S. J.; Bacher, G.; Hyeon, T., Route to the Smallest Doped Semiconductor: Mn^{2+}-Doped $(CdSe)_{13}$ Clusters, *J. Am. Chem. Soc.* **2015,** *137*, 12776–12779.

[76] Joo, J.; Son, J. S.; Kwon, S. G.; Yu, J. H.; Hyeon, T., Low-temperature solution-phase synthesis of quantum well structured CdSe nanoribbons, *J. Am. Chem. Soc.* **2006,** *128*, 5632–5633.

[77] Yu, J. H.; Liu, X.; Kweon, K. E.; Joo, J.; Park, J.; Ko, K. T.; Lee, D. W.; Shen, S.; Tivakornsasithorn, K.; Son, J. S.; Park, J. H.; Kim, Y. W.; Hwang, G. S.; Dobrowolska, M.; Furdyna, J. K.; Hyeon, T., Giant Zeeman splitting in nucleation-controlled doped $CdSe{:}Mn^{2+}$ quantum nanoribbons, *Nat. Mater.* **2010,** *9*, 47–53.

[78] Gary, D. C.; Flowers, S. E.; Kaminsky, W.; Petrone, A.; Li, X.; Cossairt, B. M., Single-Crystal and Electronic Structure of a 1.3 nm Indium Phosphide Nanocluster, *J. Am. Chem. Soc.* **2016,** *138*, 1510–1513.

[79] Xie, L.; Shen, Y.; Franke, D.; Sebastian, V.; Bawendi, M. G.; Jensen, K.

F., Characterization of Indium Phosphide Quantum Dot Growth Intermediates Using MALDI-TOF Mass Spectrometry, *J. Am. Chem. Soc.* **2016,** *138*, 13469–13472.

[80] Gary, D. C.; Petrone, A.; Li, X.; Cossairt, B. M., Investigating the role of amine in InP nanocrystal synthesis: destabilizing cluster intermediates by Z-type ligand displacement, *Chem. Commun.* **2016,** *53*, 161–164.

[81] Park, J.; An, K.; Hwang, Y.; Park, J. G.; Noh, H. J.; Kim, J. Y.; Park, J. H.; Hwang, N. M.; Hyeon, T., Ultra-large-scale syntheses of monodisperse nanocrystals, *Nat. Mater.* **2004,** *3*, 891–895.

[82] Kwon, S. G.; Piao, Y.; Park, J.; Angappane, S.; Jo, Y.; Hwang, N. M.; Park, J. G.; Hyeon, T., Kinetics of monodisperse iron oxide nanocrystal formation by "heating-up" process, *J. Am. Chem. Soc.* **2007,** *129*, 12571–12584.

[83] Jensen, K. M.; Andersen, H. L.; Tyrsted, C.; Bojesen, E. D.; Dippel, A. C.; Lock, N.; Billinge, S. J.; Iversen, B. B.; Christensen, M., Mechanisms for iron oxide formation under hydrothermal conditions: an in situ total scattering study, *ACS Nano* **2014,** *8*, 10704–10714.

[84] Oh, S. M.; Hendrickson, D. N.; Hassett, K. L.; Davis, R. E., Electron transfer in mixed-valence, oxo-centered, trinuclear iron acetate complexes: effect of statically disordered to dynamically disordered transformation in the solid state, *J. Am. Chem. Soc.* **1984,** *106*, 7984–7985.

[85] Powell, A. K.; Heath, S. L.; Gatteschi, D.; Pardi, L.; Sessoli, R.; Spina, G.; Del Giallo, F.; Pieralli, F., Synthesis, Structures, and Magnetic Properties

of Fe_2, Fe_{17}, and Fe_{19} Oxo-Bridged Iron Clusters: The Stabilization of High Ground State Spins by Cluster Aggregates, *J. Am. Chem. Soc.* **1995,** *117*, 2491–2502.

[86] Burger, J.; Klüfers, P., Stabilization of Iron Clusters by Polyolato Ligands and Calcium Ions: An Fe_{14} Oxocluster from Aqueous Alkaline Solution, *Angew. Chem. Int. Ed. Engl.* **1997,** *36*, 776–779.

[87] Micklitz, W.; Lippard, S. J., A novel hexairon(III) aggregate prepared from a basic iron(III) benzoate. Possible building blocks in ferritin core formation, *Inorg. Chem.* **1988,** *27*, 3067–3069.

[88] Taft, K. L.; Papaefthymiou, G. C.; Lippard, S. J., A mixed-valent polyiron oxo complex that models the biomineralization of the ferritin core, *Science* **1993,** *259*, 1302–1305.

[89] Chakraborty, I.; Baran, P.; Sanakis, Y.; Simopoulos, A.; Fachini, E.; Raptis, R. G., A mixed-valence octanuclear iron-oxo pyrazolate: assessment of electronic delocalization by structural and spectroscopic analysis, *Inorg. Chem.* **2008,** *47*, 11734–11737.

[90] Bagai, R.; Daniels, M. R.; Abboud, K. A.; Christou, G., Unusual structural types in polynuclear iron chemistry from the use of N,N,N',N'-tetrakis(2-hydroxyethyl)ethylenediamine ($edteH_4$): Fe_5, Fe_6, and Fe_{12} clusters, *Inorg. Chem.* **2008,** *47*, 3318–3327.

[91] Boudalis, A. K.; Tangoulis, V.; Raptopoulou, C. P.; Terzis, A.; Tuchagues, J.-P.; Perlepes, S. P., A new example of a tetranuclear iron(III) cluster

containing the $[Fe_4O_2]^{8+}$ core: preparation, X-ray crystal structure, magnetochemistry and Mössbauer study of $[Fe_4O_2(O_2CMe)_6(N_3)_2(phen)_2]$, *Inorganica Chim. Acta* **2004,** *357*, 1345–1354.

[92] Taft, K. L.; Lippard, S. J., Synthesis and structure of $[Fe(OMe)_2(O_2CCH_2Cl)]_{10}$: a molecular ferric wheel, *J. Am. Chem. Soc.* **1990,** *112*, 9629–9630.

[93] Gatteschi, D.; Sessoli, R.; Villain, J., *Molecular Nanomagnets*. Oxford University Press: Oxford, UK, **2006**.

[94] Sadeghi, O.; Zakharov, L. N.; Nyman, M., Crystal growth. Aqueous formation and manipulation of the iron-oxo Keggin ion, *Science* **2015,** *347*, 1359–1362.

[95] Liu, T.; Diemann, E.; Li, H.; Dress, A. W.; Muller, A., Self-assembly in aqueous solution of wheel-shaped Mo_{154} oxide clusters into vesicles, *Nature* **2003,** *426*, 59-62.

[96] Long, D. L.; Tsunashima, R.; Cronin, L., Polyoxometalates: building blocks for functional nanoscale systems, *Angew. Chem. Int. Ed. Engl.* **2010,** *49*, 1736–1758.

[97] Day, V. W.; Klemperer, W. G., Metal oxide chemistry in solution: the early transition metal polyoxoanions, *Science* **1985,** *228*, 533–541.

[98] Anderson, J. S., Constitution of the Poly-acids, *Nature* **1937,** *140*, 850.

[99] Keggin, J. F., Structure of the Molecule of 12-Phosphotungstic Acid, *Nature* **1933,** *131*, 908–909.

[100] Dawson, B., The structure of the 9(18)-heteropoly anion in potassium 9(18)-tungstophosphate, $K_6(P_2W_{18}O_{62}).14H_2O$, *Acta Crystallogr.* **1953,** *6*, 113–126.

[101] Alizadeh, M. H.; Harmalker, S. P.; Jeannin, Y.; Martin-Frere, J.; Pope, M. T., A heteropolyanion with fivefold molecular symmetry that contains a nonlabile encapsulated sodium ion. The structure and chemistry of $[NaP_5W_{30}O_{110}]_{14}$, *J. Am. Chem. Soc.* **1985,** *107*, 2662–2669.

[102] Panasci, A. F.; Ohlin, C. A.; Harley, S. J.; Casey, W. H., Rates of water exchange on the $[Fe_4(OH)_2(hpdta)_2(H_2O)_4]^0$ molecule and its implications for geochemistry, *Inorg. Chem.* **2012,** *51*, 6731–6738.

[103] Zhu, M.; Frandsen, C.; Wallace, A. F.; Legg, B.; Khalid, S.; Zhang, H.; Mørup, S.; Banfield, J. F.; Waychunas, G. A., Precipitation pathways for ferrihydrite formation in acidic solutions, *Geochim. Cosmochim. Acta* **2016,** *172*, 247–264.

[104] Meunier, B., *Metal-Oxo and Metal-Peroxo Species in Catalytic Oxidations*. Springer-Verlag Berlin Heidelberg: Berlin, **2000**.

[105] Banfield, J. F.; Welch, S. A.; Zhang, H.; Ebert, T. T.; Penn, R. L., Aggregation-based crystal growth and microstructure development in natural iron oxyhydroxide biomineralization products, *Science* **2000,** *289*, 751–754.

[106] Lopez, X.; Carbo, J. J.; Bo, C.; Poblet, J. M., Structure, properties and reactivity of polyoxometalates: a theoretical perspective, *Chem. Soc. Rev.* **2012,** *41*, 7537–7571.

Chapter 2. Molecular-Level Understanding of Continuous Growth from Iron-Oxo Clusters to Iron Oxide Nanoparticles

** Reprinted with permission from *J. Am. Chem. Soc.* **2019**, *141*, 7037–7045.

2.1 Introduction

The formation mechanism of inorganic colloidal nanoparticles has been generally understood by classical colloid chemistry based on nucleation and growth processes. The thermodynamic aspects of nucleation, the generation of small solid-phase crystals from the assembly of minimal binding units (monomers)[1-3], are important for regulating the entire nanoparticle formation process. The free energy of nuclei can be estimated as the sum of surface and bulk free energies.[3] Owing to the strong dependency of surface energy on size, a critical size exists below which dissolution of thermodynamically unstable particulates occurs. To overcome the thermodynamic energy barrier to nucleation, the monomer concentration needs to exceed the supersaturation level, whereby a significant number of monomers form stable nuclei. During homogeneous nucleation process to synthesize nanoparticles, supersaturation of monomers can be induced by various methods including rapid injection of precursors into a hot surfactant solution, and gradual ‘heating-up’ of the reaction mixture, and conversion of the precursors into monomers with reduced solubility.[4-9] Recent studies reveal that monomers with different chemical states, such as small molecular species and clusters containing a few metal atoms or ions,[10-14] participate in the formation of colloidal nanoparticles. In the subsequent growth regime, nuclei grow into nanoparticles via monomer attachment or coalescence events between the particles.[12,15-17] The surface energy of the growing nanoparticles controls not only the growth rate, but also their resulting sizes and morphologies.[18]

Various experimental approaches have been employed to understand the formation mechanisms of nanoparticles.[5,6,19-27] These are mostly focused on semiconductor nanoparticles as can be easily tracked with their size-specific optical properties. The formation of the nanoparticles is generally controlled by dynamic fluctuations between the growing nanoparticles and surface ligands, which bind to both molecular precursors and monomers.[6,28-31] The strength of the binding moieties affects important stages during the growth of nanoparticles. For example, weakly binding moieties, such as CdSe-amine bonding, are susceptible to fast decomposition of the molecular precursors to generate a burst of nuclei.[28-31] In the opposite case, in the presence of strongly binding moieties, such as CdSe-phosphonate bonding, the rate of nucleation is reduced by delaying the precursor decomposition.[6] In addition, the reactivity of the chalcogenide source and the reaction temperature concurrently influence the regulation of the growth rate. Important roles of intermediates during the growth from precursors to nanoparticles have also been observed in several systems of metal chalcogenide nanoparticles.[32-34]

The formation mechanism of metal oxide nanoparticles can be inherently different from that of metal chalcogenides due to several unique chemical aspects of their synthesis process. During a typical synthesis of metal oxide nanoparticles, molecular precursors include metal-carboxylate moieties and the carboxylate group stays on the surface of the nanoparticles throughout the process. The carboxylate binding moieties include oxygen atoms and normally acts as an oxygen source during the formation of the metal oxide nanoparticles. Based on the hard soft acid base theory, carboxylates are hard base. As a result, they can strongly coordinate hard metal ions, such as Fe^{3+}, on the surface of the metal oxide nanoparticles.[35] However, when the carboxylate ligands on the surface of precursors or nanoparticles are eliminated by thermal decomposition or chemical reaction, the reactive hydroxyl groups or radicals are temporarily retained on the metal ions. Chemical reactions between them can induce direct interactions between nanoparticles and frequently promote the growth of metal oxide nanoparticles.[5,36-39] Such unique thermodynamic characteristics of carboxylate moieties and their mechanistic behaviors imply that they may strongly control the formation of metal oxide nanoparticles from the initial transition of molecular precursors to small particulates and to the growth into large nanoparticles. In this case, the size of the particles in the range below the critical nucleus size where intermediate species are thermodynamically unstable, typically observed in the formation of other types of nanoparticles, can become narrow, or even absent.

Herein, we used various characterization methods including matrix-assisted laser desorption ionization time-of-flight mass spectrometry (MALDI-TOF MS), nuclear magnetic resonance (NMR) spectroscopy, transmission electron microscopy (TEM), and *in situ* X-ray scattering to study the entire formation process of iron oxide nanoparticles. We confirmed that iron-oleate complexes, the representative precursors of iron oxide nanoparticles,[40] have a cluster structure containing tri-iron-oxo-carboxylate (Figure 2.1a,b). More importantly, we reveal that the entire process is continuous without any discrete nucleation event (Figure 2.1 c,d), while the growth from tri-iron-oxo clusters to larger-sized iron-oxo clusters and eventually to iron oxide nanoparticles is driven by esterification of ligand moieties. Our findings provide new insights regarding the importance of ligand binding moieties and their reactions in metal oxide nanoparticle formation.

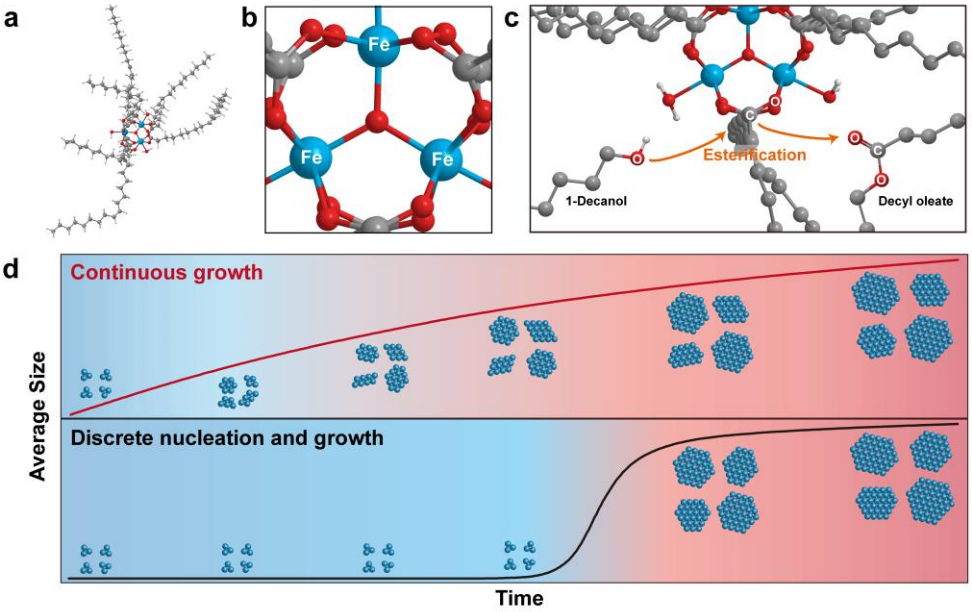

Figure 2.1 Structure of iron-oleate complex and continuous growth of iron-oxo clusters. (a) Computed trinuclear-oxo-carboxylate structure of iron-oleate complex ($[Fe_3O(C_{18}H_{33}O_2)_6]^+$). (b) Core structure of iron-oleate complex. (c) Proposed reaction mechanism of continuous growth induced by esterification. (d) Schematic of continuous growth proposed in this paper and that of discrete nucleation and growth. Compared to discrete nucleation and growth, continuous growth does not show distinct nucleation step, but shows gradual growth.

2.2 Experimental

Chemicals. Iron chloride hexahydrate (98%), 1-decanol, 3-aminoquinone, insulin, and cytochrome C were purchased from Sigma-Aldrich. Sodium oleate (95%) was purchased from TCI. Ethanol, *n*-hexane, chloroform ($CHCl_3$), and *n*-pentane were purchased from Samchum Chem. Peptide Y5R was purchased from Peptron (Daejeon, Korea).

Synthesis of iron-oxo-oleate complex. Iron-oxo-oleate complex was synthesized based on the previously reported method.[40] Notably, the reaction for the formation of the iron-oxo-oleate complex is not air sensitive (Figure 2.2). Iron chloride hexahydrate (10.8 g, 40 mmol) and sodium oleate (36.5 g, 120 mmol) were stirred in a mixture of 140 mL hexane, 80 mL ethanol, and 60 mL deionized water for 4 h at 50 °C. The ratio of solvents in a reaction mixture is optimized for clear phase separation.[41] After the completion of the reaction, the hexane phase was separated using a separation funnel and washed with deionized water three times. Finally, hexane was evaporated under vacuum in overnight.

Synthesis of iron-oxo clusters. Iron-oxo clusters were synthesized by esterification between the iron-oxo-oleate complex and a primary alcohol.

First, iron-oxo-oleate complex (1.9 g, 1 mmol) and 1-decanol (10.0 g) were mixed and degassed at room temperature. The mixture was heated to an aging temperature (100 °C to 200 °C) at a heating rate of 3.3 °C/min, and then held at that temperature for 24 h under an inert atmosphere. After the reaction was complete, the solution was rapidly cooled and centrifuged with ethanol to decant unreacted reactants and by-products. The final product was dispersed in non-polar solvents such as hexane or chloroform.

Mass characterization. Mass characterization was performed using a home-built MALDI-TOF instrument. It was calibrated using calibrants, 3-aminoquinone (M_w = 144.17 Da), Y5R peptide (M_w = 990.08 Da), insulin (M_w = 5735.6087 Da), and cytochrome C (M_w = 12361.97 Da), and the matrix 9-nitroanthracene (0.1 M in chloroform). The analyte and matrix were properly mixed in chloroform to obtain optimized mass profiles. The mixture was dried on a sample plate with vacuum evaporation, and the dried samples were desorbed and ionized by a 337-nm nitrogen laser (MNL100, Lasertechnik Berlin, Germany) with an accelerating voltage of 20.0 kV and laser power of 5.0~8.5 μJ. Each spectrum was acquired by focusing 20 laser shots on each spot and 10 different spots were averaged.

Optical characterization. Fourier transform infrared (FT-IR) spectra of the samples were acquired using a Bruker VERTEX 70V spectrometer. The

Raman spectra were recorded using a LabRam HV Evolution system equipped with a 514.5-nm Ar-ion laser. The optical absorption spectra were obtained using a CARY 5000E UV-VIS-NIR spectrophotometer.

Solution NMR characterization. Nuclear magnetic resonance (NMR) spectra were recorded on a Bruker Avance III Spectrometer operating at ^{1}H and ^{13}C frequencies of 500.000 MHz and 125.721 MHz. The sample temperature was set as 298.15 K. Fast cooled *ex situ* aliquots were measured without any treatment to avoid losing original information. All samples were dissolved in deuterated chloroform.

TEM characterization. Graphene grown on a Cu foil by CVD (chemical vapour deposition) was placed on a Quanntifoil Au holey carbon grid with a hole size of 1.2 μm. The Cu substrate was etched with 0.1 M aqueous ammonium persulfate solution. The graphene TEM grids were dried at 80 °C overnight and then the cluster solutions were dropped onto the grids. Aberration-corrected transmission electron microscopy (TEM) images were obtained with a TITAN G2 at an acceleration voltage of 80 kV.

***In situ* X-ray scattering measurement & processing.** Synchrotron *in situ* SAXS/WAXS measurements were conducted at the PLS-II 9A U-SAXS beamline of Pohang Accelerator Laboratory (PAL), Korea. The X-rays from the in-vacuum undulator (IVU) were monochromated using Si(111) double crystals and focused at the detector position using K-B-type mirrors (the beam size was 30 μm × 290 μm (V × H)). The scattering patterns were recorded with a 2D CCD detector (Rayonix SX165), and the X-ray irradiation time was 5 s depending on the saturation level of the detector.

For SAXS, the scattering angles were calibrated by a pre-calibrated TiSBA (1st peak at 0.06521 $Å^{-1}$). The sample-to-detector distance was about 2.0 m. For WAXS, the scattering angles were calibrated by a pre-calibrated sucrose (Monoclinic, P21, a = 10.8631 Å, b = 8.7044 Å, c = 7.7624 Å, β = 102.938°),[42] and the sample-to-detector distance was about 510 mm.

For the *in situ* experiment, iron-oxo-oleate and primary alcohol were mixed in the same ratio as that in the iron-oxo cluster synthesis and degassed in a vial. The prepared solution was injected into a 1.5-mm quartz capillary tube placed on a heating block. Each experiment was measured at different scattering angles (SAXS or WAXS), aging temperatures, and alcohol chain lengths. The scattering intensities acquired at the SAXS region ($q = 0.015 \sim 0.4$ $Å^{-1}$) were subtracted by background intensity of excess solvents (1-decanol or diphenyl ether). AUTORG macro was applied to determine the radius of gyration for each subtracted scattering intensity.[43] The scattering intensity measured within the WAXS region ($q = 2.2 \sim 2.8\,Å^{-1}$) can be expressed as the summation of 3rd degree polynomial and the Gaussian distribution.[44] Here, 3rd degree polynomial refers to the continuously changing background intensity of the solvents and capillary tube. The intensity of the Gaussian distribution originates from the iron oxide nanoparticles.

$$I(q) = aq^3 + bq^2 + cq + d + I_0 \exp(-(q - q_0)^2 / 2\sigma^2)$$

Computational details. The first-principles calculations based on the spin-polarized density functional theory[45] were performed with the Vienna Ab-initio Simulation Package (VASP) using a projector-augmented-wave (PAW) method.[46] The exchange correlation energy functional was employed with the generalized gradient approximation (GGA) in the Perdew–Burke–Ernzerhof scheme,[47] and the kinetic energy cutoff was set as 400 eV. A geometrical optimization of the iron-oxo complexes was carried out until the Hellmann–Feynman force acting on each atom was less than 0.01 eV/Å. To remove spurious interactions between periodic images due to periodic calculations by the long-range Coulomb interaction, a vacuum distance of 15 Å was considered between the molecules.

The formation energy of the iron-oxo complexes was calculated by the following definition:

$(E_{\text{Fe-oxo}} - N_{\text{Fe}} \cdot E_{\text{Fe}}^{\text{bulk}} - N_{\text{C}} \cdot E_{\text{C}}^{\text{graphene}} - N_{\text{O}} \cdot E_{\text{O}}^{\text{O}_2} - N_{\text{H}} \cdot E_{\text{H}}^{\text{H}_2})$, where $E_{\text{Fe-oxo}}$, $E_{\text{Fe}}^{\text{bulk}}$, $E_{\text{C}}^{\text{graphene}}$, $E_{\text{O}}^{\text{O}_2}$, and $E_{\text{H}}^{\text{H}_2}$ denote the total energy of the iron-oxo clusters, the total energy per Fe in a bcc Fe, the total energy per C in a graphene, the total energy per O in an O_2 molecule, and the total energy per H in a H_2 molecule, respectively. N_{Fe}, N_{C}, N_{O}, and N_{H} denote the number of iron, carbon, oxygen, and hydrogen atoms for a given cluster, respectively.

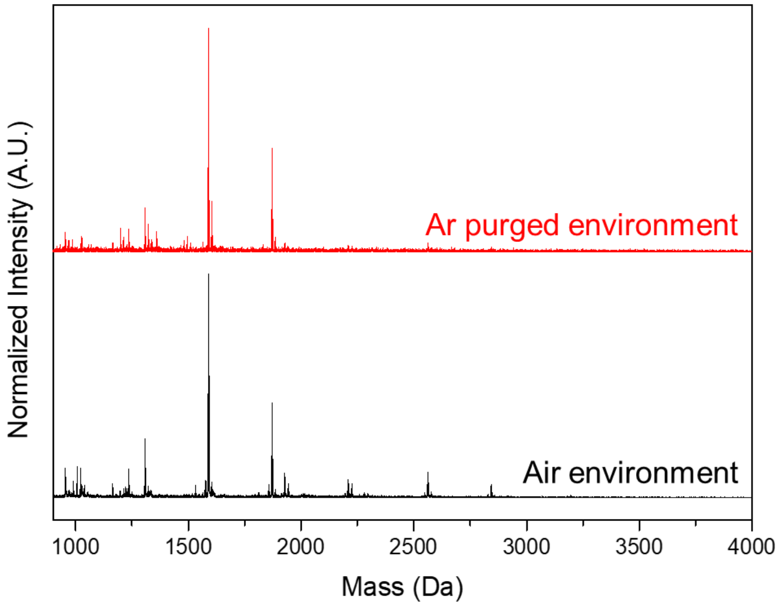

Figure 2.2 MALDI-TOF MS of iron-oxo-oleate synthesized in air (black) and inert (red) environment.

2.3 Results and discussions

2.3.1 Characterization of Iron-Oleate Complex

We study the complete growth process of the formation of iron oxide nanoparticles from iron-oleate precursors. The oleate ligands strongly bind to the metal center of the precursors and passivate the surface of the growing nanoparticles. Since the energetics of precursors determines the chemical transformation in the early stage, identification of precursor structure is a prerequisite for understanding the initiation of the reaction. We first characterized the iron-oleate complex by MALDI-TOF MS, Fourier transform infrared (FT-IR), and near-infrared spectroscopies.

MALDI-TOF MS is a powerful tool to characterize the exact molecular weight of metal-ligand complexes with minimal molecular fragmentation. The mass spectrum of the iron-oleate complex, which was synthesized from the reaction of iron chloride hexahydrate and sodium oleate, shows two main peaks (m/z = 1872 and 1591) in the high-mass region as shown in Figure 2.3a. Isotope calculation of the main peak at m/z = 1872 confirms that the chemical structure of the iron-oleate complex is $[Fe_3O(C_{17}H_{33}COO)_6]^+$, which we refer to as tri-iron-oxo-carboxylate complex (Figure 2.3b). The six coordinating oleate groups are further verified by comparing the molecular weight of the iron-oleate (m/z = 1872) with those of iron-stearate (m/z = 1884) and iron-linoleate (m/z = 1860) complexes, which show differences of +12 and –12

Da, respectively. Given that stearate (MW = 283.27 Da), oleate (MW = 281.25 Da), and linoleate (MW = 279.23 Da) have similar structures with a molecular weight difference of 2 Da of the two hydrogen atoms consecutively, the measured difference of 12 Da indicates that all the complexes contain six ligands (Figure 2.3c). Another main peak at m/z = 1591, with a difference corresponding to the mass of oleate ions, originated from the fragments of the iron-oleate complex during the measurement. TOF-TOF analysis further supports that the parent iron-oleate peak (m/z = 1872) can be broken into another main peak (m/z = 1591) (Figure 2.3d). It is noteworthy that a coordinated structure with six long-chain carboxylates are consistently observed regardless of the chemical structures of the ligands.

The presence of tri-iron-oxygen center in the iron-oleate complex is supported by various spectroscopic measurements, which have been commonly used to characterize various metal carboxylates containing metal-oxo centers.[48-58] The triangular structure strongly absorbs near-infrared light at 935 nm (Figure 2.3e). This absorption band is assigned to the $^6A_{1g}$ to $^4T_{1g}$ electron transition in the pseudo-octahedral Fe^{3+} ion.[51,52] A similar structure having a shorter carboxylate chain presents a comparable absorbance at 965 nm. On the contrary, iron chloride, which does not contain a metal-oxygen center, barely absorbs near-infrared light (800–1300 nm). The vibrational mode of Fe_3O is observed at approximately 600 cm^{-1} in the IR spectrum (Figure 2.4). The wavenumber for this absorption is consistent with the previous report on trinuclear-oxo-carboxylate complexes.[53] The binding nature of carboxylate ligands within the complex can be verified by comparing the wavenumber difference between the symmetric and asymmetric vibrations of the carboxyl group.[55] The wavenumber difference of 160 cm^{-1} indicates that the oleate ligand is bound to iron in the bridging mode. As a control experiment, the vibration peaks of sodium oleate are confirmed as 1560 cm^{-1} and 1447 cm^{-1}, which represent the ionic binding mode. The comparison of the FT-IR spectra of iron-oleate complex and sodium oleate reveals that the peaks at 1520 cm^{-1} and 1420 cm^{-1} (shoulder) originate from the asymmetric vibration of non-bridging ionic oleate that binds to the iron-oxo-oleate complex (Figure 2.5).[56] The direct bonding states of iron ions and oleate ligand induce distinct changes in the NMR spectrum (Figure 2.6 and 2.7). Carbons and hydrogens, which have 2-bond distance from the iron ions, should not appear in ordinary NMR spectra because paramagnetic iron ions can affect the magnetic resonance of nearby atoms.[57,58] In the ^1H NMR spectrum, hydrogens, which are bonded to the α-carbon of the oleate group, are expected to shift downfield. In the ^{13}C NMR spectrum, the carboxyl carbon is expected to shift downfield, while the α-carbon is shifted upfield.

In the structure of iron-oleate complex, three iron ions are bound to the central μ_3-oxygen, and six carboxylates bridge the iron ions as illustrated in Figure 2.1a,b. The tri-iron-oxo-carboxylate complex, $[Fe_3O(RCOO)_6]^+$ has been reported as a stable triangular structure.[27,49-52,56,57] Overall chemical composition of iron-oxo-oleate is proposed as $[Fe_3O(C_{18}H_{33}O_2)_6]^+(C_{18}H_{33}O_2)^-(C_{18}H_{33}O_2H)_2(H_2O)_3$ based on elemental analysis (Table 2.2).

Consistent occurrence of iron-oxo-oleate is also observed during the formation of iron oxide nanoparticles from different iron precursors including iron chloride ($FeCl_3$), iron acetylacetonate ($Fe(acac)_3$) and iron nitrate ($Fe(NO_3)_3$). When high enough temperature is applied to activate the precursor salts to be decomposed, the peak patterns from the two different mixtures ($Fe(acac)_3$ + oleic acid and $Fe(NO_3)_3$ + oleic acid), shown in Figure 2.3f, are nearly identical to that of iron-oleate complex synthesized using $FeCl_3$. The common appearance of trinuclear-oxo-oleate in several synthetic pathways confirms the structural stability and similarity of the events at the early stage of the synthesis. We could elucidate the structure of iron-oleate precursors, which are generally used for the synthesis of iron oxide nanoparticles. Our findings demonstrate that the iron-oleate precursor is not a complex containing a single metal atom center, but a cluster with three irons bound to μ_3-oxygen.

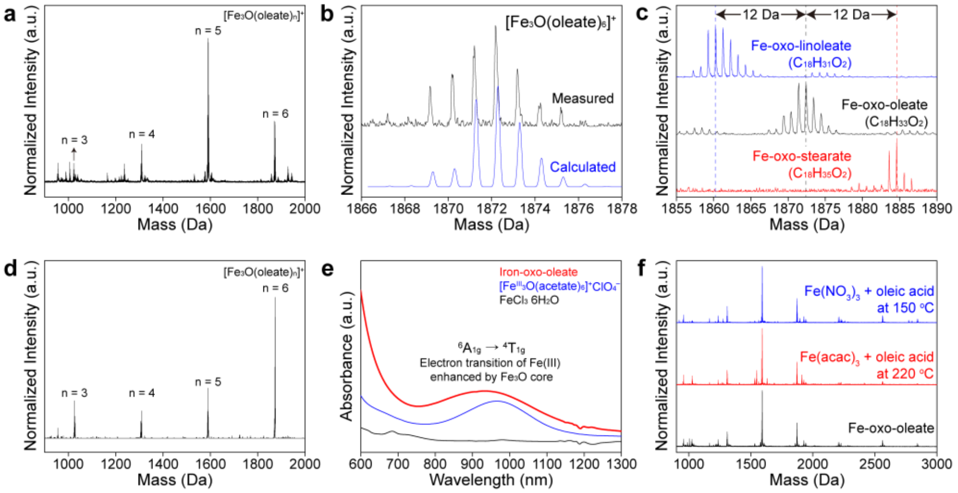

Figure 2.3 Characterization of iron-oxo-oleate complex. (a) MALDI-TOF mass spectra of iron-oxo-oleate complex. Main peaks iron-oxo-oleate are assigned in the mass spectra. (b) Isotope calculation of the main peak at m/z = 1872. (c) MALDI-TOF mass spectra of iron-oxo-carboxylates having different numbers of double bonds in the ligand. (d) TOF-TOF mass spectrum of $[Fe_3O(oleate)_6]^+$ (m/z = 1872). (e) Near-infrared absorption spectra of iron complexes. Absorption wavelength and extinction molar coefficient are presented in Table 2.1. (f) Emergence of iron-oxo-oleate complex in mass spectra starting from different iron salts.

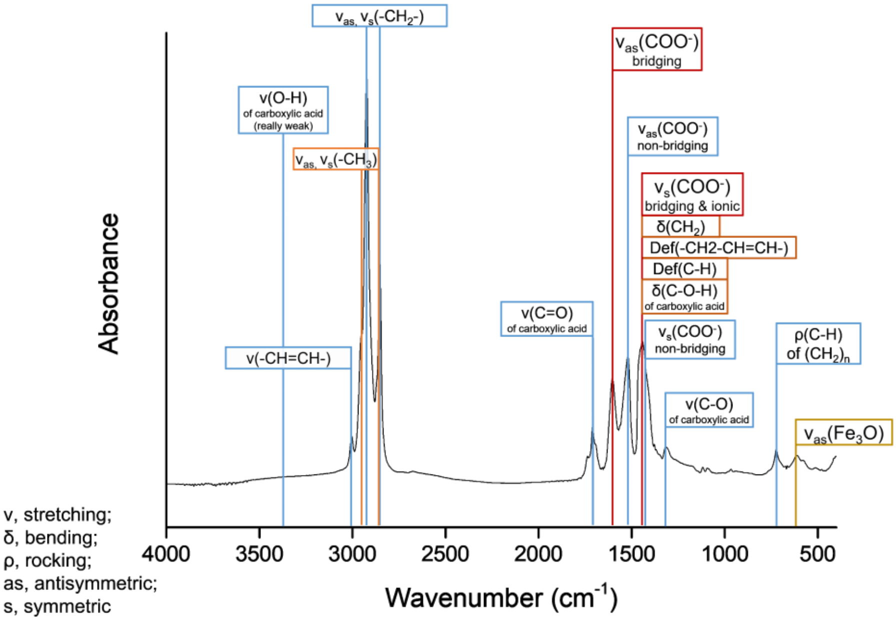

Figure 2.4 Assignment of peaks in infrared spectrum of iron-oxo-oleate.

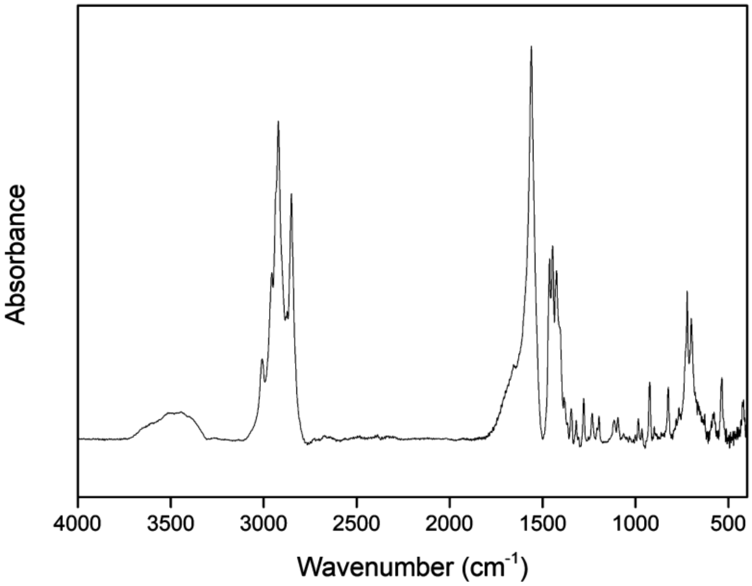

Figure 2.5 Infrared spectrum of sodium oleate.

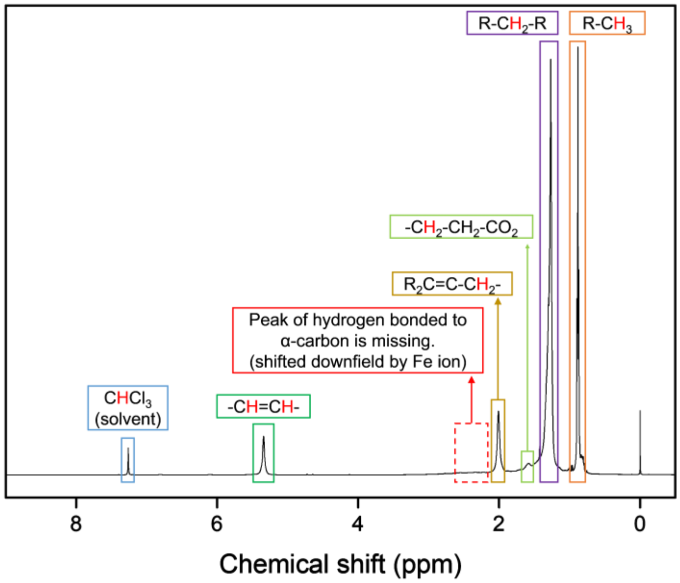

Figure 2.6 ^1H NMR spectrum of iron-oxo-oleate complex.

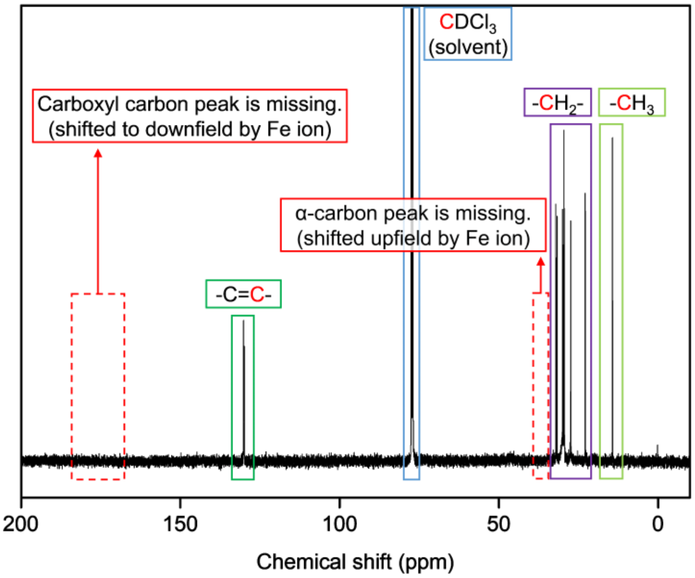

Figure 2.7 ^{13}C NMR spectrum of iron-oxo-oleate complex.

Table 2.1 Absorption wavelength and molar absorption coefficient of iron complexes.

	Iron-oxo-oleate	**$[Fe^{III}_3O(acetate)_6]^+ClO_4^-$**	**$FeCl_3 \cdot 6H_2O$**
Absorption wavelength [nm]	935	965	980
Molar absorption coefficient [L mol^{-1} cm^{-1}]	12.8	22.8	0.132

Table 2.2 Elemental composition measured by ICP-MS and elemental analysis. Calculated composition is obtained from the formula $[Fe_3O(C_{18}H_{33}O_2)_6]^+(C_{18}H_{33}O_2)^-(C_{18}H_{33}O_2H)_2(H_2O)_3$.

Elements	Experimental	Calculated
Fe	5.96%	6.04%
C	70.50%	70.18%
H	11.08%	11.09%
O	12.46%	12.69%

2.3.2 Continuous Growth Mechanism of Iron Oxide Nanoparticles

We studied the formation process of iron oxide nanoparticles from the iron-oxo-oleate complexes by using NMR spectroscopy, MALDI-TOF MS, and aberration-corrected TEM. Briefly, the reaction rate is controlled to be slow by keeping the temperature below 200 °C to allow a time-series analysis of the ongoing reaction and avoid complications that might occur at high temperatures (Figure 2.8).[59] 1-Decanol is used for multiple purposes including a solvent and a reaction promotor.[39]

When the iron-oxo-oleate complex is reacted with an excess amount of 1-decanol at 100 °C, the solution gradually turned to dark brown from reddish-brown. The products of this reaction are tracked by NMR spectra to investigate the reaction mechanism. Two strong peaks ($\delta_H = 4.06, 2.29$) that correspond to ester group are observed in the NMR spectra (Figure 2.9a). The ester peaks presumably originate from decyl oleate, which is produced from the esterification of 1-decanol and the oleate group in the iron-oxo-oleate complex. The presence of decyl oleate from the beginning of the reaction indicates that the formation of nanoparticles is initiated by the esterification reaction of the ligands strongly binding to the tri-iron-μ_3-oxygen core. NMR and LC-MS analyses of the byproducts from the reaction mixture also confirm that decyl oleate is produced from the esterification reaction (Figure 2.10 and 2.11). The extent of reaction is quantitatively analyzed by comparing the integration of NMR peaks for hydrogen adjacent to the ester group using hydrogen bound to the C=C double bond of the oleate group as a reference, which remains constant throughout the reaction (Figure 2.9a–c). The continuous increase in peak intensity of the hydrogen adjacent to the ester indicates prolonged proceeding of the esterification. In addition, shorter ligands are introduced to investigate the steric effect of ligands of iron-oxo-clusters on the rate of esterification (Figure 2.12). The esterification reaction with shorter ligands (C_8) is expedited by 1.15 times than that with longer ligands (C_{18}), indicating that the reaction between the precursor and alcohol can be controlled by regulating the steric hindrance of ligands. The esterification reaction is important at the initial phase of the nanoparticle formation as it can result in the activation of a metal center by removing the carboxylate ligands and generating hydroxyl groups.[23,60,61]

The reaction mechanism can be more specifically investigated by using MALDI-TOF MS, which is suitable for tracing the size distribution of nanomaterials of < 5 nm (Figure 2.9d–f, 2.13).[11] At the very early stage, when carboxylate ligands of iron-oxo-oleate react with the alcohol, various populations of iron-oxygen species containing different numbers of metal centers emerge in the mass spectra. Particularly, the evolution of Fe_2, Fe_4, Fe_5, and Fe_6 species is noticed after the onset of esterification (Figure 2.13a,b, and Table 2.3). The formation of Fe_2, Fe_4, and Fe_5 implies that a portion of the trinuclear-oxo cluster is decomposed into smaller activated units after esterification, which can, in turn, form larger units by attaching to undecomposed trinuclear-oxo clusters. To support the suggested growth pathway, the stability of the growing iron-oxo clusters are examined by density functional theory (DFT) calculations. In DFT calculations, the metal-oxo core and carboxylate binding groups of the surface ligands are only introduced as they are the major contributors to the energy of the iron-oxo-complexes. The initial structures of different iron-oxo-complexes with an increasing number of metal ions, i.e., Fe_3O, Fe_4O_2, Fe_5O_2, and, Fe_6O_3, are chosen based on our MS analysis and geometrically optimized to calculate the energy of complex formation and ligand binding (Figure 2.13b and 2.14). The formation energy of iron-oxo-complexes with surface ligands presents a decreasing tendency as the size of the complexes increases (Figure 2.13d), otherwise shows an increasing tendency without surface ligands (Figure 2.13c). In addition, the calculated binding energy of the carboxylate ligands on the iron-oxo core is distinctly larger than that of other types of surface ligands (Figure 2.13e).[23,28-30,62,63] These results show that the strongly binding ligands reduce the formation energy of intermediate complexes, driving the pathway with a continuously increasing number of metal ions (Figure 2.1d).[39]

Subsequently, through the aging process, these small iron-oxygen species gradually grow to large-sized clusters and eventually into nanoparticles typically observed in the synthesis of iron oxide nanoparticles, as presented in Figure 2.9e. The continuous removal of oleate ligands by esterification

(Figure 2.9b) occurs simultaneously with continuous growth of nanoparticle from the starting tri-iron-μ_3-oxygen clusters. Iron-oxygen core can be gradually grown into larger species by condensation between hydroxyl groups of the iron-oxo clusters, which is formed after esterification of oleate ligands. Since the rate of the condensation of hydroxyl groups on the transition metal cores is fast enough,[64] the rate of continuous growth of iron oxide nanoparticles highly depends on the rate of esterification. The temperature-dependent ^{1}H NMR measurement shows that the rate of esterification is positively proportional to the temperature (Figure 2.9c). The temporal profile of the most dominant mass also reveals a similar pattern to that of the temperature-dependent rate of esterification (Figure 2.9f). It is noteworthy that continuous with the absence of distinct nucleation, is universally observed over a broad temperature range from 100 °C to 140 °C (Figure 2.15, 2.16, and 2.17).

Continuous growth can also be examined by TEM characterization of sample aliquots taken during aging at 140 °C (Figure 2.18a–c). Samples for TEM analysis are prepared on graphene substrates. Because of its high electrical and thermal conductivity, graphene substrate can minimize the electron beam effect during the TEM characterization.[65,66] Additionally, graphene minimizes the scattering of incoming electron beam, thereby improving the contrast of small clusters.[16,67] In the early stage of the reaction (0 h), clusters with 3 to 10 atoms are observed (Figure 2.18a and 2.19), and the number of atoms per cluster increases with reaction time (Figure 2.18b and 2.20). The clusters grow into small-sized nanoparticles (1.5–2.5 nm) after aging for 24 hours (Figure 2.18c and 2.21). The TEM images of the iron-oxo clusters and iron oxide nanoparticles are consistent with the mass spectra, and both characterization datasets reveal continuous growth from molecular clusters to solid oxide nanoparticles without distinct nucleation.

The continuous growth mechanism is confirmed in the ensemble level by *in situ* X-ray scattering measured at different angles. *In situ* X-ray scattering technique has been frequently used for real-time observation of nucleation and growth processes.[21,45,68-70] At a small-angle regime, iron-containing compounds are the dominant scattering species, which have a high relative scattering length density with respect to background solvent. Guinier plot is applied to derive the radius of gyration of iron-containing species, as it can suggest dynamic changes in ensemble in the system. A gradual increase in radius of gyration is observed, consistent with the observations from other measurements, indicating the continuous growth of iron-oxo clusters induced by esterification (Figure 2.22a,b). Moreover, the radius of gyrations acquired from Guinier plots show temperature dependency, as confirmed from NMR spectroscopy and MALDI-TOF MS (Figure 2.22c). X-ray scattering at the wide-angle regime includes crystallographic information of emerging iron oxide nanoparticles. The growth of clusters into nanoparticles is verified by the gradual appearance of the (311) lattice plane of iron oxide nanoparticles

(Figure 2.22d,e). Sharp scattering peaks of the nanoparticles synthesized at high temperatures show that the crystal domain size of the product increases with increasing reaction temperature (Figure 2.22f).

NMR spectroscopy, mass spectrometry, electron microscopy, and X-ray scattering techniques provide consistent results supporting continuous growth from trinuclear-oxo clusters into larger iron-oxo clusters followed by the formation of iron oxide nanoparticles. Based on these characterization results, we suggest a new growth mechanism, a continuous growth model, which is induced by the controlled organic reaction between the strong binding ligands on the clusters and added alcohol in the solution. The continuous growth dominates the overall reaction process from trinuclear-oxo clusters to large-sized iron-oxo clusters, and then to iron oxide nanoparticles (Figure 2.1). This controlled reaction pathway can be understood in the similar context of the non-hydrolytic sol-gel chemistry. At first, the controlled alcoholysis of trinuclear-oxo clusters forms hydroxyl groups on the trinuclear-oxo clusters. The trinuclear-oxo clusters containing reactive hydroxyl groups are condensated into intermediate iron-oxygen species, which have distinct numbers of iron (i.e., Fe_2, Fe_4, Fe_5, and Fe_6). These intermediate species grow into continuously profiled iron-oxo clusters from continuous supply of reactive clusters. Eventually, the nanoparticles gradually appear from the continuously growing iron-oxo clusters. This mechanism implies that the nucleation step is not distinct during the formation of the iron oxide nanoparticles studied in this report, whereas it is normally observed in the formation of many other types of nanoparticles as a prior stage to the growth regime. We believe that the absence of a distinct nucleation stage can be justified by the thermodynamic stability of the intermediate clusters regardless of their sizes due to the strong binding carboxylate groups, and the controlled activation of the stabilized iron-oxo clusters.[39]

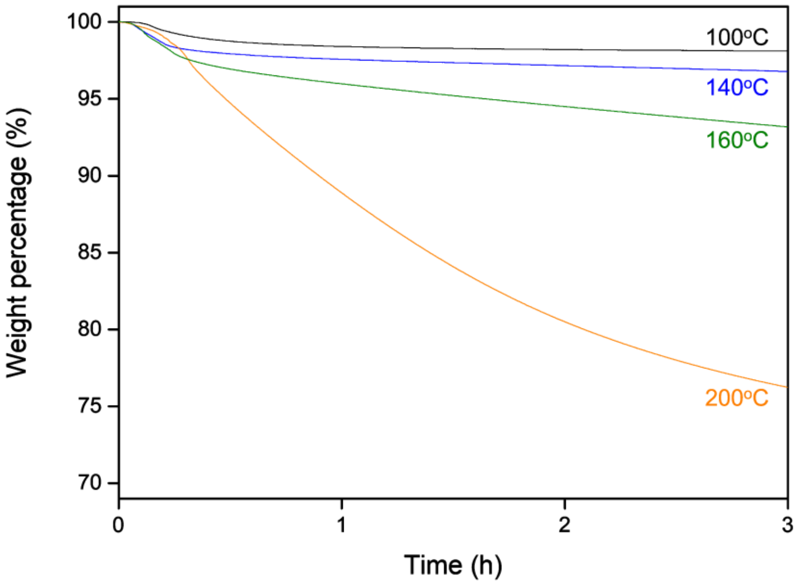

Figure 2.8 Thermogravimetric analysis (TGA) curve of iron-oxo-oleate measured at different temperatures. TGA confirms that the thermal decomposition of trinuclear-oxo cluster is suppressed below 200 °C.

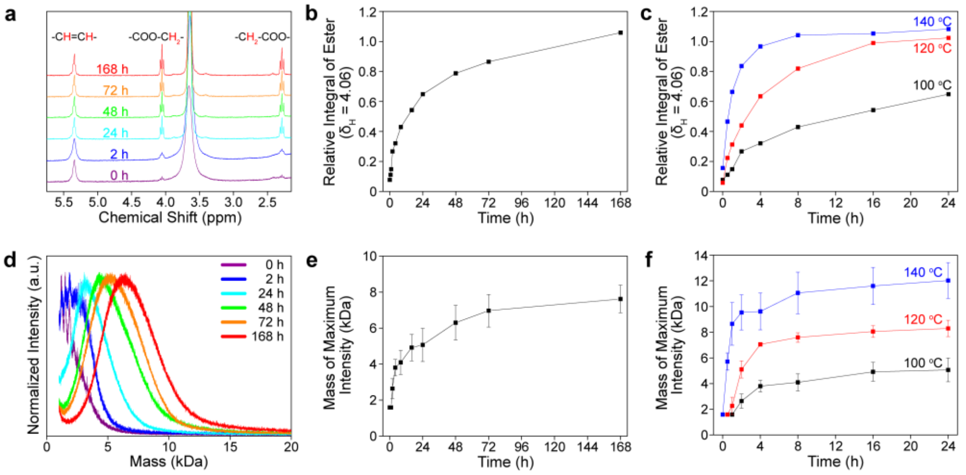

Figure 2.9 Evidence of continuous growth from the precursor to iron-oxo cluster at 100, 120, and 140 °C. (a) Change in ^{1}H NMR acquired from *ex situ* samples at 100 °C for 7 days. Strong peak observed at 3.6 ppm is assigned to hydroxyl hydrogen of 1-decanol. (b) Change in relative integral of ester at 100 °C for 7 days. (c) Change in relative integral of ester at different temperatures for 1 day. (d) Change in mass spectra at 100 °C for 7 days. (e) Change in mass of maximum intensity at 100 °C for 7 days. (f) Change in mass of maximum intensity at different temperatures for 1 day. Average and standard error of the mass of maximum intensity are presented in (e) and (f).

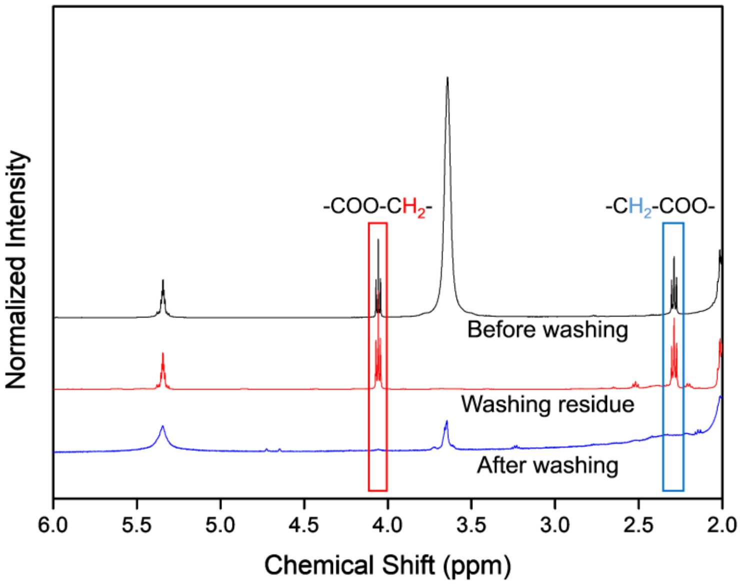

Figure 2.10 ^{1}H NMR spectra of crude product, washing residue, and final product. Esters are produced after continuous growth and separated after the washing process.

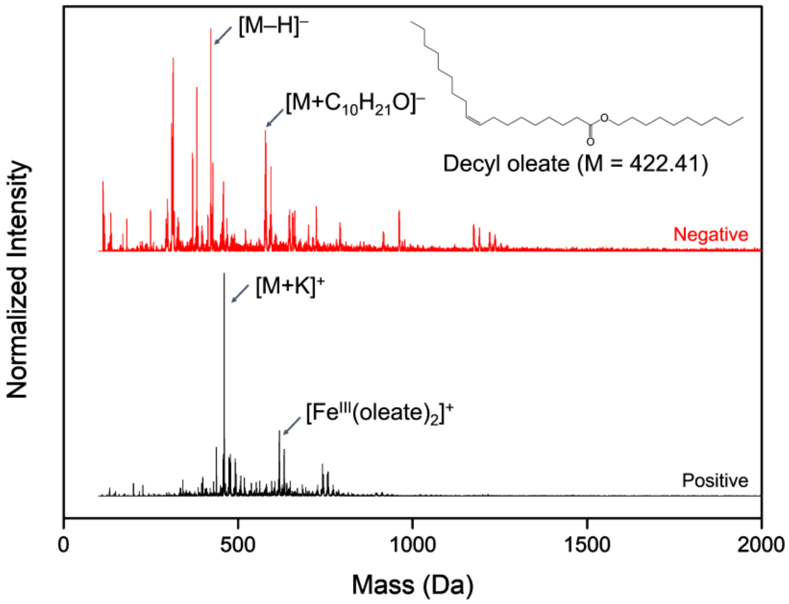

Figure 2.11 Mass spectrum of decyl oleate in washing solvent analyzed by LC-MS.

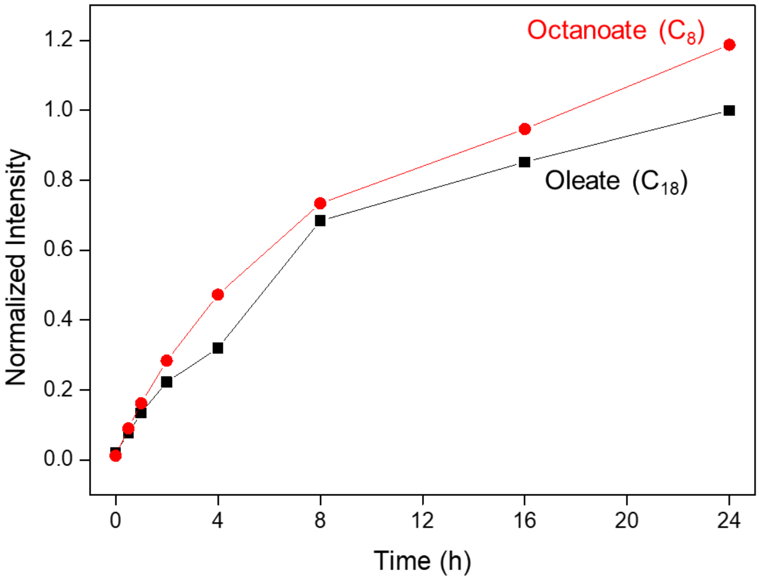

Figure 2.12 Kinetics of continuous esterification starting from iron-oxo-oleate (black) and iron-oxo-octanoate (red). Absolute quantification of ^1H NMR is applied to acquire both plots. At the same temperature, 100 ºC, continuous growth of iron-oxo clusters starting from iron-oxo-octanoate is about 1.15 faster than the case starting from iron-oxo-oleate.

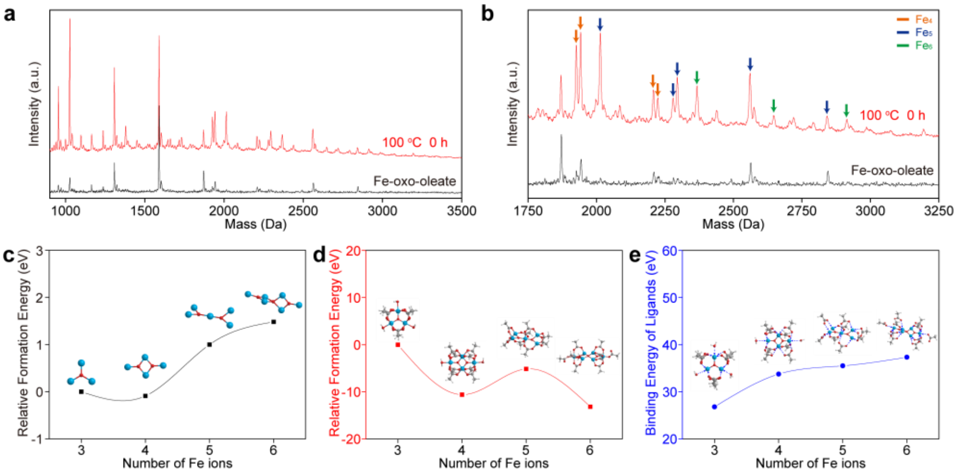

Figure 2.13 Change of mass spectra and relative formation energy at the early stage of esterification. (a) Mass spectra of iron-oxo-oleate (black), and *ex situ* aliquot at the early stage of esterification. (b) Detailed assignment of mass spectra: Fe_4 (orange), Fe_5 (blue), Fe_6 (green) species (see also Table 2.3). (c-e) Relative formation energy of iron-oxygen-core, iron-oxo-clusters and binding energy of acetate ligands bound to iron-oxygen-core are estimated by DFT calculation. (c) Relative formation energy of iron-oxygen core. The formation energy of Fe_3O core is set as zero. (d) Relative formation energy of iron-oxo-clusters. The formation energy of Fe_3O complex is set as zero. (e) Binding energy of ligands. The binding energy of ligands is calculated by subtracting the total energy with and without ligand binding moieties.

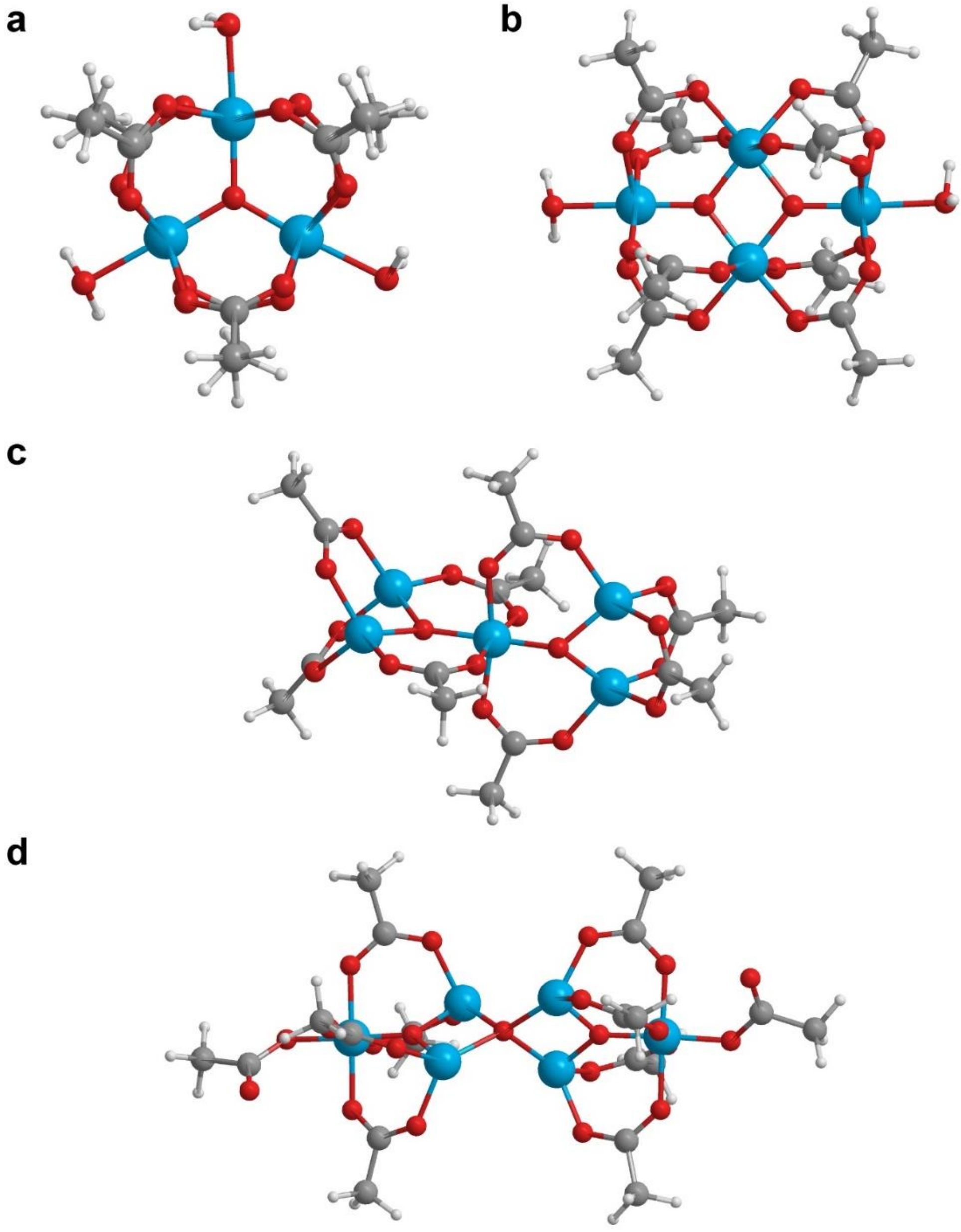

Figure 2.14 Theoretically derived structures of (a) Fe_3, (b) Fe_4, (c) Fe_5, and (d) Fe_6 clusters calculated by density functional theory.

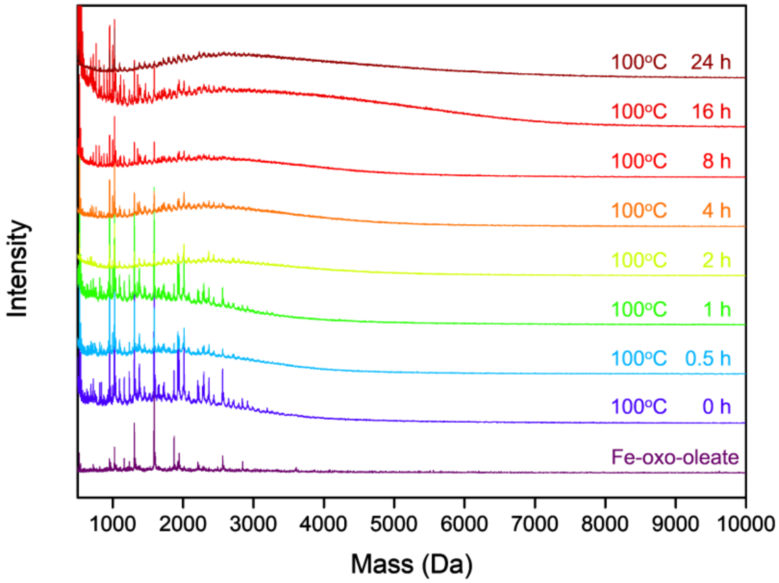

Figure 2.15 Mass spectra showing continuous growth mechanism at 100 °C.

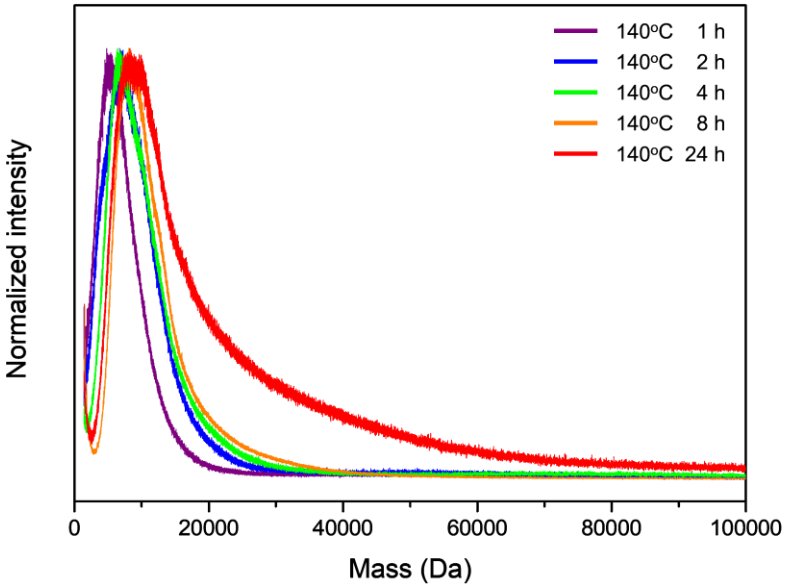

Figure 2.16 Mass spectra at 140 °C aging condition. After enough aging time, sub-nanometre iron-oxo clusters continuously grow into iron oxide nanoparticles (m/z > 20 kDa).

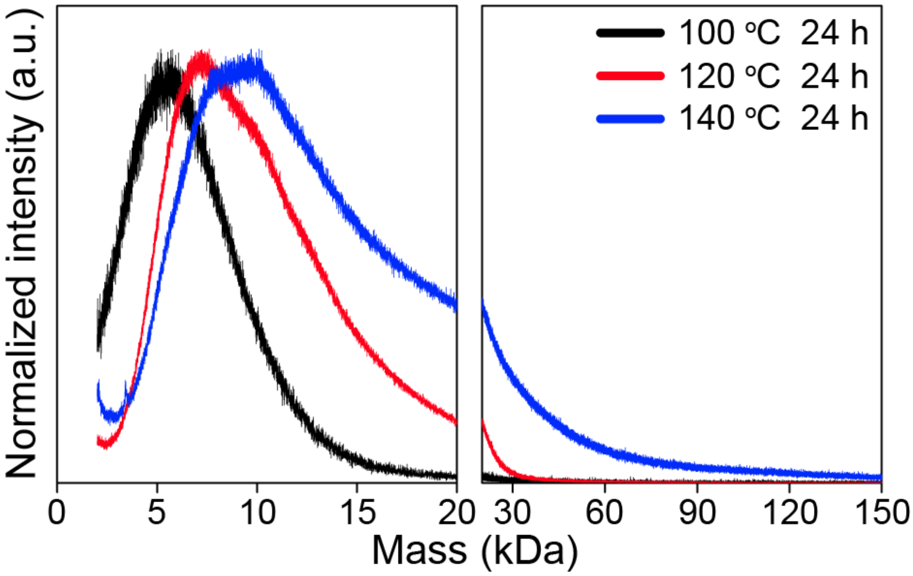

Figure 2.17 Mass spectra of iron-oxo clusters synthesized for 1 day at different temperatures. Final mass distributions show distinct effect of temperature on the rate of continuous growth.

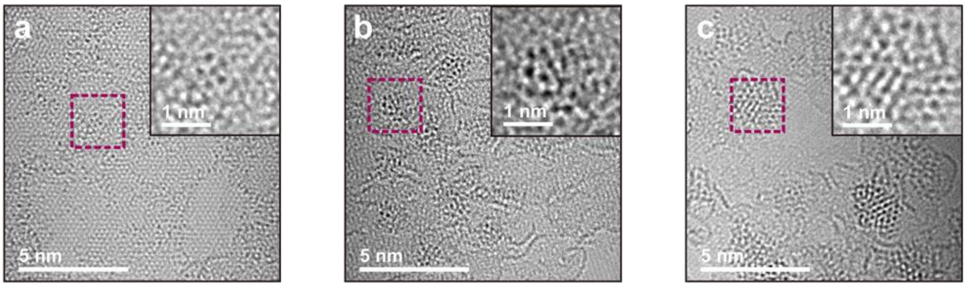

Figure 2.18 TEM images of iron-oxo clusters acquired from *ex situ* samples at 140 °C. (a) 0 h; (b) 4 h; and (c) 24 h aging. TEM images of iron-oxo clusters are presented in Figure 2.19, 2.20 and 2.21. TEM image of bare graphene substrate is shown in Figure 2.23.

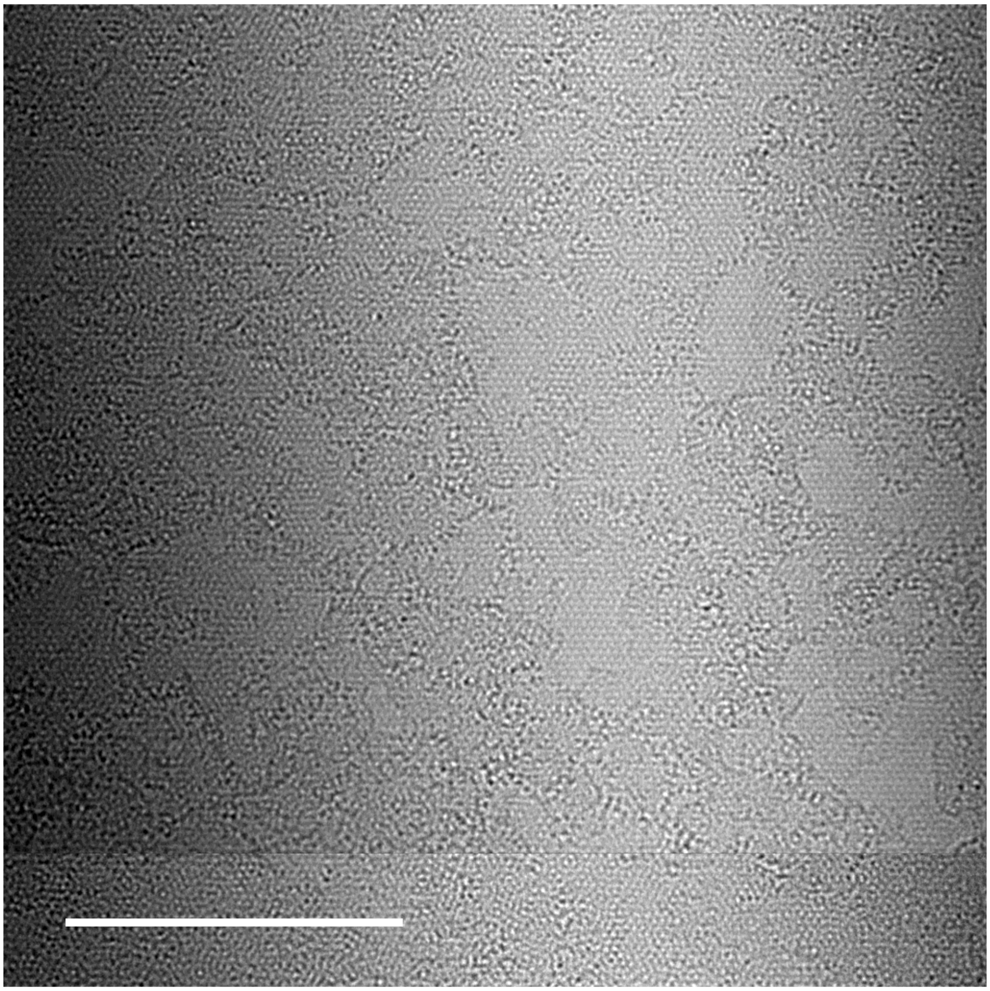

Figure 2.19 TEM image of iron-oxo clusters acquired from *ex situ* samples at 140 °C 0 h.

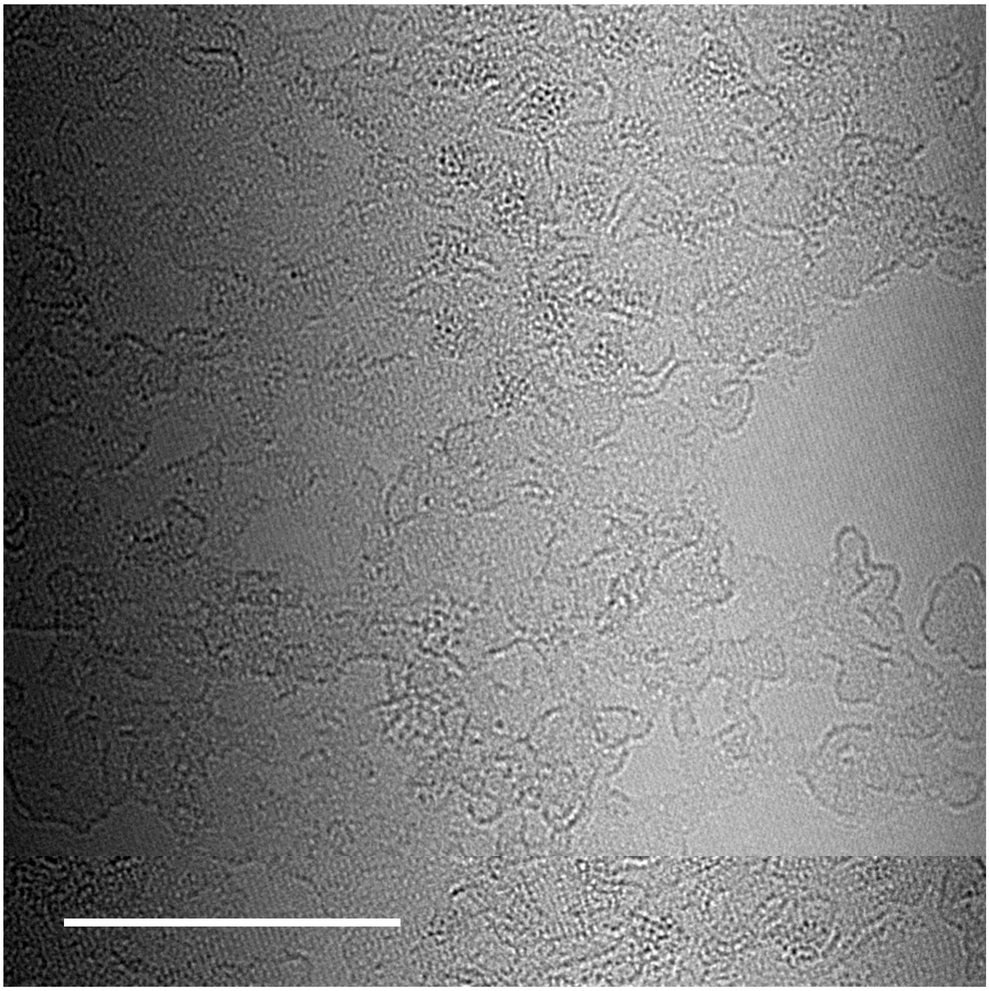

Figure 2.20 TEM image of iron-oxo clusters acquired from *ex situ* samples at 140 °C 4 h.

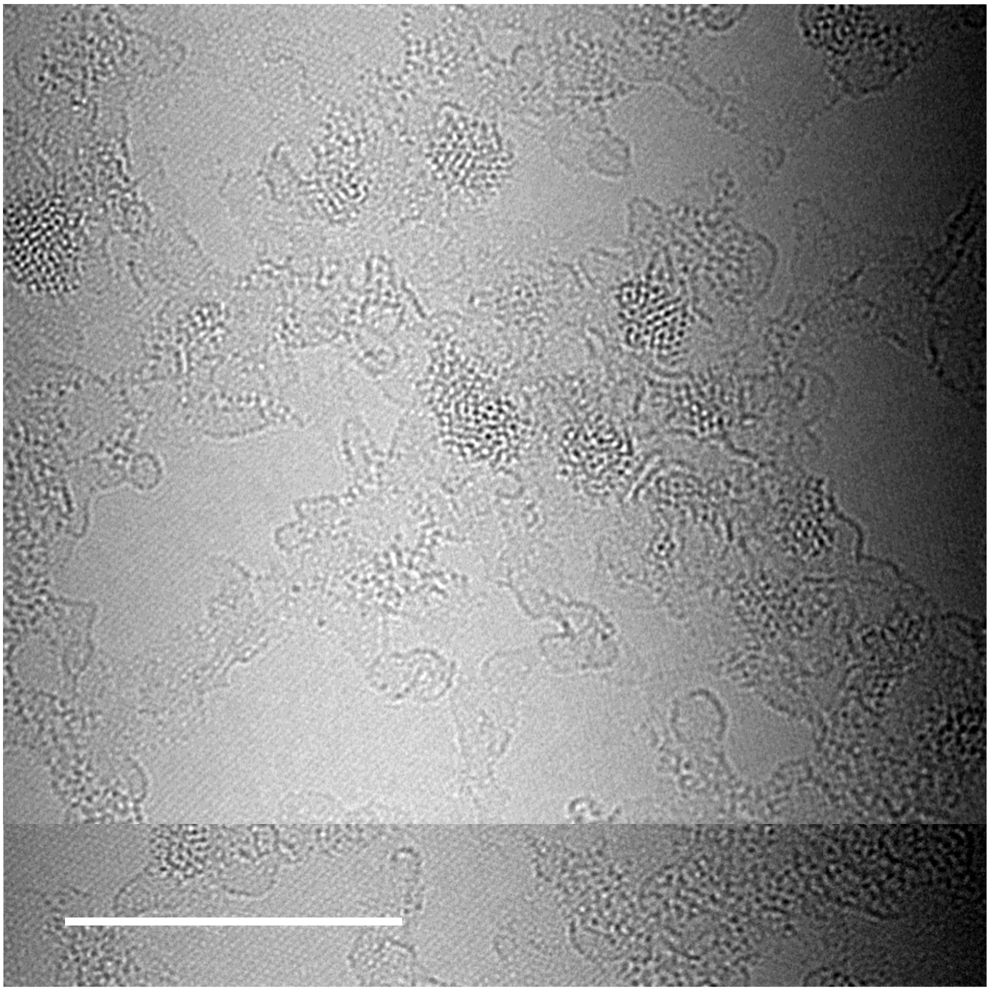

Figure 2.21 TEM image of iron-oxo clusters acquired from *ex situ* samples at 140 °C 24 h.

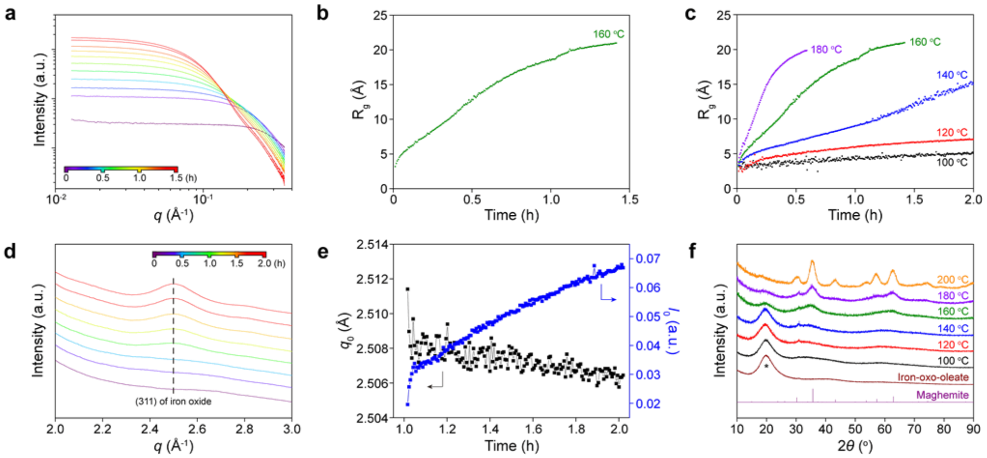

Figure 2.22 Confirmation of continuous growth by *in situ* X-ray scattering and X-ray diffraction. (a) Temporal evolution of small-angle X-ray scattering signals of iron-oleate precursors in 1-decanol solution. The reaction temperature is kept at 160 °C. (b) Change in radius of gyration derived from Guinier plot from the signals in panel (a). (c) Change in radius of gyration at different aging temperatures. (d) Temporal evolution of wide-angle X-ray scattering signals of the reacting solution at 160 °C. (e) Change in peak center and intensity of scattering peaks in panel (c). (f) X-ray diffraction patterns of final products synthesized at different aging temperatures. The broad diffraction peak, marked with asterisk, originated from disordered long-chain carboxylates.[71-72]

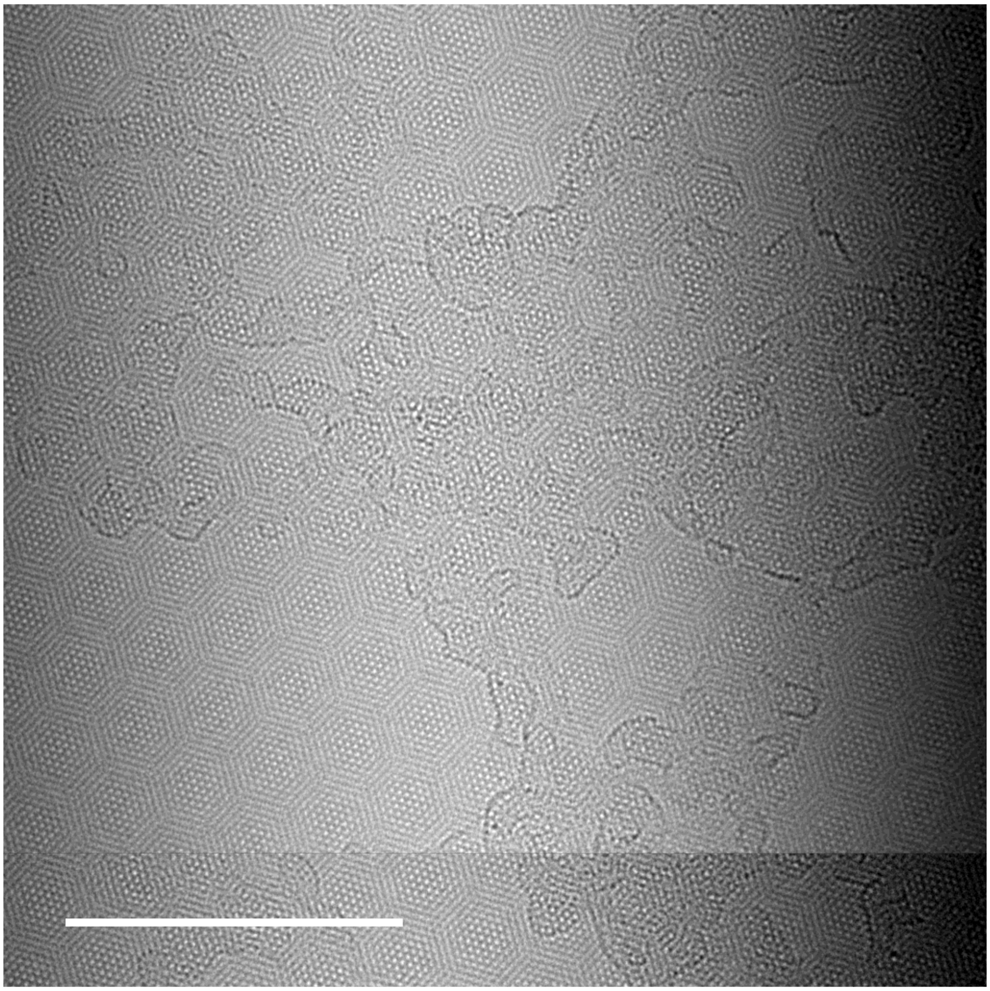

Figure 2.23 TEM image of graphene substrate loaded without any sample.

Table 2.3 Assignment of peaks shown in Figure 2.13b. Representative peaks of iron-oxo-oleate are shown in black. Peaks that dramatically emerged after esterification are shown in red. Peaks whose intensities distinctly increased after esterification are shown in green.

	955	1591	1645	1661	1716	1732	1872	1927	1943	2015	2086	2208	2224
Iron	2	3	4	4	5	5	3	4	4	5	6	4	4
Oxygen	0	1	1	2	2	3	1	1	2	3	4	1	2
Oleate	3	5	5	5	5	5	6	6	6	6	6	7	7

	2280	2296	2353	2368	2424	2440	2563	2579	2635	2650	2706	2722	2794
Iron	5	5	6	6	7	7	5	5	6	6	7	7	8
Oxygen	2	3	3	4	4	5	2	3	3	4	4	5	6
Oleate	7	7	7	7	7	7	8	8	8	8	8	8	8

	2844	2860	2916	2932	2988	3004	3194
Iron	5	5	6	6	7	7	6
Oxygen	2	3	3	4	4	5	3
Oleate	9	9	9	9	9	9	10

2.4 Conclusion

In this work, we elucidate that the continuous growth of iron-oxo-complexes into iron oxide nanoparticles is regulated by the strong binding between the metal-oxo-core and carboxylate ligands. The molecular structure of iron-oleate precursors and their entire growth trajectories are extensively verified by a combination of characterization methods and theoretical calculation. As the synthetic processes for various metal oxide nanoparticles are analogous to that we studied using metal-oleate complexes as starting precursors, the continuous growth process proposed in this work extends insights into the formation mechanism of various other metal oxide nanoparticles.

** Studies on this part was written based on the work conducted with Byung Hyo Kim (Co-first authors) which was reported on *Journal of the American Chemical Society*. (*J. Am. Chem. Soc.* **2019**, *141*, 7037–7045.)

2.5 Reference

[1] LaMer, V. K.; Dinegar, R. H., Theory, production and mechanism of formation of monodispersed hydrosols. *J. Am. Chem. Soc.* **1950,** *72*, 4847–4854.

[2] Talapin, D. V.; Rogach, A. L.; Haase, M.; Weller, H., Evolution of an ensemble of nanoparticles in a colloidal solution: theoretical study. *J. Phys. Chem. B* **2001,** *105*, 12278–12285.

[3] Kwon, S. G.; Hyeon, T., Formation mechanisms of uniform nanocrystals via hot-injection and heat-up methods. *Small* **2011,** *7*, 2685–2702.

[4] Murray, C. B.; Norris, D. J.; Bawendi, M. G., Synthesis and characterization of nearly monodisperse CdE (E = sulfur, selenium, tellurium) semiconductor nanocrystallites. *J. Am. Chem. Soc.* **1993,** *115*, 8706–8715.

[5] Kwon, S. G.; Piao, Y.; Park, J.; Angappane, S.; Jo, Y.; Hwang, N. M.; Park, J. G.; Hyeon, T., Kinetics of monodisperse iron oxide nanocrystal formation by "heating-up" process. *J. Am. Chem. Soc.* **2007,** *129*, 12571–12584.

[6] Owen, J. S.; Chan, E. M.; Liu, H.; Alivisatos, A. P., Precursor conversion kinetics and the nucleation of cadmium selenide nanocrystals. *J. Am. Chem. Soc.* **2010,** *132*, 18206–18213.

[7] Evans, C. M.; Evans, M. E.; Krauss, T. D., Mysteries of TOPSe revealed: insights into quantum dot nucleation. *J. Am. Chem. Soc.* **2010,** *132*, 10973–10975.

[8] Goulet, P. J.; Lennox, R. B., New insights into Brust-Schiffrin metal nanoparticle synthesis. *J. Am. Chem. Soc.* **2010,** *132*, 9582–9584.

[9] Cossairt, B. M.; Owen, J. S., CdSe clusters: at the interface of small molecules and quantum dots. *Chem. Mater.* **2011,** *23*, 3114–3119.

[10] Watzky, M. A.; Finke, R. G., Transition metal nanocluster formation kinetic and mechanistic studies. A new mechanism when hydrogen is the reductant: slow, continuous nucleation and fast autocatalytic surface growth. *J. Am. Chem. Soc.* **1997,** *119*, 10382–10400.

[11] Kim, B. H.; Shin, K.; Kwon, S. G.; Jang, Y.; Lee, H. S.; Lee, H.; Jun, S. W.; Lee, J.; Han, S. Y.; Yim, Y. H.; Kim, D. H.; Hyeon, T., Sizing by weighing: characterizing sizes of ultrasmall-sized iron oxide nanocrystals using MALDI-TOF mass spectrometry. *J. Am. Chem. Soc.* **2013,** *135*, 2407–2410.

[12] Wang, F.; Richards, V. N.; Shields, S. P.; Buhro, W. E., Kinetics and mechanisms of aggregative nanocrystal growth. *Chem. Mater.* **2014,** *26*, 5–21.

[13] Lee, J.; Yang, J.; Kwon, S. G.; Hyeon, T., Nonclassical nucleation and growth of inorganic nanoparticles. *Nat. Rev. Mater.* **2016,** *1*, 16034.

[14] Liu, M.; Wang, K.; Wang, L.; Han, S.; Fan, H.; Rowell, N.; Ripmeester, J. A.; Renoud, R.; Bian, F.; Zeng, J.; Yu, K., Probing intermediates of the induction period prior to nucleation and growth of semiconductor quantum dots. *Nat. Commun.* **2017,** *8*, 15467.

[15] Zheng, H.; Smith, R. K.; Jun, Y. w.; Kisielowski, C.; Dahmen, U.;

Alivisatos, A. P., Observation of single colloidal platinum nanocrystal growth trajectories. *Science* **2009,** *324*, 1309–1312.

[16] Yuk, J. M.; Park, J.; Ercius, P.; Kim, K.; Hellebusch, D. J.; Crommie, M. F.; Lee, J. Y.; Zettl, A.; Alivisatos, A. P., High-resolution EM of colloidal nanocrystal growth using graphene liquid cells. *Science* **2012,** *336*, 61–64.

[17] Loh, N. D.; Sen, S.; Bosman, M.; Tan, S. F.; Zhong, J.; Nijhuis, C. A.; Kral, P.; Matsudaira, P.; Mirsaidov, U., Multistep nucleation of nanocrystals in aqueous solution. *Nat. Chem.* **2017,** *9*, 77–82.

[18] Wu, Z.; Yang, S.; Wu, W., Shape control of inorganic nanoparticles from solution. *Nanoscale* **2016,** *8*, 1237–1259.

[19] Chan, E. M.; Xu, C.; Mao, A. W.; Han, G.; Owen, J. S.; Cohen, B. E.; Milliron, D. J., Reproducible, high-throughput synthesis of colloidal nanocrystals for optimization in multidimensional parameter space. *Nano Lett.* **2010,** *10*, 1874–1885.

[20] Kang, Y.; Li, M.; Cai, Y.; Cargnello, M.; Diaz, R. E.; Gordon, T. R.; Wieder, N. L.; Adzic, R. R.; Gorte, R. J.; Stach, E. A.; Murray, C. B., Heterogeneous catalysts need not be so "heterogeneous": monodisperse Pt nanocrystals by combining shape-controlled synthesis and purification by colloidal recrystallization. *J. Am. Chem. Soc.* **2013,** *135*, 2741–2747.

[21] Kwon, S. G.; Krylova, G.; Phillips, P. J.; Klie, R. F.; Chattopadhyay, S.; Shibata, T.; Bunel, E. E.; Liu, Y.; Prakapenka, V. B.; Lee, B.; Shevchenko, E. V., Heterogeneous nucleation and shape transformation of multicomponent

metallic nanostructures. *Nat. Mater.* **2015,** *14*, 215–223.

[22] Hendricks, M. P.; Campos, M. P.; Cleveland, G. T.; Jen-La Plante, I.; Owen, J. S., A tunable library of substituted thiourea precursors to metal sulfide nanocrystals. *Science* **2015,** *348*, 1226–1230.

[23] De Roo, J.; Van Driessche, I.; Martins, J. C.; Hens, Z., Colloidal metal oxide nanocrystal catalysis by sustained chemically driven ligand displacement. *Nat. Mater.* **2016,** *15*, 517–521.

[24] Xie, L.; Shen, Y.; Franke, D.; Sebastian, V.; Bawendi, M. G.; Jensen, K. F., Characterization of Indium Phosphide Quantum Dot Growth Intermediates Using MALDI-TOF Mass Spectrometry. *J. Am. Chem. Soc.* **2016,** *138*, 13469–13472.

[25] Gary, D. C.; Flowers, S. E.; Kaminsky, W.; Petrone, A.; Li, X.; Cossairt, B. M., Single-Crystal and Electronic Structure of a 1.3 nm Indium Phosphide Nanocluster. *J. Am. Chem. Soc.* **2016,** *138*, 1510–1513.

[26] Frenette, L. C.; Krauss, T. D., Uncovering active precursors in colloidal quantum dot synthesis. *Nat. Commun.* **2017,** *8*, 2082.

[27] Guntlin, C. P.; Ochsenbein, S. T.; Wörle, M.; Erni, R.; Kravchyk, K. V.; Kovalenko, M. V., Popcorn-shaped Fe_xO (wüstite) nanoparticles from a single-source precursor: colloidal synthesis and magnetic properties. *Chem. Mater.* **2018,** *30*, 1249–1256.

[28] Puzder, A.; Williamson, A. J.; Zaitseva, N.; Galli, G.; Manna, L.; Alivisatos, A. P., The effect of organic ligand binding on the growth of CdSe

nanoparticles probed by ab initio calculations. *Nano Lett.* **2004,** *4*, 2361–2365.

[29] Manna, L.; Wang, L. W.; Cingolani, R.; Alivisatos, A. P., First-principles modeling of unpassivated and surfactant-passivated bulk facets of wurtzite CdSe: a model system for studying the anisotropic growth of CdSe nanocrystals. *J. Phys. Chem. B* **2005,** *109*, 6183–6192.

[30] Rempel, J. Y.; Trout, B. L.; Bawendi, M. G.; Jensen, K. F., Density functional theory study of ligand binding on CdSe (0001), (0001), and (1120) single crystal relaxed and reconstructed surfaces: implications for nanocrystalline growth. *J. Phys. Chem. B* **2006,** *110*, 18007–18016.

[31] van Embden, J.; Mulvaney, P., Nucleation and growth of CdSe nanocrystals in a binary ligand system. *Langmuir* **2005,** *21*, 10226–10233.

[32] Joo, J.; Son, J. S.; Kwon, S. G.; Yu, J. H.; Hyeon, T., Low-temperature solution-phase synthesis of quantum well structured CdSe nanoribbons. *J. Am. Chem. Soc.* **2006,** *128*, 5632–5633.

[33] Yu, J. H.; Liu, X.; Kweon, K. E.; Joo, J.; Park, J.; Ko, K. T.; Lee, D. W.; Shen, S.; Tivakornsasithorn, K.; Son, J. S.; Park, J. H.; Kim, Y. W.; Hwang, G. S.; Dobrowolska, M.; Furdyna, J. K.; Hyeon, T., Giant Zeeman splitting in nucleation-controlled doped CdSe:Mn^{2+} quantum nanoribbons. *Nat. Mater.* **2010,** *9*, 47–53.

[34] Yang, J.; Fainblat, R.; Kwon, S. G.; Muckel, F.; Yu, J. H.; Terlinden, H.; Kim, B. H.; Iavarone, D.; Choi, M. K.; Kim, I. Y.; Park, I.; Hong, H. K.; Lee, J.; Son, J. S.; Lee, Z.; Kang, K.; Hwang, S. J.; Bacher, G.; Hyeon, T., Route

to the Smallest Doped Semiconductor: Mn^{2+}-Doped $(CdSe)_{13}$ Clusters. *J. Am. Chem. Soc.* **2015,** *137*, 12776–12779.

[35] Pearson, R. G., Hard and Soft Acids and Bases. *J. Am. Chem. Soc.* **1963,** *85*, 3533–3539.

[36] Joo, J.; Kwon, S. G.; Yu, J. H.; Hyeon, T., Synthesis of ZnO Nanocrystals with Cone, Hexagonal Cone, and Rod Shapes via Non-Hydrolytic Ester Elimination Sol–Gel Reactions. *Adv. Mater.* **2005,** *17*, 1873–1877.

[37] Niederberger, M., Nonaqueous sol-gel routes to metal oxide nanoparticles. *Acc. Chem. Res.* **2007,** *40*, 793–800.

[38] Kwon, S. G.; Hyeon, T., Colloidal chemical synthesis and formation kinetics of uniformly sized nanocrystals of metals, oxides, and chalcogenides. *Acc. Chem. Res.* **2008,** *41*, 1696–1709.

[39] Gatteschi, D.; Caneschi, A.; Sessoli, R.; Cornia, A., Magnetism of large iron-oxo clusters. *Chem. Soc. Rev.* **1996,** *25*, 101–109.

[40] Park, J.; An, K.; Hwang, Y.; Park, J. G.; Noh, H. J.; Kim, J. Y.; Park, J. H.; Hwang, N. M.; Hyeon, T., Ultra-large-scale syntheses of monodisperse nanocrystals. *Nat. Mater.* **2004,** *3*, 891–895.

[41] Huang, C.; Chung, P.; Tseng, I.-M.; Lee, L., Measurements and Correlations of Liquid-Liquid-Equilibria of the Mixtures Consisting of Ethanol, Water, Pentane, Hexane, and Cyclohexane. *Open Thermodynamics J.* **2010,** *4*, 102–118.

[42] Hynes, R. C.; Le Page, Y., Sucrose, a convenient test crystal for absolute

structures. *J. Appl. Crystallogr.* **1991,** *24*, 352–354.

[43] Petoukhov, M. V.; Konarev, P. V.; Kikhney, A. G.; Svergun, D. I., ATSAS 2.1 – towards automated and web-supported small-angle scattering data analysis. *J. Appl. Crystallogr.* **2007,** *40*, s223–s228.

[44] Abecassis, B.; Bouet, C.; Garnero, C.; Constantin, D.; Lequeux, N.; Ithurria, S.; Dubertret, B.; Pauw, B. R.; Pontoni, D., Real-time in situ probing of high-temperature quantum dots solution synthesis. *Nano Lett.* **2015,** *15*, 2620–2626.

[45] Kohn, W.; Sham, L. J., Self-consistent equations including exchange and correlation effects. *Phys. Rev.* **1965,** *140*, A1133–A1138.

[46] Kresse, G.; Joubert, D., From ultrasoft pseudopotentials to the projector augmented-wave method. *Phys. Rev. B* **1999,** *59*, 1758–1775.

[47] Perdew, J. P.; Burke, K.; Ernzerhof, M., Generalized gradient approximation made simple. *Phys. Rev. Lett.* **1996,** *77*, 3865–3868.

[48] (a) Mehrotra, R. C.; Bohra, R., *Metal Carboxylates*. Academic Press: 1983. (b) McCleverty, J. A.; Meyer, T. J., *Comprehensive coordination chemistry II.* Elsevier Ltd: 2004; Vol. 5.

[49] Oh, S. M.; Hendrickson, D. N.; Hassett, K. L.; Davis, R. E., Electron transfer in mixed-valence, oxo-centered, trinuclear iron acetate complexes: effect of statically disordered to dynamically disordered transformation in the solid state. *J. Am. Chem. Soc.* **1984,** *106*, 7984–7985.

[50] Oh, S. M.; Henderickson, D. N.; Hassett, K. L.; Davis, R. E., Valence-

detrapping modes for electron transfer in the solid state of mixed-valence, oxo-centered, trinuclear iron acetate complexes: x-ray structure and physical data for [$Fe_3O(O_2CCH_3)_6$(4-Et-py)$_3$](4-Et-py). *J. Am. Chem. Soc.* **1985,** *107*, 8009–8018.

[51] Long, G. J.; Robinson, W. T.; Tappmeyer, W. P.; Bridges, D. L., The magnetic, electronic, and Mössbauer spectral properties of several trinuclear iron(III) carboxylate complexes. *J. Chem. Soc., Dalton Trans.* **1973**, 573–579.

[52] Blake, A. B.; Yavari, A.; Hatfield, W. E.; Sethulekshmi, C. N., Magnetic and spectroscopic properties of some heterotrinuclear basic acetates of chromium(III), iron(III), and divalent metal ions. *J. Chem. Soc., Dalton Trans.* **1985**, 2509–2520.

[53] Abrahamson, H. B.; Lukaski, H. C., Synthesis and characterization of iron stearate compounds. *J. Inorg. Biochem.* **1994,** *54*, 115–130.

[54] Baran, P.; Boča, R.; Chakraborty, I.; Giapintzakis, J.; Herchel, R.; Huang, Q.; McGrady, J. E.; Raptis, R. G.; Sanakis, Y.; Simopoulos, A., Synthesis, Characterization, and Study of Octanuclear Iron-Oxo Clusters Containing a Redox-Active Fe_4O_4-Cubane Core. *Inorg. Chem.* **2008,** *47*, 645–655.

[55] Nakamoto, K., *Infrared and Raman Spectra of Inorganic and Coordination Compounds*. John Wiley & Sons, Inc., New Jersey: 2008.

[56] Johnson, M. K.; Powell, D. B.; Cannon, R. D., Vibrational spectra of carboxylato complexes—III. Trinuclear 'basic' acetates and formates of chromium(III), iron(III) and other transition metals. *Spectrochim. Acta A*

1981, *37*, 995–1006.

[57] Amani, V.; Safari, N.; Khavasi, H. R., Solution and solid state characterization of oxo-centered trinuclear iron(III) acetate complexes $[Fe_3(\mu_3\text{-}O)(\mu\text{-}OAc)_6(L)_3]^+$. *Spectrochim. Acta A* **2012,** *85*, 17–24.

[58] Belmore, K.; Madison, X. J.; Harton, A.; Vincent, J. B., Carbon-13 NMR studies of oxo-centered trinuclear chromium(III) complexes of the general formula $[Cr_3O(O_2CR)_6(L)_3]^+$ (R = Me, Ph; L = H_2O, py). *Spectrochim. Acta A* **1994,** *50*, 2365–2370.

[59] Lynch, J.; Zhuang, J.; Wang, T.; LaMontagne, D.; Wu, H.; Cao, Y. C., Gas-bubble effects on the formation of colloidal iron oxide nanocrystals. *J. Am. Chem. Soc.* **2011,** *133*, 12664–12674.

[60] Kim, B. H.; Lee, N.; Kim, H.; An, K.; Park, Y. I.; Choi, Y.; Shin, K.; Lee, Y.; Kwon, S. G.; Na, H. B.; Park, J. G.; Ahn, T. Y.; Kim, Y. W.; Moon, W. K.; Choi, S. H.; Hyeon, T., Large-scale synthesis of uniform and extremely small-sized iron oxide nanoparticles for high-resolution T1 magnetic resonance imaging contrast agents. *J. Am. Chem. Soc.* **2011,** *133*, 12624–12631.

[61] Ito, D.; Yokoyama, S.; Zaikova, T.; Masuko, K.; Hutchison, J. E., Synthesis of ligand-stabilized metal oxide nanocrystals and epitaxial core/shell nanocrystals via a lower-temperature esterification process. *ACS Nano* **2014,** *8*, 64–75.

[62] Harris, R. A.; Shumbula, P. M.; van der Walt, H., Analysis of the interaction of surfactants oleic acid and oleylamine with iron oxide

nanoparticles through molecular mechanics modeling. *Langmuir* **2015,** *31*, 3934–3943.

[63] Al-Johani, H.; Abou-Hamad, E.; Jedidi, A.; Widdifield, C. M.; Viger-Gravel, J.; Sangaru, S. S.; Gajan, D.; Anjum, D. H.; Ould-Chikh, S.; Hedhili, M. N.; Gurinov, A.; Kelly, M. J.; El Eter, M.; Cavallo, L.; Emsley, L.; Basset, J. M., The structure and binding mode of citrate in the stabilization of gold nanoparticles. *Nat. Chem.* **2017,** *9*, 890–895.

[64] Jao, M.-H.; Cheng, C.-C.; Lu, C.-F.; Hsiao, K.-C.; Su, W.-F., Low temperature and rapid formation of high quality metal oxide thin film via a hydroxide-assisted energy conservation strategy. *J. Mater. Chem. C* **2018,** *6*, 9941-9949.

[65] Nair, R. R.; Blake, P.; Blake, J. R.; Zan, R.; Anissimova, S.; Bangert, U.; Golovanov, A. P.; Morozov, S. V.; Geim, A. K.; Novoselov, K. S.; Latychevskaia, T., Graphene as a transparent conductive support for studying biological molecules by transmission electron microscopy. *Appl. Phys. Lett.* **2010,** *97*, 153102.

[66] Bosch-Navarro, C.; Laker, Z. P.; Thomas, H. R.; Marsden, A. J.; Sloan, J.; Wilson, N. R.; Rourke, J. P., Covalently binding atomically designed Au_9 clusters to chemically modified graphene. *Angew. Chem. Int. Ed.* **2015,** *54*, 9560–9563.

[67] Park, J.; Elmlund, H.; Ercius, P.; Yuk, J. M.; Limmer, D. T.; Chen, Q.; Kim, K.; Han, S. H.; Weitz, D. A.; Zettl, A.; Alivisatos, A. P., Nanoparticle

imaging. 3D structure of individual nanocrystals in solution by electron microscopy. *Science* **2015,** *349*, 290–295.

[68] Polte, J.; Ahner, T. T.; Delissen, F.; Sokolov, S.; Emmerling, F.; Thunemann, A. F.; Kraehnert, R., Mechanism of gold nanoparticle formation in the classical citrate synthesis method derived from coupled in situ XANES and SAXS evaluation. *J. Am. Chem. Soc.* **2010,** *132*, 1296–1301.

[69] Lassenberger, A.; Grunewald, T. A.; van Oostrum, P. D. J.; Rennhofer, H.; Amenitsch, H.; Zirbs, R.; Lichtenegger, H. C.; Reimhult, E., Monodisperse iron oxide nanoparticles by thermal decomposition: elucidating particle formation by second-resolved in situ small-angle X-ray scattering. *Chem. Mater.* **2017,** *29*, 4511–4522.

[70] Maes, J.; Castro, N.; De Nolf, K.; Walravens, W.; Abécassis, B.; Hens, Z., Size and Concentration Determination of Colloidal Nanocrystals by Small-Angle X-ray Scattering. *Chem. Mater.* **2018,** *30*, 3952–3962.

[71] Jandacek, R. J.; Broering, W. B., X-ray diffraction study of sodium soaps of monounsaturated and polyunsaturated fatty acids. *Lipids* **1989,** *24*, 1008–1013.

[72] Corkery, R. W., A variation on Luzzati's soap phases. Room temperature thermotropic liquid crystals. *Phys. Chem. Chem. Phys.* **2004,** *6*, 1534–1546.

Chapter 3. $Cd_{12}Ag_{32}(SePh)_{36}$: Non-Noble Metal Doped Silver Nanoclusters

** Reprinted with permission from *J. Am. Chem. Soc.* **2019**, *141*, 8422–8425.

3.1 Introduction

Ligand stabilized few-atom (tens to hundreds) nanoclusters (NCs) of metals such as Au, Ag and Cu have gained much attention in recent years for their intriguing properties, including photoluminescence (PL), optical activity, catalysis, and size- and structure-conversion.[1-4] The NCs (typical size <3 nm) bridge the gap between the metal-ligand complexes and nanoparticles (NPs, size >3 nm). Unlike the classical NPs with large size and composition distributions, the NCs are truly single-sized with precise molecular formulae. Thus, NCs are the potential candidates to gain fundamental insights into the evolution of optical and catalytic properties of materials from discrete atomic to molecular levels.[5-8]

Since the first report on the X-ray crystal structure of ligated Au_{102} cluster,[9] several Au, Ag and their heteroatom doped NCs have been synthesized and atomic structures determined.[1-3,10] The size, structure and composition are shown to influence the cluster properties significantly. The former two are generally directed by the choice of ligands.[1-3,11] The common ligands used to attain different clusters are thiols, selenols, alkynyls, halides, hydrides, phosphines or their combinations,[1,2,12-17] in which selenols are rarely used for stabilizing Ag clusters.[18,19]

Another path to modulate the cluster properties is by modifying the metal composition through substitutional doping with heteroatoms.[20,21] The doped NCs exhibit enhanced properties compared to undoped ones owing to synergistic effects.[4,22,23] The dopants incorporated into Au and Ag NCs are mostly the noble metals such as Pd and Pt due to their close atomic diameters.[1,20] In contrast, doping a noble metal NC with a non-noble metal such as Cd is challenging largely due to mismatch in their atomic sizes and standard reduction potentials. Recently, several Cd doped Au NCs were synthesized by post-synthetic modification processes,[24-27] while those of Ag remain unexplored.

Here, we report a novel synthetic method for the non-noble metal doped Ag NCs by a phosphine assisted process. Specifically, by using triphenylphosphine (PPh_3) as an assisting ligand and Cd as dopant, we successfully synthesized a selenophenolate stabilized Ag NC, $Cd_{12}Ag_{32}(SePh)_{36}$. The details of its synthesis (Figure 3.1) and purification procedures are provided in the Experimental section. The single crystals of NCs were grown (Figure 3.2) by the vapor diffusion of n-pentane into a DCM solution of the cluster.

Figure 3.1 The digital photographs describing the synthesis of $Cd_{12}Ag_{32}(SePh)_{36}$ cluster. (A) The yellow, insoluble metal-selenolates formed from Cd^{2+}, Ag^+ and PhSeH in a solution of ethanol and DCM. (B) Dissolution of metal-selenolates as metal-selenolate-phosphine complexes after introducing PPh_3 and TOAB. (C) A dark solution of $Cd_{12}Ag_{32}(SePh)_{36}$ clusters formed after borohydride reduction of metal-ligand complexes.

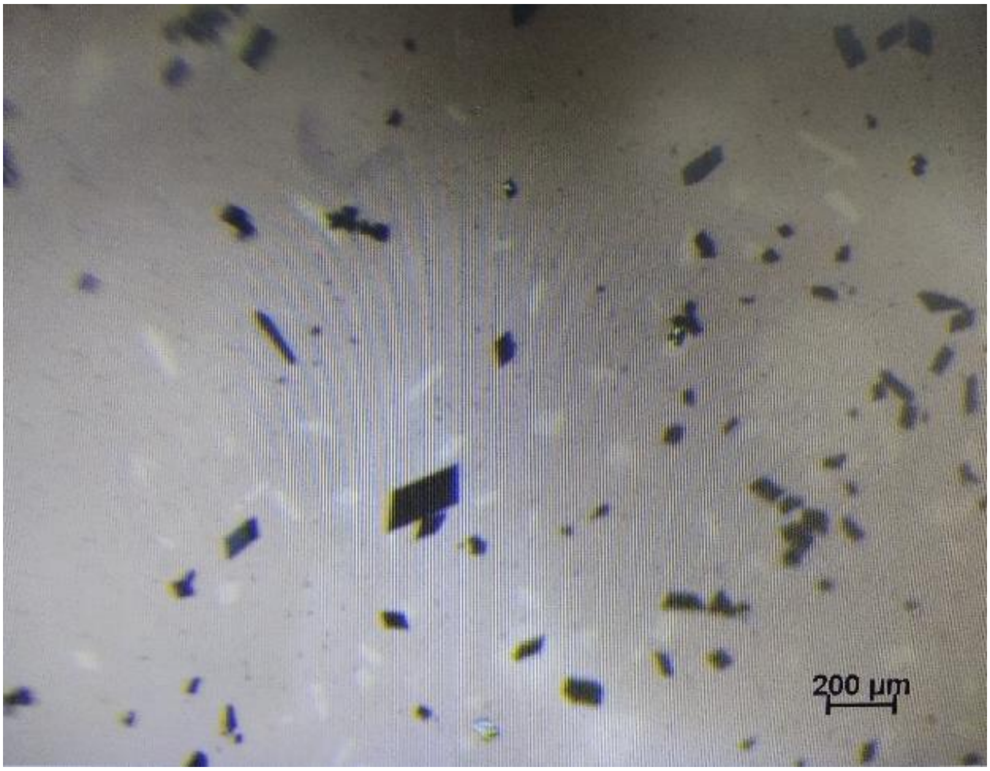

Figure 3.2 An optical microscopic image of the single crystals of $Cd_{12}Ag_{32}(SePh)_{36}$ clusters, which are grown by the vapor diffusion of n-pentane into a concentrated DCM solution of the cluster.

3.2 Experimental

Chemicals. The following chemicals and solvents were purchased from various sources and used them without further purification. Cadmium nitrate tetrahydrate [$Cd(NO_3)_2 \cdot 4H_2O$], silver nitrate ($AgNO_3$), triphenylphosphine (PPh_3), tetraoctylammonium bromide (TOAB), tetrabutylammonium bromide (TBAB), sodium borohydride ($NaBH_4$), trans-2-[3-(4-tert-butylphenyl)-2-methyl-2-propenylidene]malononitrile (DCTB, ≥98%) and deuterated chloroform ($CDCl_3$) were received from Sigma-Aldrich. Selenophenol (PhSeH, 98%, from Acros Organics), 4-fluorothiophenol (4-FTP, 97%, from Acros Organics) and 2,4-dichlorobenzenethiol (2,4-DCBT, >97%, from TCI) were purchased. Solvents, ethanol (EtOH, 99.9%), N,N-dimethylformamide (DMF, 99%) and n-pentane (99%) were received from Samchun and dichloromethane (DCM, 99%) was acquired from Alfa Aesar.

Synthesis of $Cd_{12}Ag_{32}(SePh)_{36}$ nanoclusters. 20 mg of $AgNO_3$ and 10 mg of $Cd(NO_3)_2 \cdot 4H_2O$ were dissolved in 10 mL of ethanol by sonication after transferring them into a 50 mL three neck round bottom flask. To this solution, under magnetic stirring at 1000 rpm, 10 μL of PhSeH was added, resulting a yellow turbid metal-selenolates. Then, 20 mL DCM solution containing 100 mg of PPh_3 and 15 mg TOAB was dropped into the above solution. Within five minutes, the turbid metal-selenolates were dissolved through the formation of metal-selenolate-phosphine (Ag-Cd-Se-P) complexes, producing a transparent solution. These metal-ligand soluble complexes were reduced with 10 mg of $NaBH_4$ dispersed in 3 mL ethanol under argon atmosphere (Note: reduction in air resulted undesired plasmonic silver nanoparticles). The colorless solution turned orange, brown and deep black sequentially within 15 minutes, indicating the formation of nanoclusters. This solution was continuously stirred for 24 h at room temperature. After that, the solution was centrifuged and the supernatant was concentrated using a rotary evaporator. Once DCM was removed, the cluster precipitated out from the solution, which was collected by centrifugation at 5000 rpm for 5 minutes. This precipitate was repeatedly washed with ethanol to remove excess ligands if any. Finally, the synthesized product was completely dried under vacuum and stored in a refrigerator for further use. The $[Cu_{12}Ag_{28}(2,4\text{-DCBT})_{24}]^{4-}$ and $[Ag_{44}(4\text{-FTP})_{30}]^{4-}$ clusters were synthesized following literature reports.[28,29]

Crystallization of $Cd_{12}Ag_{32}(SePh)_{36}$ nanoclusters. About 2-3 mg of the dried $Cd_{12}Ag_{32}(SePh)_{36}$ nanoclusters was dissolved in clean DCM (500 μL) and filtered using a syringe filter with a pore size of 0.22 μm. The filtrate was transferred into a 5 mL glass vial. This vial was placed inside a 20 mL glass vial that containing 2 mL of clean n-pentane. The large vial was capped and placed in a refrigerator at 5 °C. Due to the vapor diffusion of n-pentane into the DCM solution, the dark single crystals suitable for the single crystal X-ray diffraction (SCXRD) were observed after a week.

UV-vis absorption spectroscopy. The UV-vis spectra of the solutions of nanoclusters were measured using a Cary 5000 UV-Vis-NIR spectrophotometer (Agilent).

Photoluminescence (PL) spectroscopy. The PL and PL excitation (PLE) spectra of the solutions of nanoclusters were recorded using an FLS 980 spectrometer (Edinburgh Instruments). The PL quantum yield (PLQY: ~0.28%) of $Cd_{12}Ag_{32}(SePh)_{36}$ cluster (in DCM) was calculated using the following expression with respect to $[Ag_{44}(4\text{-}FTP)_{30}]^{4-}$ cluster.[29]

$$\Phi_X = \Phi_{ST}\ [Grad(X) \div Grad\ \ (ST)]\ [(\eta_X)^2\ \div\ (\eta_{ST})^2]$$

Here, X and ST = $Cd_{12}Ag_{32}(SePh)_{36}$ and $[Ag_{44}(4\text{-}FTP)_{30}]^{4-}$ clusters, respectively; Φ_{ST} = QY of $[Ag_{44}(4\text{-}FTP)_{30}]^{4-}$ i.e., 0.01% (in DMF); Grad = slopes of the absorbance versus PL area plots; η = refractive index of the solvent.

Matrix-assisted laser desorption ionization time of flight (MALDI-TOF). Mass spectrometry was performed using a home-built MALDI-TOF instrument. The instrument was calibrated using calibrants, 3-aminoquinone (Mw = 144.17 Da), Y5R peptide (Mw = 990.08 Da), insulin (Mw = 5735.6087 Da), and cytochrome C (Mw = 12361.97 Da. The analyte and DCTB matrix were properly mixed in DCM to obtain optimized mass profiles.

The mixture was dried on a sample plate with vacuum evaporation, and the dried samples were desorbed and ionized by a 337 nm nitrogen laser (MNL100, Lasertechnik Berlin, Germany) with an accelerating voltage of 20.0 kV and laser power of 1.7-9.3 μJ. Each spectrum was acquired by focusing 200 laser shots on each spot.

Nuclear magnetic resonance (NMR) spectroscopy. Liquid-state ^{1}H and ^{31}P NMR spectra were recorded using a Bruker Avance III 400 FT-NMR spectrometer by dissolving the desired samples in $CDCl_3$. For understanding the role of phosphine in the nanoclusters synthesis using NMR, 500 μL solution from the reaction mixture was withdrawn at the desired times and vacuum dried.

Scanning electron microscopy energy dispersive X-ray spectroscopy (SEM EDS). The FE-SEM images and EDS of Cd doped Ag cluster were obtained from JSM-7800F Prime microscope (JEOL, Japan).

Thermogravimetric analysis (TGA). TGA of about 2 mg of single crystals of AgCd clusters was carried out using a SDT Q600 apparatus (TA instrument, USA) under Ar gas (50 mL/minute) in the temperature range of 50-1000 °C with a heating rate 10 °C/min.

Inductively coupled plasma atomic emission spectroscopy (ICP AES).

The ICP AES was conducted on a Shimadzu (ICPS-8100) spectrometer. The samples were prepared by washing the single crystals of $Cd_{12}Ag_{32}(SePh)_{36}$ with ethanol followed by dissolving in DCM. This DCM solution was centrifuged and the supernatant was vacuum dried. The dry solid was digested with an acid mixture of concentrated HNO_3 and HCl (1:3 vol:vol).

Scanning transmission electron microscopy EDS (STEM EDS). A clean cluster sample in DCM was used to measure the STEM EDS using a JEOL EM-2010 microscope operated at 200 kV.

Fourier transform infrared spectroscopy (FTIR). FTIR spectra of cluster film were recorded on a TENSOR27 (Bruker, Germany) spectrometer.

Single-crystal X-ray diffraction (SCXRD). The diffraction data of $Cd_{12}Ag_{32}(SePh)_{36}$ cluster were collected on an Agilent Technologies SuperNova system with Cu Kα radiation (λ = 1.54184 Å) at 100 K. All the data were processed using CrysAlisPro.[30] All structures were solved and refined using Full-matrix least-squares based on F2 with the program ShelXT[31] and ShelXL[32] within Olex2.[33]

Computational details. We used density-functional theory (DFT) as implemented for real-space calculations in the code package GPAW.[34] The structural relaxations and the ground state electronic structure analysis were done in a 3D real-space grid with 0.2 Å grid spacing. The electron-electron exchange-correlation (xc) effects were approximated by the PBE (Perdew-Burke-Ernzerhof) xc-functional.[35] Structure optimizations were stopped when residual forces were below 0.05 eV/Å. The scalar-relativistic effects were included in the atomic setups of GPAW. The initial atomic structure was taken from the experimental crystal structure. Optical absorption and CD spectra were calculated with 0.25 Å grid spacing using linear response time-dependent density functional theory (LR-TDDFT) in Casida formalism.[36] Spectra were calculated both for the experimental crystal structure and for the PBE-relaxed structure. Peaks and shoulders in the optical absorption spectra were analyzed by using dipole transition contribution maps (DTCM) using time dependent density functional perturbation theory (TD-DFPT).[37] The superatomic nature of the cluster was studied with Y_{lm}-analysis by projecting the electron states to spherical harmonics centered at the center of the mass of the cluster.[38] Atomic charges were analyzed with the Bader method.[39] To estimate the emission wavelengths computationally, we relaxed the cluster in the excited singlet (S_1) and triplet (T_1) states with fixed electron state occupations. The emission energies E_1, E_2 were obtained from total energy difference to the singlet ground state (S_0) in excited state geometries:

$E_1 = E(S_1) - E(S_{0,S})$ corresponding to 1134 nm and $E_2 = E(T_1) - E(S_{0,T})$ corresponding to 1150 nm.

3.3 Results and discussions

3.3.1 Structure of Cd-doped Ag clusters

The single crystal X-ray diffraction (SCXRD) analysis reveals that the final product is a 44 metal atom cluster stabilized by 36 SePh ligands with a molecular formula, $Cd_{12}Ag_{32}(SePh)_{36}$ (Figure 3.3). Clearly, the Cd atoms are located on the cluster surface. The cluster crystallizes in a triclinic system of *P-1* space group (Table 3.1) and its unit cell comprises two NCs (Figure 3.4). No counterions were identified in the structure, indicating that the cluster is neutral. The detailed structural analysis (Figure 3.5) shows that the NC consists of a Ag_{28} core stabilized by four $Cd_3Ag(SePh)_9$ motifs. Further anatomy of the Ag_{28} core unveils a Ag_4 tetrahedron (Figure 3.5A) at the center. The average Ag-Ag bond distance of 2.84 Å is close to that of the bulk Ag, indicating the strong Ag-Ag interactions in the NC. Six Ag atoms arrange nearly coplanarly to form a Ag_6 facet with four triangles (Figure 3.5B). Such four Ag_6 facets cap the four faces of Ag_4 tetrahedron to form a structure shown in Figure 3.5C. The interfacet interactions through Ag-Ag bonding produce a Ag_{24} layer and it completely encapsulates the Ag_4 tetrahedron, forming a two-shell $Ag_4@Ag_{24}$ core (Figure 3.5D). Notably, the central Ag_3 triangles of Ag_6 facets (placed exactly on top of the triangular faces of inner Ag_4 core) are significantly elongated from the Ag_4 core compared to other Ag-Ag bonds (Table 3.2).

In $Cd_3Ag(SePh)_9$ surface motif (Figure 3.5E), each Cd atom is tetrahedrally coordinated with four Se atoms of four SePh ligands. Totally, three Se atoms from three $CdSe_4$ tetrahedrons bind with one Ag to form a $AgSe_3$ cap-like structure, forming the $Cd_3Ag(SePh)_9$ motif. The capping of four $Cd_3Ag(SePh)_9$ motifs on four Ag_6 facets of Ag_{28}, through Se atoms that are unbound to motif Ag atoms, produces the total structure of $Cd_{12}Ag_{32}(SePh)_{36}$ cluster (Figure 3.5F). Notably, 12 and 24 Se atoms appear in μ-3 and μ-2 bridging modes, respectively. All the four $Cd_3Ag(SePh)_9$ motifs are mounted over four triangular faces of inner Ag_4 tetrahedron, and therefore, it imparts the tetrahedral shape to the final structure. A similar Ag_{28} core of our cluster is observed in $[Cu_{12}Ag_{28}(SR)_{24}]^{4-}$ cluster,[28] however with vividly different metal and ligand composition, electronic charge and the surface structure.

The presence of Cd, Ag and Se in the cluster was supported by energy dispersive X-ray spectroscopy (Figure 3.6). The matrix-assisted laser desorption ionization mass spectrometry shows only a single high-mass peak at ~9.6kDa, indicating that the cluster is single-sized. This peak with lower in mass by ~0.7kDa compared to 10.3kDa for $Cd_{12}Ag_{32}(SePh)_{36}$ may be due to the fragmentation often observed in the Ag clusters[11] (Figure 3.7). The formula of the cluster is further validated by the elemental analysis (Figure 3.8). The thermogravimetric analysis shows a total weight loss of 54.5%, very close to a theoretical ligand weight of the cluster 54.0% (Figure 3.9). ^1H nuclear magnetic resonance (NMR) spectrum of the cluster (Figure 3.10) shows proton signals spread between 6-8 ppm for SePh protection,[12] which is also in agreement with the infrared analysis (Figure 3.11). The absence of H and P signals for PPh_3 ligands, which were used during the cluster synthesis, in ^1H and ^{31}P NMR spectra is consistent with the SCXRD results.

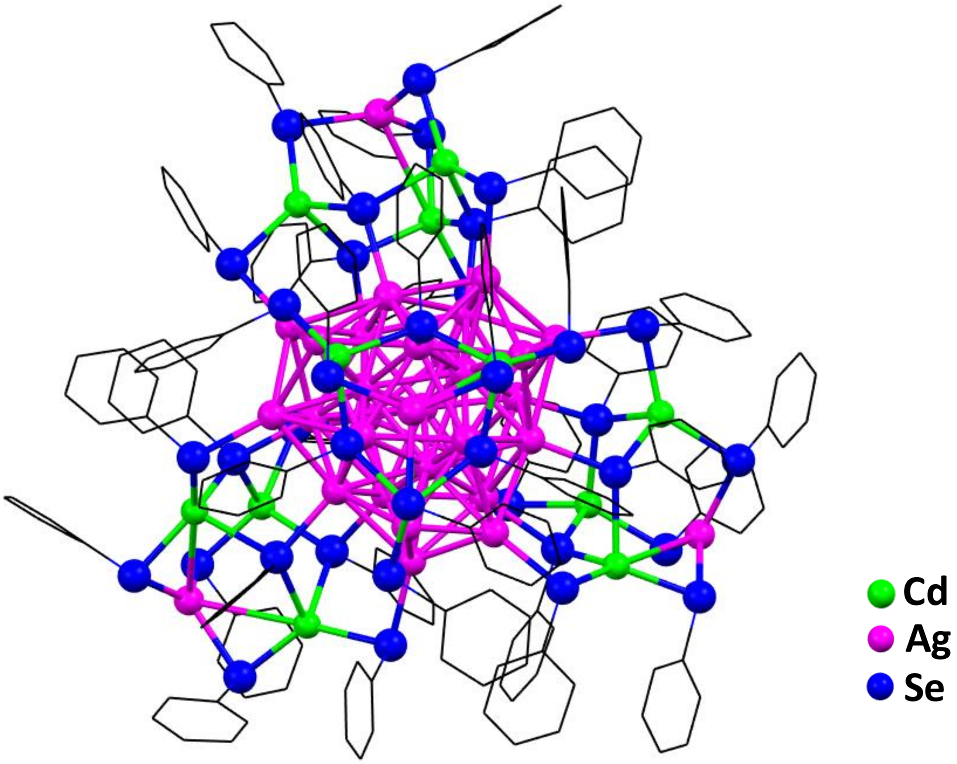

Figure 3.3 The total structure of $Cd_{12}Ag_{32}(SePh)_{36}$ cluster. H atoms of SePh ligands are omitted for clarity.

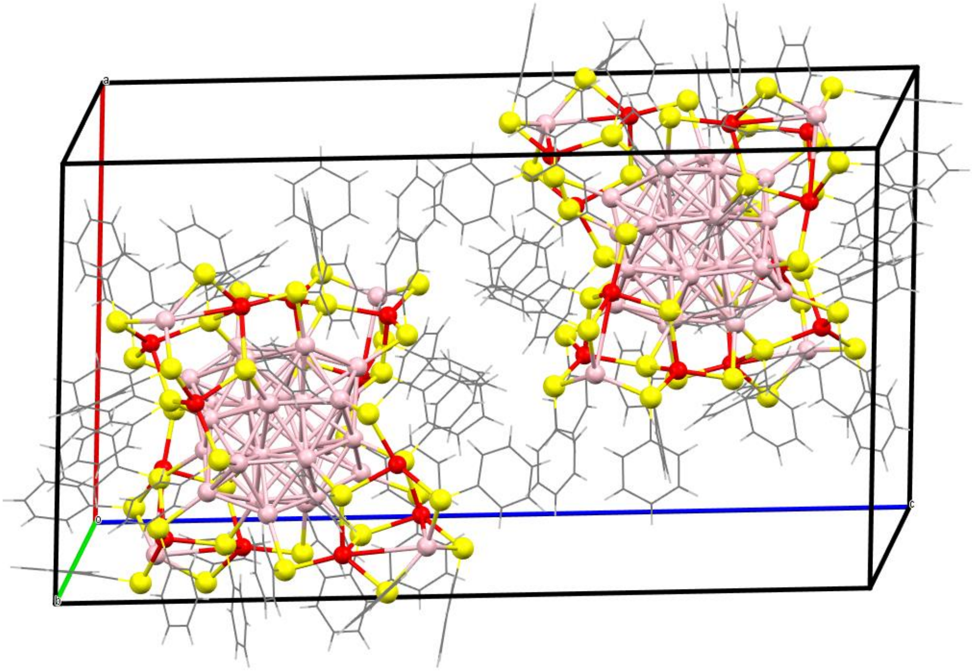

Figure 3.4 Packing of $Cd_{12}Ag_{32}(SePh)_{36}$ clusters in a unit cell, accommodating two clusters. Color legend: Cd, red; Ag, pink; Se: yellow; C, grey and H, light grey.

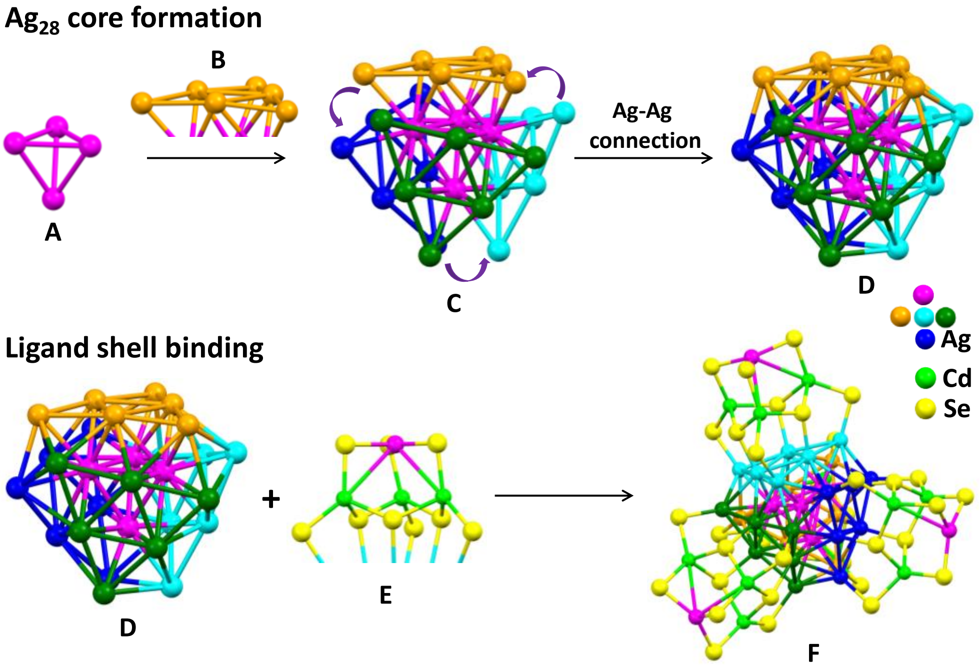

Figure 3.5 Construction of the structure of $Cd_{12}Ag_{32}(SePh)_{36}$. (A) Ag_4 inner core and (B) Ag_6 facet. Capping of Ag_4 core with Ag_6 facets and interfacet interactions (purple arrows) result in C and D, respectively. Mounting of $Cd_3Ag(SePh)_9$ motifs (E) on the Ag_{28} core (D) gives the total structure of the cluster (F). The phenyl rings of ligands are omitted for clarity.

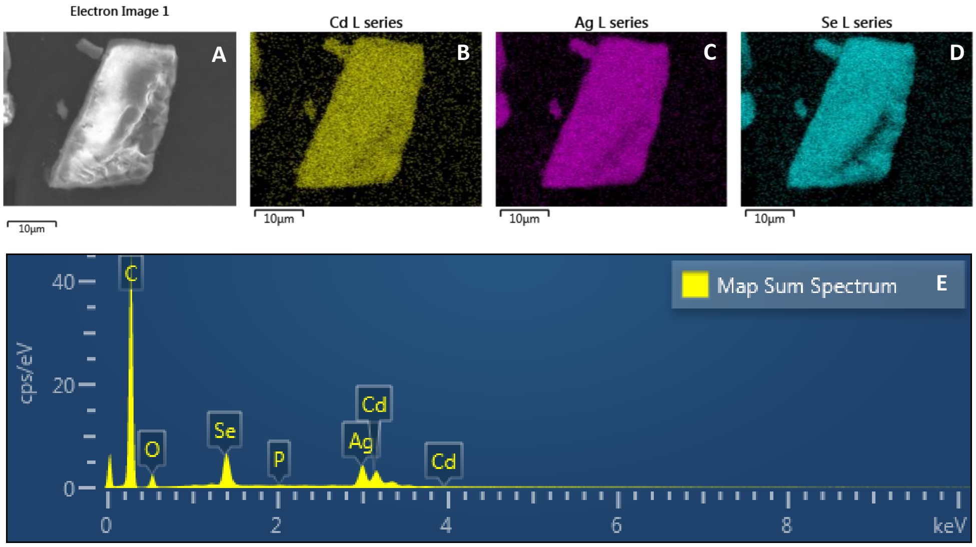

Figure 3.6 (A) SEM image of a small deformed single crystal of $Cd_{12}Ag_{32}(SePh)_{36}$ cluster. (B-D) are the elemental maps of Cd, Ag and Se, respectively. (E) EDS spectrum, confirming the presence of above elements in the cluster, which is consistent with the cluster composition obtained by SCXRD data.

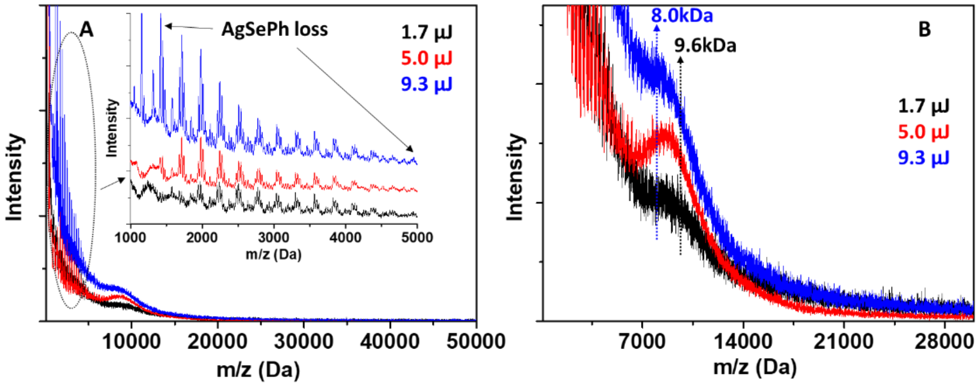

Figure 3.7 (A) Positive mode MALDI MS of $Cd_{12}Ag_{32}(SePh)_{36}$ cluster measured at different laser powers (1.7, 5.0 and 9.3 µJ). Inset of A, expanded view in the mass range of 1000-5000 Da, shows several peaks with a mass separation corresponding to AgSePh loss. This suggests that the cluster is fragile even at a threshold laser power of 1.7 µJ. (B) Expanded view of the spectra in A, showing a single peak for the cluster at ~9.6kDa at 1.7 µJ laser power, which upon shifted to ~8.0kDa by increasing the laser power to 9.3 µJ. Such laser-induced fragmentation is typical in the MALDI MS of silver clusters.

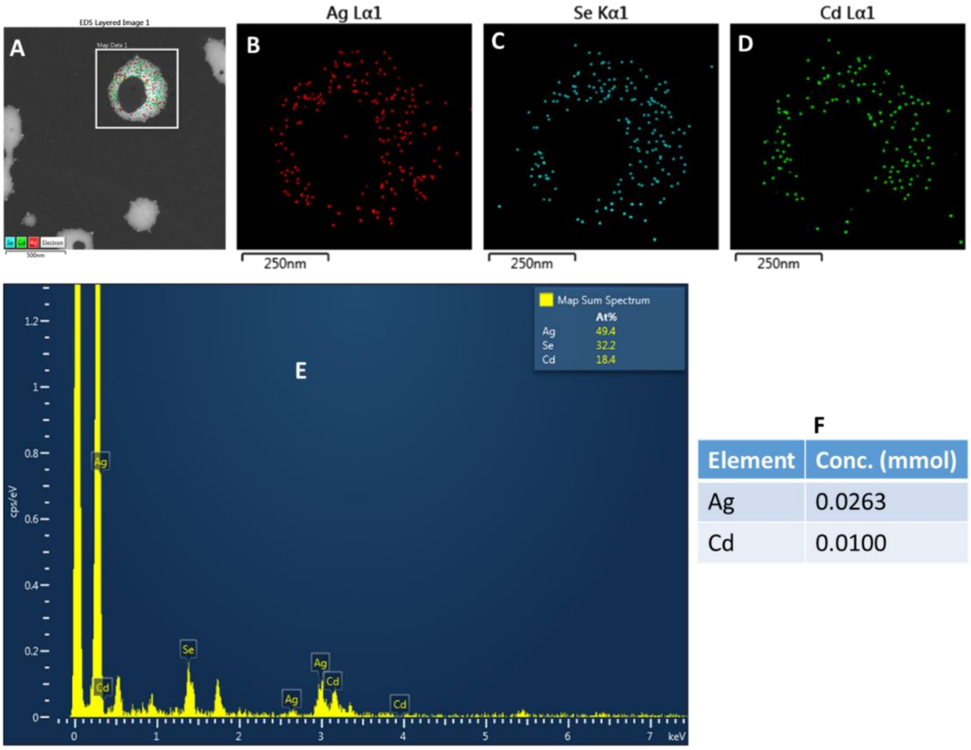

Element	Conc. (mmol)
Ag	0.0263
Cd	0.0100

Figure 3.8 (A) STEM image, (B-D) EDS elemental maps, (E) EDS spectrum and (F) ICP AES elemental analysis of single crystal sample of $Cd_{12}Ag_{32}(SePh)_{36}$ cluster. A close match of the Ag:Cd atomic ratio (2.66) in the $Cd_{12}Ag_{32}(SePh)_{36}$ cluster with that from STEM EDS and ICP AES (2.68 and 2.63, respectively) validates the metal composition of the cluster.

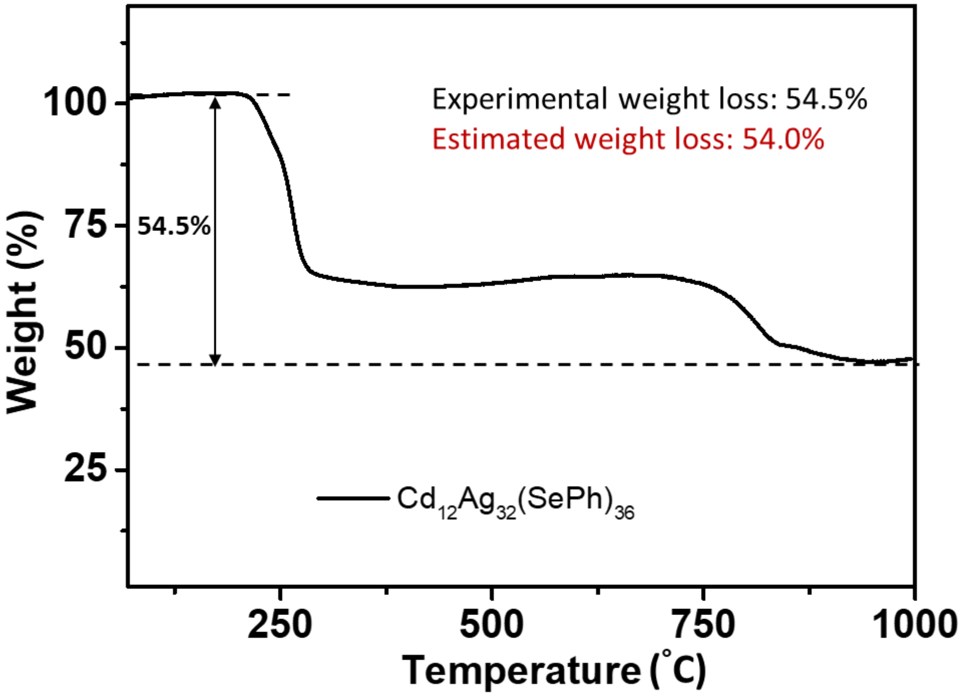

Figure 3.9 TGA curve of the single crystals of $Cd_{12}Ag_{32}(SePh)_{36}$ cluster, displaying a total weight loss of 54.5% in agreement with the estimated weight loss of 54.0% due to ligand dissociation.

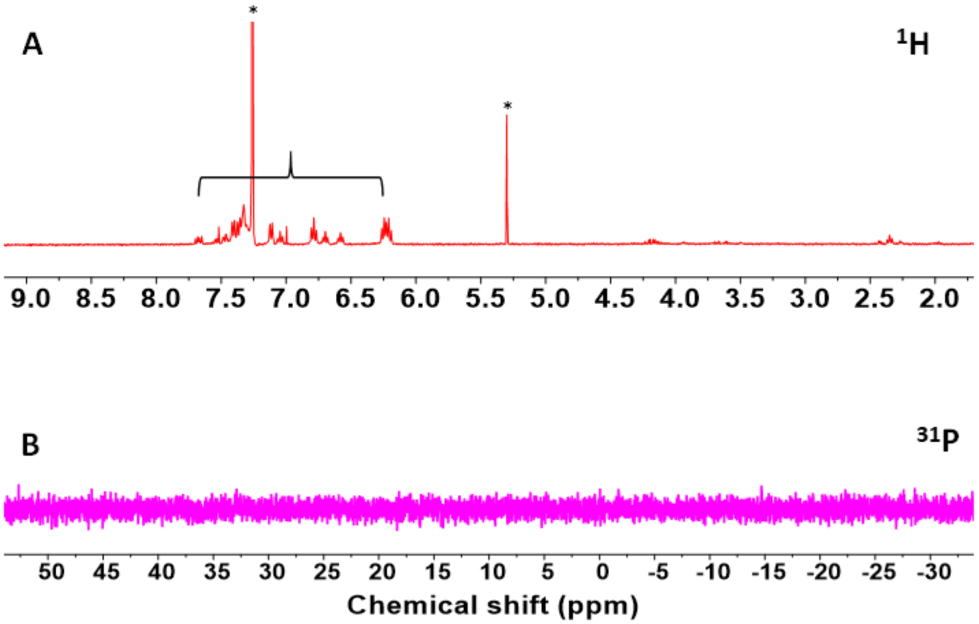

Figure 3.10 (A) ^{1}H and (B) ^{31}P NMR spectra of $CDCl_3$ solution of single crystals of $Cd_{12}Ag_{32}(SePh)_{36}$ clusters. Sharp single peaks labelled with asterisk (*) at 7.26 and 5.30 ppm are due to residual solvents $CHCl_3$ (from $CDCl_3$) and CH_2Cl_2 (from single crystals of cluster), respectively. The absence of ^{31}P signal in B and the presence of aromatic hydrogens (in between 6-8 ppm) from SePh of the clusters are in good agreement with the single crystal XRD results.

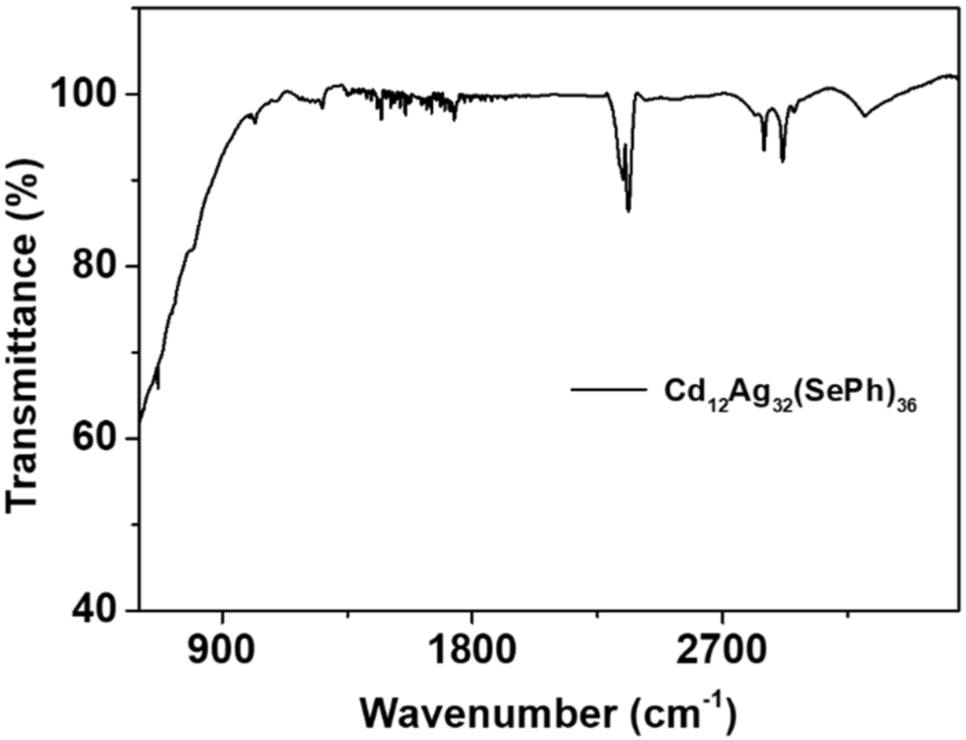

Figure 3.11 The FTIR spectrum of the $Cd_{12}Ag_{32}(SePh)_{36}$ cluster, showing aromatic C-H stretching frequencies around ~3000 cm^{-1} for SePh ligands.

Table 3.1 Crystal data and structure refinement of $Cd_{12}Ag_{32}(SePh)_{36}$ cluster.

Empirical formula	$\mathbf{C_{216}H_{180}Cd_{12}Ag_{32}Se_{36}}$
Formula weight	10418.79
Temperature/K	100.01(10)
Crystal system	triclinic
Space group	P-1
a/Å	19.2821(4)
b/Å	19.3677(4)
c/Å	34.7903(5)
α/°	88.3916(13)
β/°	86.2435(13)
γ/°	85.6543(15)
Volume/$Å^3$	12923.8(4)
Z	2
ρ_{calc} g/cm^3	2.677
μ/mm^{-1}	32.776
F(000)	9560.0
Crystal size/mm^3	0.05 × 0.05 × 0.01
Radiation	Cu Kα (λ = 1.54184 Å)
2Θ range for data collection/°	6.732 to 122.338
Index ranges	$-21 \leq h \leq 21$, $-22 \leq k \leq 20$, $-35 \leq l \leq 39$
Reflections collected	81562
Independent reflections	39636 [R_{int} = 0.0603, R_{sigma} = 0.0676]
Data/restraints/parameters	39636/1596/2617
Goodness-of-fit on F^2	1.077
Final R indexes [I>=2σ (I)]	R_1 = 0.0631, wR_2 = 0.1568
Final R indexes [all data]	R_1 = 0.0742, wR_2 = 0.1669
Largest diff. peak/hole / e $Å^{-3}$	4.17/-2.08

Table 3.2 List of bond lengths in $Cd_{12}Ag_{32}(SePh)_{36}$ clusters.

Bond type/Location	**Bond length range (Å)**	**Average length (Å)**
Ag-Ag/within Ag_4 inner core	2.834-2.863	2.8475
Ag-Ag/($Ag_{4\ \text{tetrahedron}}$-$Ag_{24\ \text{layer}}$)	2.673-3.156	2.8383
Ag-Ag/(within the $Ag_{24\ \text{layer}}$)	2.805-3.160	2.9562
Ag-Se/(Ag_{24} layer-Se)	2.575-2.640	2.6040
Ag-Se/(within the ligand motif)	2.571-2.638	2.6000
Ag-Cd/(within the ligand motif)	3.520-3.701	3.63
Cd-Se/(within the ligand motif)	2.565-2.734	2.6438

3.3.2. Characterization and theoretical calculation of $Cd_{12}Ag_{32}(SePh)_{36}$ cluster

The “superatom” theory[38] calculates a free metal electron count of 20 for $Cd_{12}Ag_{32}(SePh)_{36}$ cluster i.e., [(12x2)+(32x1)–(36x1)] by considering the *s*-valence of two for Cd and one for Ag as well as one-electron withdrawing character of the SePh ligand. This electron count predicts that the HOMO state and the molecular orbitals just below HOMO should have 1D-2S symmetries present in a spherical angular momentum analysis, and the LUMO state should have 1F character. This is indeed what we observe by performing symmetry analysis and inspecting visually the frontier orbitals (Figure 3.12, 3.13), although the HOMO has a mixed 2S-1F character probably due to the non-spherical symmetry of the metal core. Furthermore, atomic charge analysis (Table 3.3) shows that the Ag atoms in the Ag_4Ag_{24} shells are close to neutral, whereas the Ag and Cd atoms in the ligand motifs are clearly positively charged by 0.20 e and 0.66 e, respectively. The SePh ligands are shown as electron-withdrawing with a clear negative total charge by -0.28 e per ligand.

The optical properties and electronic structure of $Cd_{12}Ag_{32}(SePh)_{36}$ cluster were further studied both experimentally by UV-vis spectroscopy and theoretically by the linear response formulation of the time-dependent density functional theory (LR-TDDFT). The experimental absorption spectrum (Figure 3.14) displays clear peaks at 451, 534 and 640 nm along with shoulder peaks at 245, 288, 335, and 493 nm. The absorption onset (Figure 3.15) at ~900 nm (1.37 eV) is very close to the calculated HOMO-LUMO gap of 1.35 eV, with a slight underestimation of the gap being a typical feature of the used DFT PBE xc-functional. The calculated absorption spectrum for both the experimental (Figure 3.15) and PBE-relaxed cluster structure show a good agreement with the experiment, with at least six peaks/shoulders identifiable in the computed spectrum (labels a–f).

The absorption features a-f were analyzed by creating the dipole transition contribution maps and by breaking down the contributions by different parts of the cluster to a given transition (Figure 3.16). The lower energy peaks (a–c) have all similar characters, namely they are superatom-to-superatom transitions concentrated in the Ag core (intraband Ag(sp)→Ag(sp) transitions). It is interesting to note that the energy difference between a and b peaks seems to be a direct measure to the energy splitting of the superatom 1F manifold by the overall tetrahedral symmetry of the cluster (Figure 3.12). The high-energy features, d–f have increasing contributions also from the metal-ligand interface (mainly from Se(p)) and weakening contributions from the superatom states. We note that the Ag d-band is not actively participating to optical transitions in the analyzed and measured energy range, nor are the Cd atoms (since they are in the formal Cd(II) state). Interestingly, the $Cd_{12}Ag_{32}(SePh)_{36}$ cluster shows a broad NIR PL (quantum yield: ~0.28%) peak at ~1020 nm (Figure 3.15), which is different from the visible PL of Ag

NCs.[2] The similar PL excitation and UV-vis spectra, and the same emission at 1020 nm for different excitations together (Figure 3.17) indicate that the PL is originated from the cluster. The PL of Cd doped Ag cluster at 1020 nm is clearly different from that of a Cu doped cluster at 900 nm,[28] suggesting the successful tuning of NIR PL by the non-noble metal doping (Figure 3.18). Theoretically estimated PL emissions at 1134 nm and 1150 nm are in qualitative agreement with the experiment (1020 nm), strongly suggesting that the origin of the high-energy end of broad PL is the de-excitation over the HOMO-LUMO energy gap.[40] The low-energy end of PL is likely resulted from the relaxation through an intrinsic $Cd_3Ag(SePh)_9$ surface state.

The SCXRD shows that the two clusters in the unit cell are enantiomers (Figure 3.19) due to asymmetric Ag_{28} core. Since the solution of $Cd_{12}Ag_{32}(SePh)_{36}$ is racemic, we cannot experimentally measure the chiral optical response, however, it can be straightforwardly calculated for one of the enantiomers. Our calculations predict that the strength of the chiral response in the UV-vis region (Figure 3.20) is comparable to, e.g., the well-known thiolated chiral $Au_{38}(SR)_{24}$ cluster.[41,42]

We note the absence of PPh_3 in $Cd_{12}Ag_{32}(SePh)_{36}$ cluster (Figure 1), which could be synthesized only in the presence of PPh_3 and tetraoctylammonium bromide (Figure 3.21) in our experimental conditions. The absorption spectra (Figure 3.22) suggest that the formation of $Cd_{12}Ag_{32}(SePh)_{36}$ proceeds through the intermediate clusters formed after $NaBH_4$ reduction of metal-ligand complexes. The ^{31}P and ^{1}H NMR spectra confirm the binding of PPh_3 in the metal-ligand complexes (Figure 3.23, 3.24). After $NaBH_4$ addition, the PPh_3 in the complex transfers the metals to form intermediates and subsequently released into solution, confirming PPh_3-mediated synthesis of the $Cd_{12}Ag_{32}(SePh)_{36}$ cluster. This cluster shows moderate and excellent ambient stability in the solution- and solid-state, respectively (Figure 3.25).

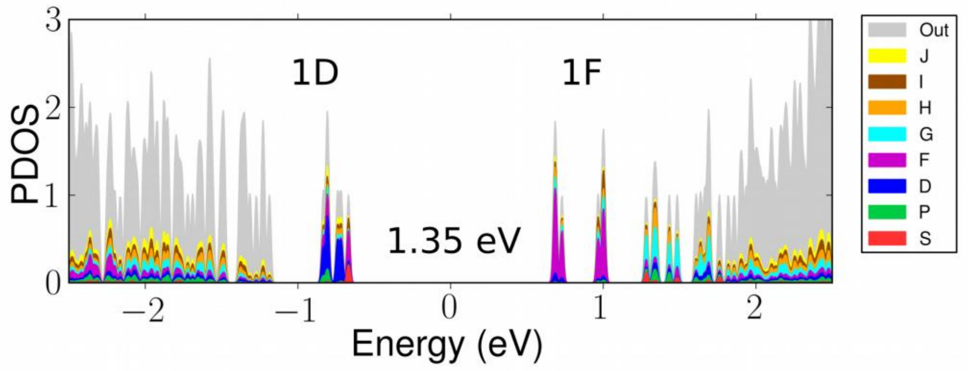

Figure 3.12 Y_{lm}-analysis of electronic states of $Cd_{12}Ag_{32}(SePh)_{36}$ cluster using the experimental crystal structure. The projection is with respect to spherical harmonics around center of mass of the cluster. The central energy gap around zero (1.35 eV) is the HOMO-LUMO gap. The manifold of the states around the HOMO-LUMO gap shows symmetries of 1D (blue peaks), a mixed 2S-1F HOMO (red-purple peak), and 1F LUMO (purple), as labeled, consistent with 20 free metal electrons in the cluster as deduced from the superatom theory.[38]

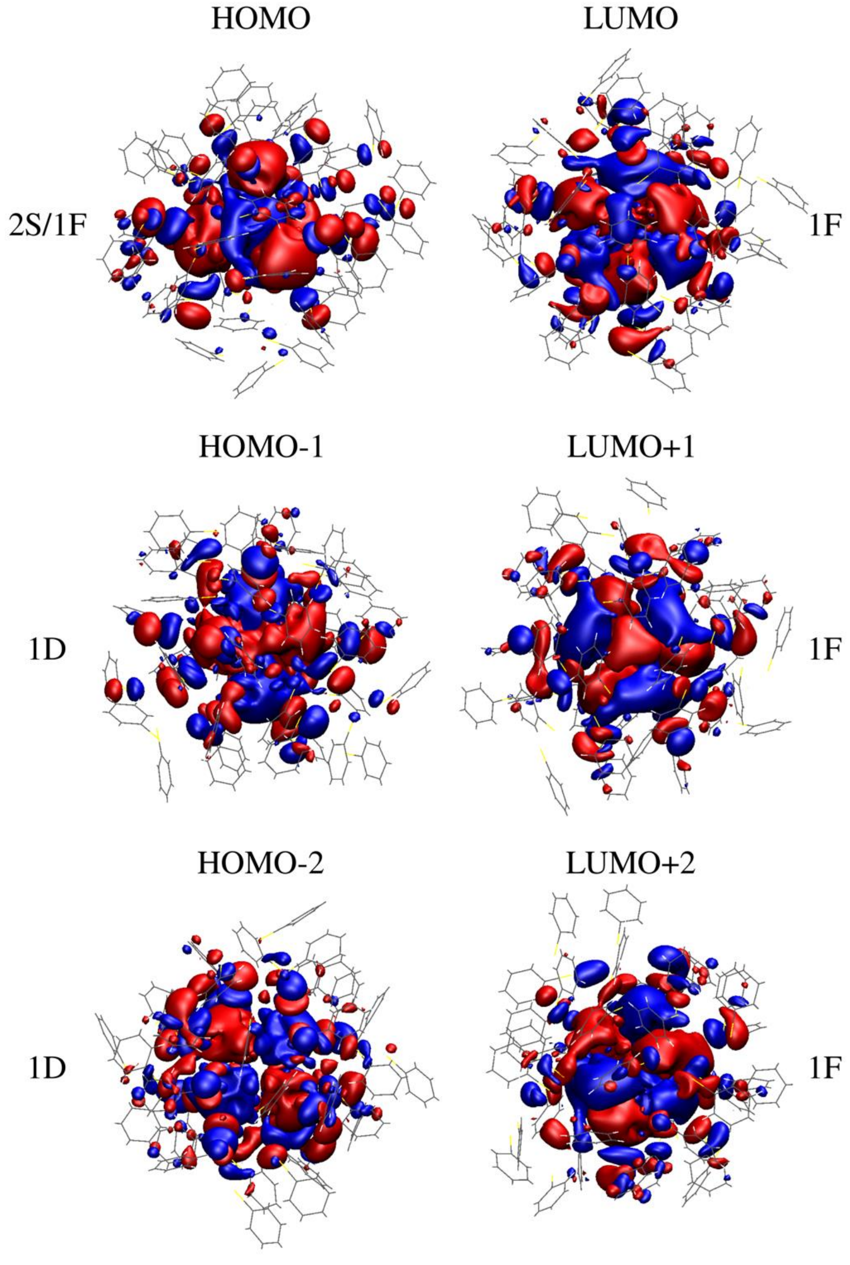

Figure 3.13 Visualization of selected frontier orbitals of $Cd_{12}Ag_{32}(SePh)_{36}$ along with the spherical symmetry notation (cf. Figure 3.12).

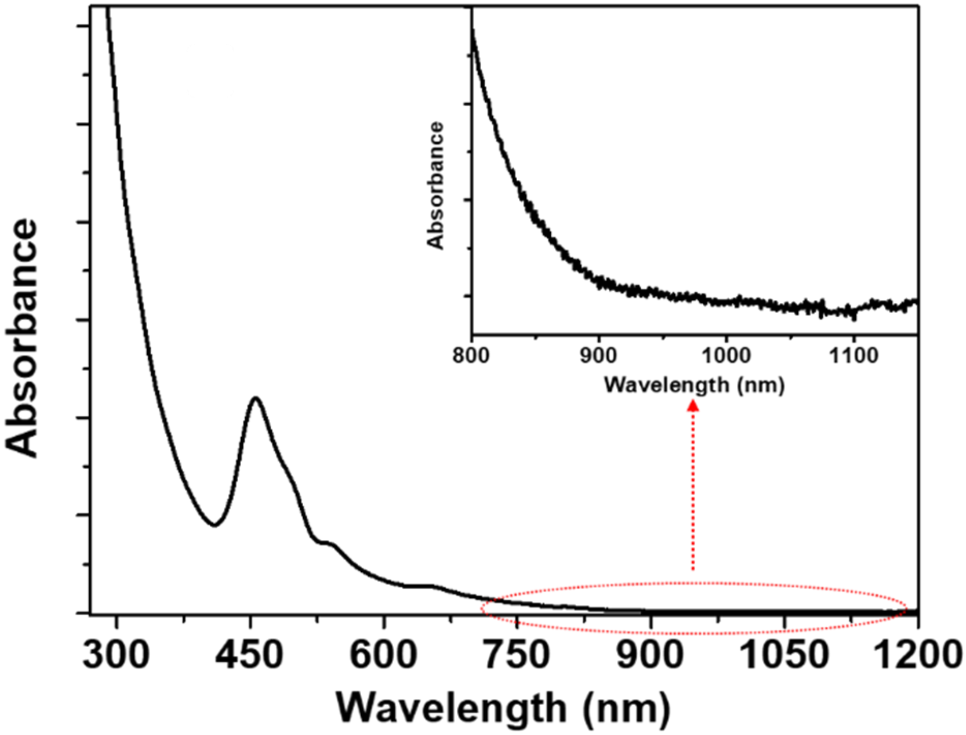

Figure 3.14 UV-vis absorption spectrum of $Cd_{12}Ag_{32}(SePh)_{36}$ cluster. Inset of B shows the absorption onset around 900 nm.

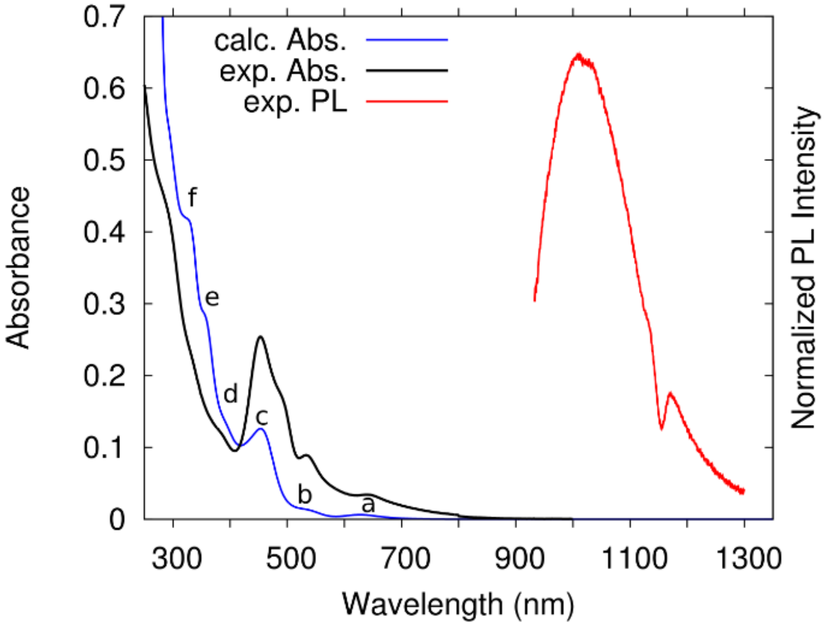

Figure 3.15 Experimental (black) and calculated (blue) absorption spectra of $Cd_{12}Ag_{32}(SePh)_{36}$ cluster. For easier comparison, the calculated spectrum is blue-shifted uniformly by 0.3 eV. Red line: experimental PL (excitation: 490 nm).

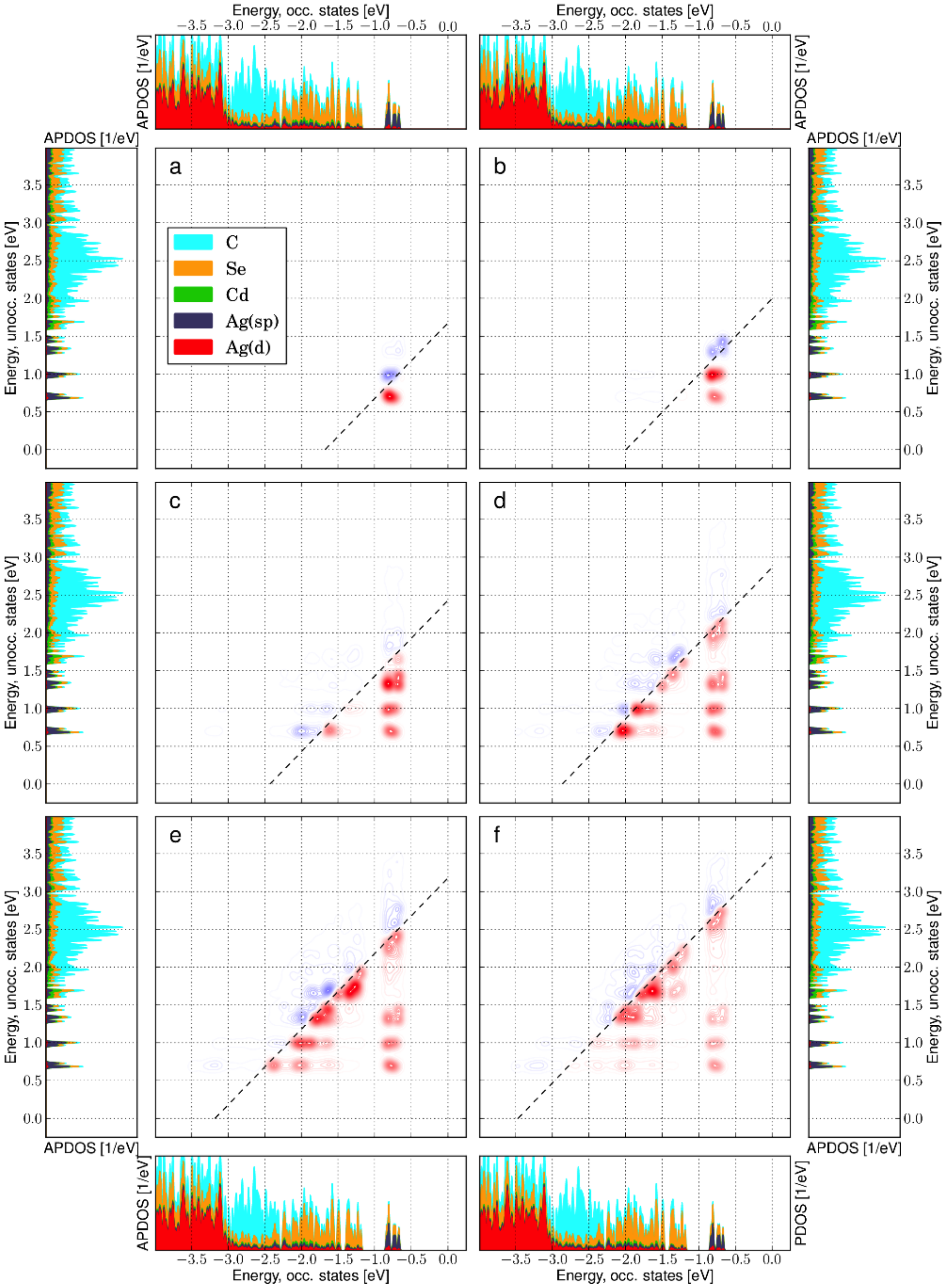
a
b
c
d
e
f
C
Se
Cd
Ag(sp)
Ag(d)
Energy, occ. states [eV]
−3.5 −3.0 −2.5 −2.0 −1.5 −1.0 −0.5 0.0
Energy, unocc. states [eV]
0.0 0.5 1.0 1.5 2.0 2.5 3.0 3.5
APDOS [1/eV]
PDOS [1/eV]

Figure 3.16 Dipole transition contribution map (DTCM) analysis of the six lowest-energy linear absorption peaks/shoulders of $Cd_{12}Ag_{32}(SePh)_{36}$ computed by using the experimental crystal structure. Labels a–f correspond directly to labels a–f in the computed spectrum in Figure 3.15. The electron states are formed in the manifold of the initially unoccupied states (leftmost and rightmost panels) and the hole states are formed in the manifold of the initially occupied states (topmost and bottom-most panels). The occupied – unoccupied electron densities of states (DOS) are presented as a projection to atomic components (atom-projected DOS, APDOS) as shown by the labels in panel a. Red/blue contributions denote constructive/destructive contribution to the transition dipole, respectively. The brightness of the red/blue spots scales with the magnitude of contribution. The dashed diagonal lines denote the electron-hole (e-h) energy equaling the peak position, *i.e.*, $\varepsilon_e - \varepsilon_h = hc / \lambda$. The Fermi energy is at zero.

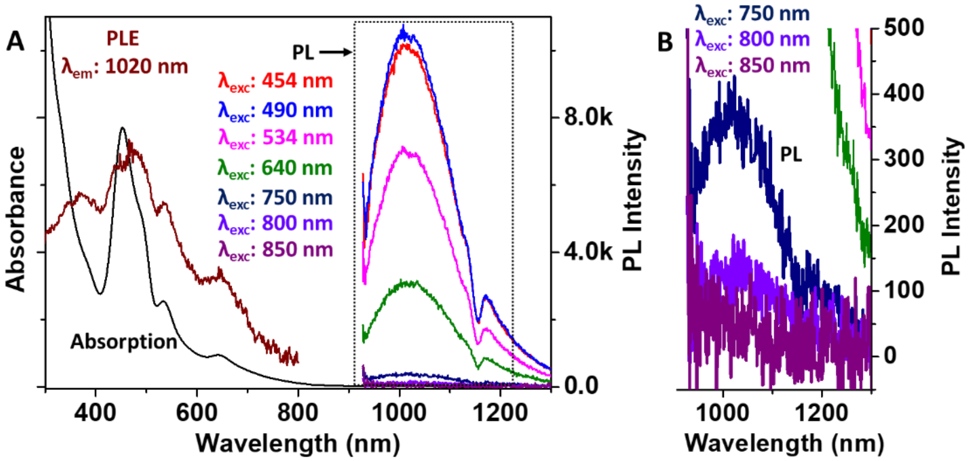

Figure 3.17 (A) UV-vis absorption, PL excitation (PLE) and PL emission spectra of $Cd_{12}Ag_{32}(SePh)_{36}$ cluster in DCM. (B) An expanded view of the PL spectra (λ_{exc}: 750, 800 and 850 nm) in A, showing the appearance of PL even at an excitation at 800 nm.

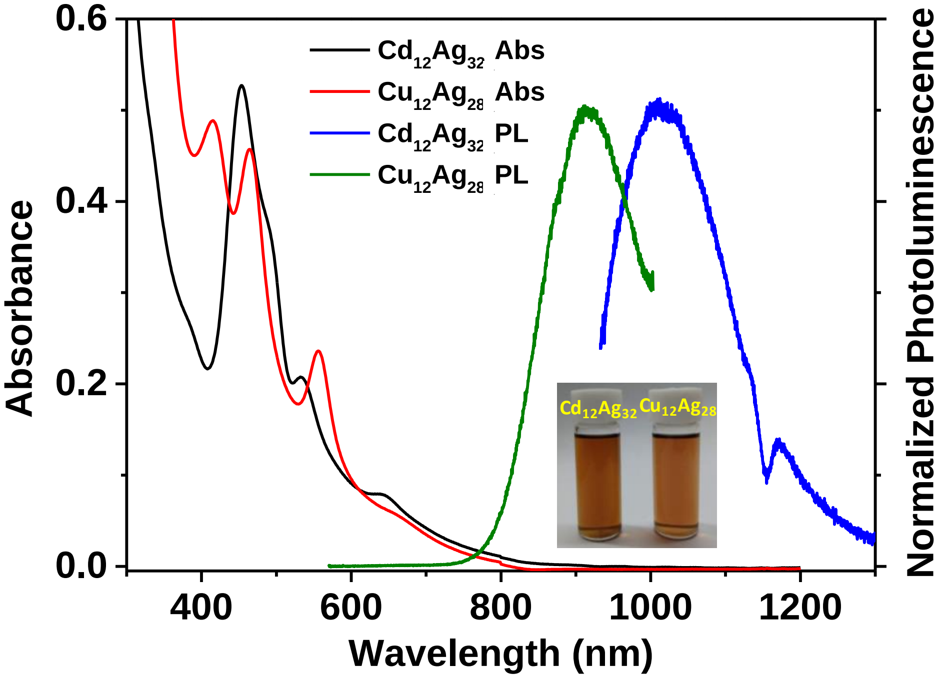

Figure 3.18 Comparison of the UV-vis absorption and PL emission spectra of $Cd_{12}Ag_{32}(SePh)_{36}$ and $[Cu_{12}Ag_{28}(2,4\text{-}DCBT)_{24}]^{4-}$ clusters in DCM. Inset: DCM solutions of above clusters, appearing nearly the same.

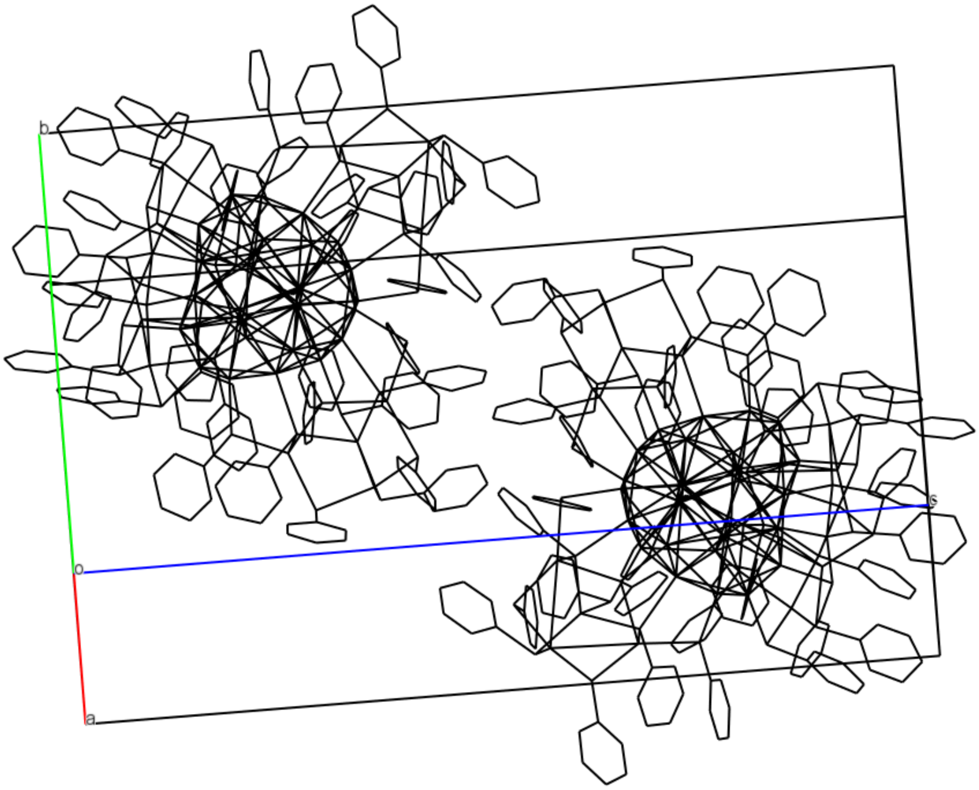

Figure 3.19 The crystal structure of $Cd_{12}Ag_{32}(SePh)_{36}$ cluster, in which the unit cell comprises a pair of enantiomers.

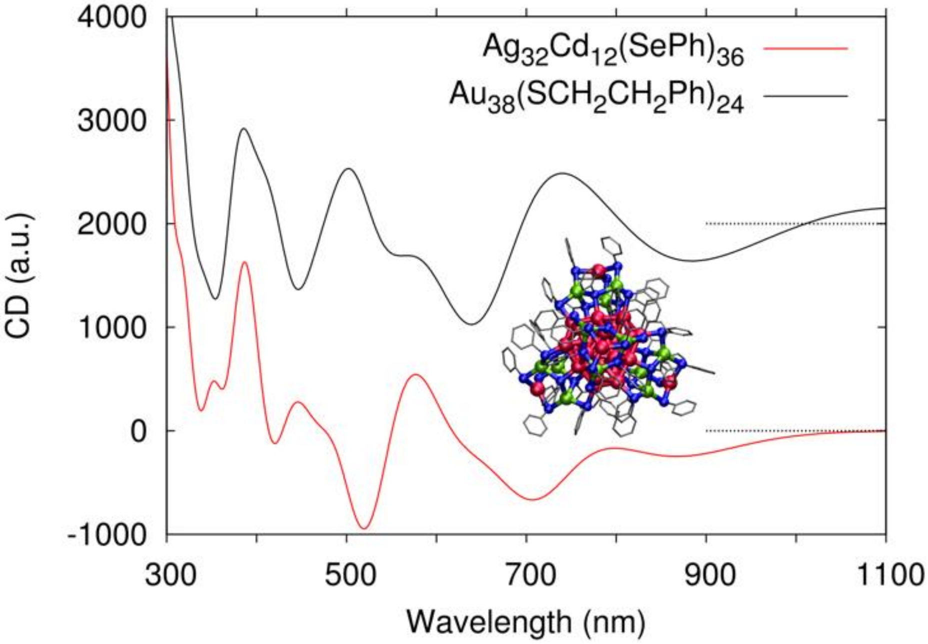

Figure 3.20 Computed circular dichroism (CD) spectra of one of the enantiomers of $Cd_{12}Ag_{32}(SePh)_{36}$ (red curve) and $Au_{38}(SCH_2CH_2Ph)_{24}$ (black curve, offset vertically for better visualization) clusters. Inset: the DFT optimized structure of the $Cd_{12}Ag_{32}(SePh)_{36}$ enantiomer.

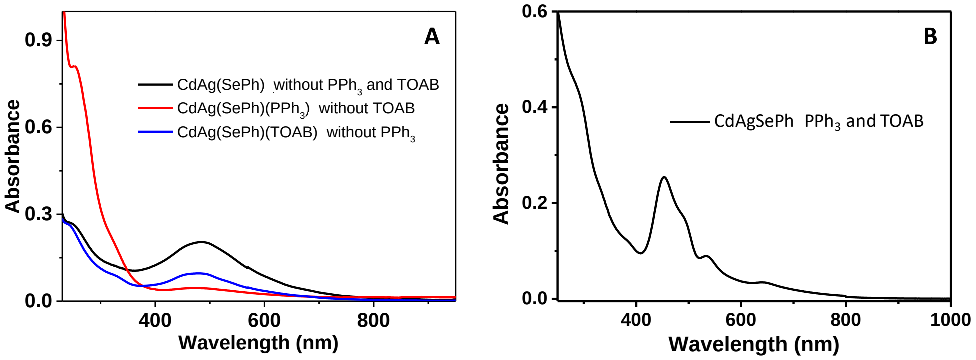

Figure 3.21 (A and B) UV-vis absorption spectra of the final products synthesized under various conditions. These data clearly indicate the synthesis of $Cd_{12}Ag_{32}(SePh)_{36}$ clusters needs both TOAB and PPh_3.

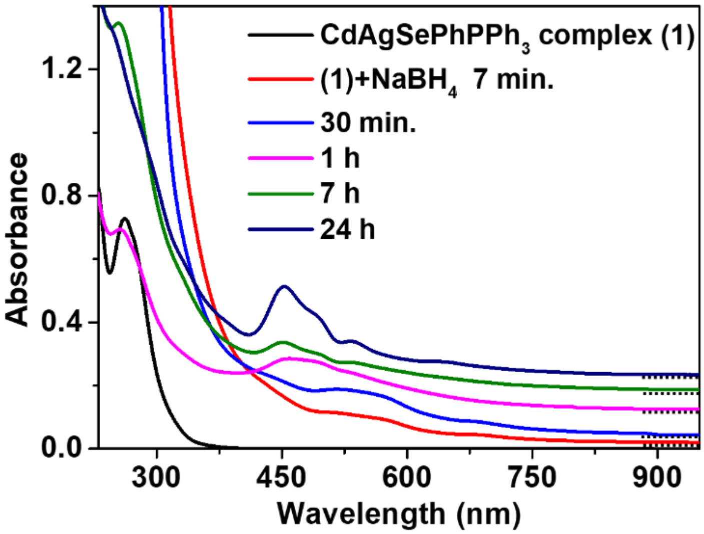

Figure 3.22 The UV-vis absorption spectra of the solutions recorded at different times during the synthesis of $Cd_{12}Ag_{32}(SePh)_{36}$ cluster.

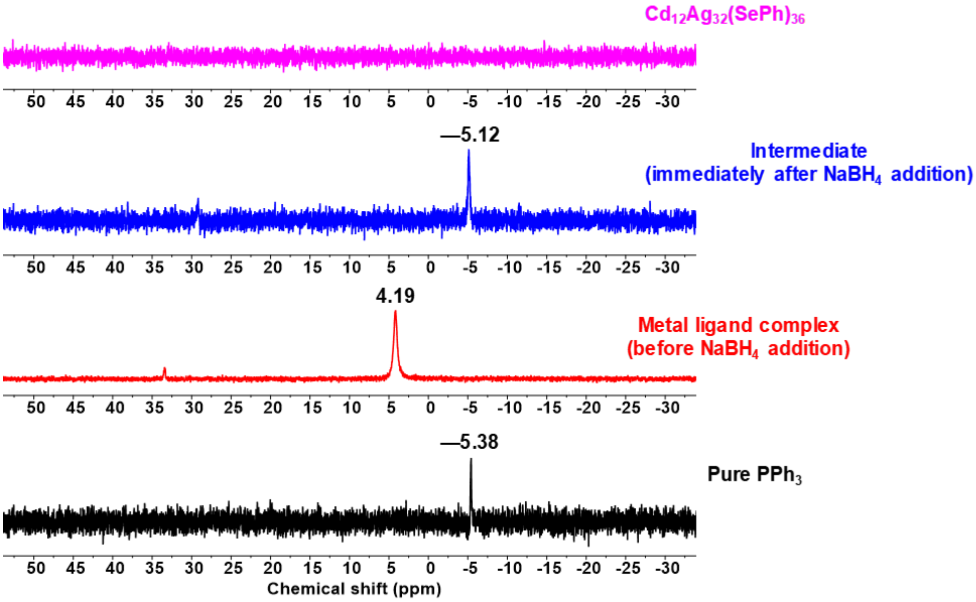

Figure 3.23 ^{31}P NMR spectra of PPh_3, colorless metal ligand complexes (before $NaBH_4$ reduction), intermediates (formed immediately after $NaBH_4$ reduction) and pure $Cd_{12}Ag_{32}(SePh)_{36}$ clusters. The release of PPh_3 from the metal ligand complex after adding $NaBH_4$ is identified by the disappearance of ^{31}P peak at 4.19 ppm and its appearance at -5.12 ppm. This indicates the simultaneous metal transfer from the complex to form intermediates and the release of PPh_3 into solution.

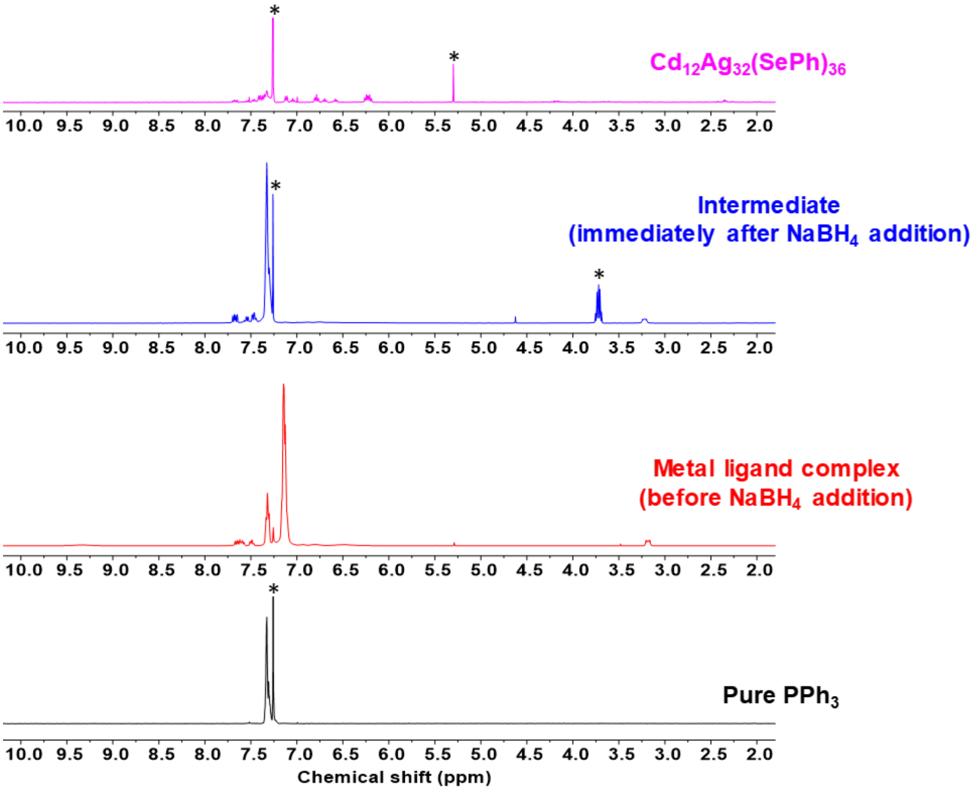

Figure 3.24 ^{1}H NMR spectra of PPh_3, colorless metal ligand complexes (before $NaBH_4$ reduction), intermediates (formed immediately after $NaBH_4$ reduction) and pure $Cd_{12}Ag_{32}(SePh)_{36}$ clusters. After $NaBH_4$ reduction, the release of PPh_3 ligands into solution from metal ligand complex is consistent with ^{31}P NMR results. Sharp single peaks labelled with asterisk (*) at 7.26 and 5.30 ppm are due to residual solvents $CHCl_3$ (from $CDCl_3$) and CH_2Cl_2 (from the reaction), respectively.

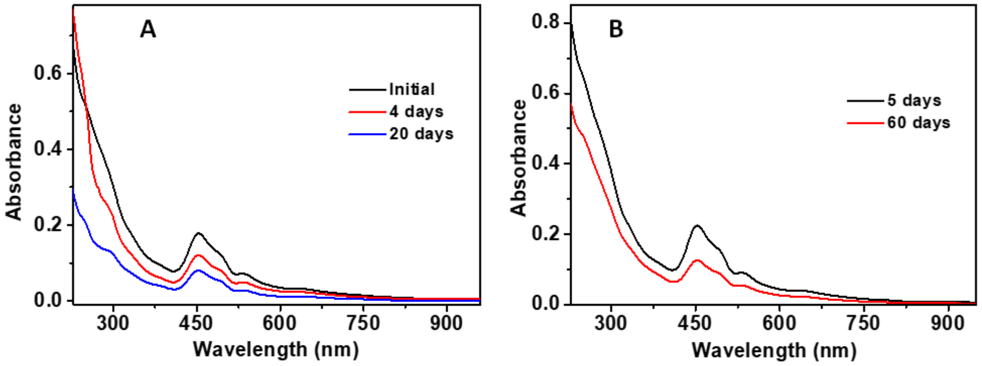

Figure 3.25 Monitoring the ambient stability of $Cd_{12}Ag_{32}(SePh)_{36}$ clusters in (A) solution and (B) solid state using UV-vis spectroscopy. The spectra in B were acquired by dissolving the same cluster powder in DCM at desired time. Only a slight decrease in absorbance of cluster in solution state (A) suggests the moderate stability of cluster in the solution, while it is highly stable as a solid.

Table 3.3 Shell-by-shell atomic charges from the Bader analysis for $Cd_{12}Ag_{32}(SePh)_{36}$ cluster in the experimental crystal structure.

Atomic layers	**Number of atoms/ligands**	**Total charge Q [|e|]**	**Q/N [|e|]**
1: Ag_4 (inner core)	4	-0.130	-0.033
2: Ag_{24} (outer core)	24	1.630	0.068
3: Ag_4 (motifs)	4	0.804	0.201
4: Cd_{12} (motifs)	12	7.899	0.658
5: Se (motifs)	36	-5.953	-0.165
6: C,H in Ph (motifs)	36	-4.265	-0.118

3.4 Conclusion

In summary, we designed a phosphine-assisted synthetic strategy to dope an atomically precise Ag nanocluster with a non-noble metal, Cd. By this method, we synthesized a single-sized neutral $Cd_{12}Ag_{32}(SePh)_{36}$ cluster and elucidated its total structure using X-ray crystallography. The Cd dopant is found to prefer the cluster surface to its core. Our cluster exhibits NIR PL and a chiral core, resulting optical activity. The absorption spectrum and electronic structure of this cluster are well compared with those from the DFT. Our ligand-assisted synthesis of nanocluster may become a general method to introduce other active metals into noble metal clusters.

** Studies on this part written based on the work conducted with Megalamane Siddarappa Bootharaju (Co-first author) which was reported on *Journal of the American Chemical Society*. (*J. Am. Chem. Soc.* **2019**, *141*, 8422–8425.)

3.5 Reference

[1] Jin, R.; Zeng, C.; Zhou, M.; Chen, Y. Atomically precise colloidal metal nanoclusters and nanoparticles: fundamentals and opportunities. *Chem. Rev.* **2016**, *116*, 10346–10413.

[2] Chakraborty, I.; Pradeep, T. Atomically precise clusters of noble metals: emerging link between atoms and nanoparticles. *Chem. Rev.* **2017**, *117*, 8208.

[3] Yan, J.; Teo, B. K.; Zheng, N. Surface chemistry of atomically precise coinage–metal nanoclusters: from structural control to surface reactivity and catalysis. *Acc. Chem. Res.* **2018**, *51*, 3084–3093.

[4] Liu, Y.; Chai, X.; Cai, X.; Chen, M.; Jin, R.; Ding, W.; Zhu, Y. Central doping of a foreign atom into the silver cluster for catalytic conversion of CO_2 toward C−C bond formation. *Angew. Chem. Int. Ed.* **2018**, *57*, 9775–9779.

[5] Sakthivel, N. A.; Dass, A. Aromatic thiolate-protected series of gold nanomolecules and a contrary structural trend in size evolution. *Acc. Chem. Res.* **2018**, *51*, 1774–1783.

[6] Tang, Q.; Hu, G.; Fung, V.; Jiang, D.-e., Insights into interfaces, stability, electronic properties, and catalytic activities of atomically precise metal nanoclusters from first principles. *Acc. Chem. Res.* **2018**, 51, 2793–2802.

[7] Bhattarai, B.; Zaker, Y.; Atnagulov, A.; Yoon, B.; Landman, U.; Bigioni, T. P. Chemistry and Structure of Silver Molecular Nanoparticles. *Acc. Chem. Res.* **2018**, *51*, 3104–3113.

[8] Wang, Z.; Su, H. F.; Tung, C. H.; Sun, D.; Zheng, L. S. Deciphering synergetic core-shell transformation from [Mo_6O_{22}@Ag_{44}] to [Mo_8O_{28}@Ag_{50}]. *Nat. Commun.* **2018**, *9*, 4407.

[9] Jadzinsky, P. D.; Calero, G.; Ackerson, C. J.; Bushnell, D. A.; Kornberg, R. D. Structure of a thiol monolayer-protected gold nanoparticle at 1.1 Å resolution. *Science* **2007**, *318*, 430–433.

[10] Conn, B. E.; Atnagulov, A.; Yoon, B.; Barnett, R. N.; Landman, U.; Bigioni, T. P. Confirmation of a de novo structure prediction for an atomically precise monolayer-coated silver nanoparticle. *Sci. Adv.* **2016**, *2*, e1601609.

[11] Bootharaju, M. S.; Burlakov, V. M.; Besong, T. M. D.; Joshi, C. P.; AbdulHalim, L. G.; Black, D. M.; Whetten, R. L.; Goriely, A.; Bakr, O. M. Reversible size control of silver nanoclusters via ligand-exchange. *Chem. Mater.* **2015**, *27*, 4289–4297.

[12] Song, Y.; Zhong, J.; Yang, S.; Wang, S.; Cao, T.; Zhang, J.; Li, P.; Hu, D.; Pei, Y.; Zhu, M. Crystal structure of $Au_{25}(SePh)_{18}$ nanoclusters and insights into their electronic, optical and catalytic properties. *Nanoscale* **2014**, *6*, 13977–13985.

[13] Lei, Z.; Wan, X. K.; Yuan, S. F.; Guan, Z. J.; Wang, Q. M. Alkynyl approach toward the protection of metal nanoclusters. *Acc. Chem. Res.* **2018**, *51*, 2465–2474.

[14] Zhang, S. S.; Alkan, F.; Su, H. F.; Aikens, C. M.; Tung, C. H.; Sun, D. [$Ag_{48}(C\equiv C^tBu)_{20}(CrO_4)_7$]: an atomically precise silver nanocluster co-

protected by inorganic and organic ligands. *J. Am. Chem. Soc.* **2019**, *141*, 4460–4467.

[15] Qu, M.; Li, H.; Xie, L. H.; Yan, S. T.; Li, J. R.; Wang, J. H.; Wei, C. Y.; Wu, Y. W.; Zhang, X. M. Bidentate phosphine-assisted synthesis of an all-alkynyl-protected Ag_{74} nanocluster. *J. Am. Chem. Soc.* **2017**, *139*, 12346–12349.

[16] Shichibu, Y.; Negishi, Y.; Watanabe, T.; Chaki, N. K.; Kawaguchi, H.; Tsukuda, T. Biicosahedral gold clusters $[Au_{25}(PPh_3)_{10}(SC_nH_{2n+1})_5Cl_2]^{2+}$ (n = 2−18): a stepping stone to cluster-assembled materials. *J. Phys. Chem. C* **2007**, *111*, 7845–7847.

[17] Dhayal, R. S.; van Zyl, W. E.; Liu, C. W. Polyhydrido copper clusters: synthetic advances, structural diversity, and nanocluster-to-nanoparticle conversion. *Acc. Chem. Res.* **2016**, *49*, 86–95.

[18] Chakraborty, I.; Kurashige, W.; Kanehira, K.; Gell, L.; Häkkinen, H.; Negishi, Y.; Pradeep, T. $Ag_{44}(SeR)_{30}$: a hollow cage silver cluster with selenolate protection. *J. Phys. Chem. Lett.* **2013**, *4*, 3351–3355.

[19] Fuhr, O.; Dehnen, S.; Fenske, D. Chalcogenide clusters of copper and silver from silylated chalcogenide sources. *Chem. Soc. Rev.* **2013**, *42*, 1871.

[20] Ghosh, A.; Mohammed, O. F.; Bakr, O. M. Atomic-level doping of metal clusters. *Acc. Chem. Res.* **2018**, *51*, 3094–3103.

[21] Yang, J.; Muckel, F.; Baek, W.; Fainblat, R.; Chang, H.; Bacher, G.; Hyeon, T. Chemical synthesis, doping, and transformation of magic-sized semiconductor alloy nanoclusters. *J. Am. Chem. Soc.* **2017**, *139*, 6761–6770.

[22] Hossain, S.; Ono, T.; Yoshioka, M.; Hu, G.; Hosoi, M.; Chen, Z.; Nair, L. V.; Niihori, Y.; Kurashige, W.; Jiang, D.-e.; Negishi, Y. Thiolate-protected trimetallic $Au_{\sim 20}Ag_{\sim 4}Pd$ and $Au_{\sim 20}Ag_{\sim 4}Pt$ alloy clusters with controlled chemical composition and metal positions. *J. Phys. Chem. Lett.* **2018**, *9*, 2590–2594.

[23] Yuan, X.; Dou, X.; Zheng, K.; Xie, J. Recent advances in the synthesis and applications of ultrasmall bimetallic nanoclusters. *Part. Part. Syst. Charact.* **2015**, *32*, 613–629.

[24] Wang, S.; Song, Y.; Jin, S.; Liu, X.; Zhang, J.; Pei, Y.; Meng, X.; Chen, M.; Li, P.; Zhu, M. Metal exchange method using Au_{25} nanoclusters as templates for alloy nanoclusters with atomic precision. *J. Am. Chem. Soc.* **2015**, *137*, 4018–4021.

[25] Zhu, M.; Wang, P.; Yan, N.; Chai, X.; He, L.; Zhao, Y.; Xia, N.; Yao, C.; Li, J.; Deng, H.; Zhu, Y.; Pei, Y.; Wu, Z. The fourth alloying mode by way of anti-galvanic reaction. *Angew. Chem. Int. Ed.* **2018**, *57*, 4500–4504.

[26] Yang, S.; Chen, S.; Xiong, L.; Liu, C.; Yu, H.; Wang, S.; Rosi, N. L.; Pei, Y.; Zhu, M. Total structure determination of $Au_{16}(S\text{-}Adm)_{12}$ and $Cd_1Au_{14}(S^tBu)_{12}$ and implications for the structure of $Au_{15}(SR)_{13}$. *J. Am. Chem. Soc.* **2018**, *140*, 10988–10994.

[27] Yao, C.; Lin, Y. J.; Yuan, J.; Liao, L.; Zhu, M.; Weng, L. h.; Yang, J.; Wu, Z. Mono-cadmium vs mono-mercury doping of Au_{25} nanoclusters. *J. Am. Chem. Soc.* **2015**, *137*, 15350–15353.

[28] Yan, J.; Su, H.; Yang, H.; Hu, C.; Malola, S.; Lin, S.; Teo, B. K.; Häkkinen, H.; Zheng, N. Asymmetric synthesis of chiral bimetallic $[Ag_{28}Cu_{12}(SR)_{24}]^{4-}$ nanoclusters via ion pairing. *J. Am. Chem. Soc.* **2016**, *138*, 12751–12754.

[29] Bakr, O. M.; Amendola, V.; Aikens, C. M.; Wenseleers, W.; Li, R.; Dal Negro, L.; Schatz, G. C.; Stellacci, F. Silver nanoparticles with broad multiband linear optical absorption. *Angew. Chem. Int. Ed.* **2009**, *48*, 5921–5926.

[30] CrysAlisPro Version 1.171.35.19. Agilent Technologies Inc. Santa Clara, CA, USA, **2011**.

[31] Sheldrick, G. M. SHELXT - Integrated space-group and crystal-structure determination. *Acta Cryst*. **2015**, *C71*, 3–8.

[32] Sheldrick, G. M. A short history of SHELX. *Acta Cryst.* **2008**, *A64*, 112–122.

[33] Dolomanov, O. V.; Bourhis, L. J.; Gildea, R. J.; Howard, J. A. K.; Puschmann, H. OLEX2: a complete structure solution, refinement and analysis program. *J. Appl. Cryst*. **2009**, *42*, 339–341.

[34] Enkovaara, J.; Rostgaard, C.; Mortensen, J.J.; Chen, J.; Dulak, M.; Ferrighi, L.; Gavnholt, J.; Glinsvad, C.; Haikola, V.; Hansen, H.A. *et al.*

Electronic structure calculations with GPAW: a real-space implementation of the projector augmented-wave method. *J. Phys.: Condens. Matter* **2010**, *22*, 253202.

[35] Perdew, J. P.; Burke, K.; Ernzerhof, M. Generalized gradient approximation made simple. *Phys. Rev. Lett.* **1996,** *77*, 3865–3868.

[36] Walter, M.; Häkkinen, H.; Lehtovaara, L.; Puska, M.; Enkovaara, J.; Rostgaard, C.; Mortensen, J.J. Time-dependent density-functional theory in the projector augmented-wave method. *J. Chem. Phys.* **2008**, *128*, 244101.

[37] Malola, S.; Lehtovaara, L.; Enkovaara, J.; Häkkinen, H. Birth of the localized surface plasmon resonance in monolayer-protected gold nanoclusters. *ACS Nano* **2013**, *7*, 10263–10270.

[38] Walter, M.; Akola, J.; Lopez-Acevedo, O; Jadzinsky, P.D.; Calero, G.; Ackerson, C.J.; Whetten, R.L.; Grönbeck, H.; Häkkinen, H. A unified view of ligand-protected gold clusters as superatom complexes. *Proc. Natl. Acad. Sci. U. S. A.* **2008,** *105*, 9157–9162.

[39] Henkelman, G.; Arnaldsson, A.; Jónsson, H. A fast and robust algorithm for Bader decomposition of charge density. *Comp. Mater. Sci.* **2006**, *36*, 354–360.

[40] Aikens, C. M. Electronic and Geometric Structure, Optical Properties, and Excited State Behavior in Atomically Precise Thiolate-Stabilized Noble Metal Nanoclusters. *Acc. Chem. Res.* **2018,** *51*, 3065–3073.

[41] Lopez-Acevedo, O.; Tsunoyama, H.; Tsukuda, T.; Häkkinen, H.; Aikens, C.M. Chirality and electronic structure of the thiolate-protected Au_{38} nanocluster. *J. Am. Chem. Soc*. **2010**, *132*, 8210–8218.

[42] Dolamic, I.; Knoppe, S.; Dass, A.; Burgi, T. First enantioseparation and circular dichroism spectra of Au_{38} clusters protected by achiral ligands. *Nature Comm*. **2012**, *3*, 798.

Bibliography

1. International Publications

1.1. As co-first author (highlighted as bold and undelined)

Chang, H.; **Kim, B. H.**; Jeong, H. Y.; Moon, J. H.; Park, M.; Shin, K.; Chae, S. I.; Lee, J.; Kang, T.; Choi, B. K.; Yang, J.; Bootharaju, M. S.; Song, H.; An, S. H.; Park, K. M.; Oh, J. Y.; Lee, H.; Kim, M. S.; Park, J.; Hyeon, T. Molecular-Level Understanding of Continuous Growth from Iron-Oxo Clusters to Iron Oxide Nanoparticles. *J. Am. Chem. Soc.* **2019**, *141*, 7037–7045.

Bootharaju, M. S.; **Chang, H.**; Deng, G.; Malola, S.; Baek, W.; Häkkinen, H.; Zheng, N.; Hyeon, T. $Cd_{12}Ag_{32}(SePh)_{36}$: Non-Noble Metal Doped Silver Nanoclusters. *J. Am. Chem. Soc.* **2019**, *141*, 8422–8425.

1.2. As contributing author (highlighted as bold and undelined)

Kim, B. H.; **Chang, H.**; Hackett, M. J.; Park, J.; Seo, P.; Hyeon, T. Size characterization of ultrasmall silver nanoparticles using MALDI-TOF mass spectrometry. *Bull. Korean Chem. Soc.* **2014**, *35*, 961–964.

Muckel, F.; Yang, J.; Lorenz, S.; Baek, W.; **Chang, H.**; Hyeon, T.; Bacher, G.; Fainblat, R. Digital doping in magic-sized CdSe clusters. *ACS Nano* **2016**, *10*, 7135–7141.

Yang, J.; Muckel, F.; Baek, W.; Fainblat, R.; **Chang, H.**; Bacher, G.; Hyeon, T. Chemical synthesis, doping, and transformation of magic-sized semiconductor alloy nanoclusters. *J. Am. Chem. Soc.* **2017**, *139*, 6761–6770.

Lu, Y.; Xu, Y.-J.; Zhang, G.-b.; Ling, D.; Wang, M.-q.; Zhou, Y.; Wu, Y.-D.; Wu, T.; Hackett, M. J.; Kim, B. H.; **Chang, H.**; Kim, J.; Hu, X.-T.; Dong, L.; Lee, N.; Li, F.; He, J.-C.; Zhang, L.; Wen, H.-Q.; Yang, B.; Choi, S. H.; Hyeon, T.; Zou, D.-H. Iron oxide nanoclusters for T 1 magnetic resonance imaging of non-human primates. *Nat. Biomed. Eng.* **2017**, *1*, 637–643.

Kale, V. S.; Hwang, M. S.; **Chang, H.**; Kang, J.; Chae, S. I.; Jeon, Y.; Yang, J.; Kim, J.; Ko, Y.-J.; Piao, Y.; Hyeon, T. Microporosity-Controlled Synthesis of Heteroatom Codoped Carbon Nanocages by Wrap-Bake-Sublime Approach for Flexible All-Solid-State-Supercapacitors. *Adv. Funct. Mater.* **2018**, 28, 1803786.

Yang, J.; Muckel, F.; Choi, B. K.; Lorenz, S.; Kim, I. Y.; Ackermann, J.; **Chang, H.**; Czerney, T.; Kale, V. S.; Hwang, S.-J.; Bacher, G.; Hyeon, T. Co^{2+}-Doping of Magic-Sized CdSe Clusters: Structural Insights via Ligand Field Transitions. *Nano Lett.* **2018**, *18*, 7350–7357.

Kwon, H. J.; Shin, K.; Soh, M.; **Chang, H.**; Kim, J.; Lee, J.; Ko, G.; Kim, B. H.; Kim, D.; Hyeon, T. Large-Scale Synthesis and Medical Applications of Uniform-Sized Metal Oxide Nanoparticles. *Adv. Mater.* **2018**, *30*, 1704290.

2. International Conferences

Chang, H.; Hyeon, T. Size characterization of Silver Nanoparticles Using MALDI-TOF Mass Spectroscopy. *The 12th International Nanotech Symposium & Exhibition (Nano Korea 2014)*, COEX, Seoul, Korea, July 2-4, 2014.

Chang, H.; Hyeon, T. Continuous growth of iron-oxo clusters to iron oxide nanoparticles: Insights on iron oxide nanoparticle formation at the early stage. *258th ACS National Meeting & Exposition*, San Diego Convention Center, San Diego, CA, USA, August 25-29, 2019. (Sci-Mix)

3. Awards

Chang, H. Continuous growth of iron-oxo clusters to iron oxide nanoparticles. Samsung Electro-Mechanics' 14th Best Paper Award, 2018, Bronze Award.

국문 초록 (Abstract in Korean)

특정한 조성과 구조를 가진 나노입자를 합성하는 것은 나노입자로 하여금 다양한 분야에서 응용이 가능하도록 기대할만한 물리화학적 성질을 가지도록 유도할 수 있다. 합성하고자 하는 나노물질이 점차 복잡해짐에 따라, 합성의 최적화를 보다 효율적으로 하고 결과물의 성능을 개선하기 위해서는 전체 합성 과정에 대한 명확한 이해가 필수적으로 선행 되어야한다. 기술이 발전함에 따라 나노입자 합성 기작에 대해 자세히 조사한 연구들이 이뤄졌고, 그 결과 나노입자 합성을 설명하기 위해선 비고전적 핵 형성 및 성장 모델이 필수적이라는 것이 밝혀졌다. 이런 연구들에서 분자와 나노입자 사이를 잇는 연결 고리로 볼 수 있는 나노클러스터들이 관찰되었다는 사실도 주목해야한다. 본 학위 논문은 나노입자와 나노클러스터의 합성 과정을 분석하고 분자 단위로 이해하는데 집중하고 있다.

먼저, 열 분해를 제한하여 산화철 나노입자의 합성을 섬세하게 조절했고, 다양한 분석 기술을 적용하여 합성 과정을 면밀히 분석했다. 그 결과 시작 단계의 전구체부터 나노입자에 이르기까지 합성 과정에 대해 분자수준의 이해를 성공적으로 할 수 있었다. 산

화철 나노입자 합성에 널리 쓰이는 전구체인 철-올레이트 복합체는 산소 원자 1개가 철 원자 3개와 동시에 결합한 중심부를 가진 클러스터 구조임을 확인했고, 이 복합체는 구분되는 핵 형성 과정을 나타내지 않으면서 연속적으로 성장해서 1 나노미터보다 작은 철-산소 클러스터, 더 나아가선 산화철 나노입자까지 커질 수 있다는 것을 알 수 있었다. 원자 단위의 성장은 크게 두 가지 효과로 인해 가능했다고 보인다. 리간드에 의한 철-산소 중심부의 안정화가 열 분해가 제한된 환경에서 극대화 됐으며, 저온 반응 조건에서 성장과정에서의 비수화 졸-겔 축합 반응이 제한적이었기 때문이다. 다양한 산화물 나노입자 합성들의 유사성을 고려했을 때, 이 연구에서 확인한 연속 성장 과정은 다른 산화물 나노입자의 형성 메커니즘을 이해하는데 통찰력 있는 정보들을 제공할 것으로 기대된다.

둘째, 금이 아닌 귀금속 나노클러스터에서는 어려웠던 비 귀금속이 도핑된 금속 나노클러스터를 추가 리간드를 넣어주는 방식으로 성공적으로 합성했다. 포스핀을 추가 리간드로 넣어줌으로써 카드뮴이 도핑 된 은 나노클러스터($Cd_{12}Ag_{32}(SePh)_{36}$)를 성공적으로 합성했고, 이 나노클러스터는 특징적인 흡광과 근적외선 영역의 발광을 나타냄을 확인했다. 이 클러스터의 구조는 4개의

$Cd_3Ag(SePh)_9$ 표면 모티프가 비대칭성 $Ag_4@Ag_{24}$ 금속 중심부를 둘러싼 구조임을 X-선 단 결정 분석을 통해 밝혔다. 한편, 초원자 이론과 시간에 따른 밀도 범함수 이론을 통해 나노클러스터의 전자 구조를 확인했다. $Cd_{12}Ag_{32}(SePh)_{36}$ 클러스터는 20개의 전자로 이뤄진 초원자로 볼 수 있으며, 이 물질의 이론적 키랄 광학 반응성은 키랄 광학 반응성이 존재한다고 잘 알려진 $Au_{38}(SR)_{24}$ 클러스터와 비견할 정도임을 알 수 있었다. 본 연구에서 제안한 리간드 보조 나노클러스터 합성은 다른 활성 금속을 귀금속 클러스터에 도핑하는 새로운 방식으로 쓰일 수 있을 것으로 기대된다.

주요어: 나노입자, 나노클러스터, 형성 기작, 분자 수준의 이해, 질량 분석법.

학번 2015-30218